Application of Lidar Altimetry and Hyperspectral Imaging to Ice Sheet and Snow Monitoring

by

Zachary Fair

A dissertation submitted in partial fulfillment
of the requirements for the degree of
Doctor of Philosophy
(Climate and Space Sciences and Engineering)
in The University of Michigan
2021

Doctoral Committee:

Associate Professor Mark Flanner, Chair
Associate Professor Jeremy Bassis
Associate Research Scientist Roger De Roo
Professor Valeriy Ivanov

Zachary Fair

zhfair@umich.edu

ORCID: 0000-0002-6047-1723

For my family and friends.

ACKNOWLEDGEMENTS

The work in Chapters 2 and 3 were funded by the NASA Earth and Space Science Fellowship (grant no. 19-EARTH19R-0047). The work in Chapters 3 and 4 were supported by NASA grant 80NSSC20K0062.

I would like to thank the collaborators that I have had the privilege of working with over these five years. In particular, I thank Kelly Brunt and Tom Neumann from NASA Goddard for the insightful conversations via email and Zoom. I came into my thesis research knowing little about lidar altimetry, so their patience and openness has been very helpful in the completion of my work. I extend my thanks to McKenzie Skiles for her knowledge of snowpack physics and snow grain size retrievals, which proved to be invaluable for Chapter 3 of this thesis. I also thank Benjamin Smith for his endless expertise in exploiting lidar altimetry data, and for our conversations regarding volumetric scattering bias in altimetry signals.

More generally, I thank the ICESat-2 and Operation IceBridge science teams for making two successful missions. I have met many science team members through the annual AGU conference, and the conversations have all been illuminating and enjoyable. I also thank the members of the SnowEx mission, particularly those whom I met at the 2019 Snow Field School in Bretton Woods, NH. Although I am a recent convert to snow science, the people I met there were very friendly and accepting of new science ideas. I hope to continue working with each of these science teams as I advance in my career.

I extend large thanks to my advisor for the past three years, Dr. Mark Flanner.

I came into his group with little experience in snow science or radiative transfer modeling. However, Mark's unending patience proved to be highly encouraging as we formulated project ideas for this thesis. Even though I continued to focus on observations rather than modeling, Mark's guidance and expertise proved valuable as I learned about snowpack physics. If we were to ever collaborate again in a future study, then I would look forward to the opportunity.

I would not have been able to make it through graduate school without the friends I made along the way. I must give a shoutout to the friends I made as an intern at NASA Langley Research Center, particularly Abbey, Rachel, Pablo, Tia, and Megan. We may not speak to each other as often, but the crazy times we had together made for a great internship. Among my fellow CLaSP students, I thank Jamie, Anthony, Zach Butterfield ("other Zach"), Matt, and many others for the fun times and trips to northern Michigan. I must give my biggest thanks to the members of the "Physics House" friend group, including Emily, Joe, Glenn, and Peter, among others. The weekly movie nights and countless other activities have been some of the most memorable experiences of my time here.

Finally, I have to thank my family for the unending love and support over the past 28 years. Although I have moved to an entirely new state to continue my education, it never feels like any of you are far away.

"This is a new day, a new beginning." - Ahsoka Tano, *Star Wars Rebels*

TABLE OF CONTENTS

LIST OF FIGURES

Figure

LIST OF TABLES

Table

ABSTRACT

The Greenland Ice Sheet (GrIS) is of tremendous importance for climate change projections. The GrIS has contributed an estimated 10.8 mm to sea level rise since 1992, and that contribution is expected to increase in the coming decades. It is therefore essential to make routine measurements of ice, meltwater, and snow over the GrIS using satellite and airborne observations. Two prominent methods for ice sheet monitoring include lidar altimetry and hyperspectral imaging. Lidar altimetry is typically used to make fine-scale estimates of ice sheet surface height, whereas hyperspectral imaging is commonly utilized to infer snow or ice surface composition. In this dissertation, I use data from the Ice, Clouds, and land Elevation Satellite-2 (ICESat-2) and the Next Generation Airborne Visible/Infrared Imaging Spectrometer (AVIRIS-NG) to examine light transmittance over the Greenland Ice Sheet. I first utilize ICESat-2 photon-counting data for the development of a retrieval algorithm for supraglacial lake depth, with validation from the Operation IceBridge airborne mission. This work was performed to support other depth retrieval efforts that struggle with attenuation in deep water. I then use hyperspectral radiative transfer models to perform a sensitivity analysis on snow grain size retrievals. Snow grain size is an important metric for snowpack evolution, but there are limited efforts to quantify potential errors in an existing inversion algorithm. Lastly, I used a combination of Operation IceBridge altimetry and AVIRIS-NG hyperspectral data to assess the impacts of snow grain size on surface heights derived from lidar altimetry.

Results from the three studies indicate that lidar signals and ice reflectance in the near-infrared are highly sensitive to changes in surface media. Because it operates at

532 nm, the ICESat-2 laser penetrates through liquid water with minimal signal loss, but volumetric scattering within a snowpack may induce significant errors in surface heights derived from Operation IceBridge, especially at large snow grain sizes. The ICESat-2 laser is susceptible to noise from clouds and rough surface topography, so additional work is needed to accurately identify supraglacial lake beds and volumetric scattering caused by snow. Also, the near-infrared spectrum of snow is highly sensitive to changes in solar geometry and to the presence of dust, therefore increasing uncertainties in snow grain size retrievals. Co-dependencies between snowpack perturbations were not considered, but I speculate that snow particle shape and snow impurities will impact the angular distribution of radiation reflected from a snowpack. I expect that the research presented here will motivate the development of improved algorithms for supraglacial lake depth, snow grain size, and lidar altimetry bias.

CHAPTER I

Introduction

1.1 Fundamentals of Remote Sensing

1.1.1 Reflectance

In earth science, there is frequently a need for measurements with routine coverage of the Earth's surface over time. Field observations are insufficient for this purpose, so airborne and satellite remote sensing is utilized to improve spatiotemporal coverage. Remote sensing is performed by measuring electromagnetic radiation that is reflected or emitted by the Earth's surface or atmosphere. Depending on (a) the wavelength of the radiation measured and (b) the radiative quantity measured, we can infer aspects of the climate system and monitor changes over time.

In this thesis, we consider reflected radiance (or simply "reflectance"), which is the amount of sunlight that is reflected by the Earth to space. Reflectance (R) is mathematically represented through:

$$R = \frac{F^{\uparrow}}{F^{\downarrow}} \tag{1.1}$$

where $F^{\uparrow}$ and $F^{\downarrow}$ represent the radiative flux that moves away from and toward the surface, respectively. A radiative flux considers radiation that is integrated across all angles across a hemisphere, so it is also referred to as a "hemispheric" quantity. In

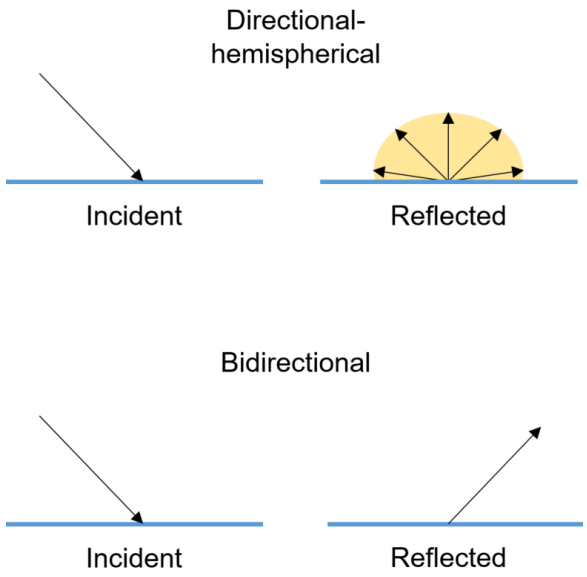

Figure 1.1: A schematic showing the reflectance quantities relevant to Chapters 3 and 4. The arrows represent sunlight moving toward or away from the surface.

most realistic scenarios, incident and reflected radiance vary in direction and intensity, depending on solar geometry and the state of the atmosphere and surface. Therefore, we may consider a "directional" reflectance that is represented by an azimuth angle and a zenith angle. However, it is difficult to measure purely directional radiance with current remote sensing techniques, so the term "conical" reflectance is often used to denote observed directional reflectance. Radiative transfer models are required to estimate directional reflectance from conical or hemispherical quantities (*Schaepman-Strub et al.*, 2006; *Nicodemus et al.*, 1977).

A reflectance is defined on whether we consider directional or hemispheric radiation for incident and reflected light. If purely directional or hemispheric radiation is considered, then the corresponding reflectance is known as bidirectional and bihemispherical, respectively. We may also use different quantities for the incident and reflected light. For instance, a reflectance with directional sunlight and hemispherical reflected light is known as directional-hemispherical reflectance (*Schaepman-Strub et al.*, 2006). In Chapters 3 and 4, we derive bidirectional and directional-hemispherical reflectances from radiative transfer and Monte Carlo models to infer

the state of a snowpack. A graphical representation of these two quantities is given in Figure 1.1.

The characterstics of an observed surface have a strong impact on the distribution of reflected radiation across a hemisphere. A common assumption in radiative transfer modeling and remote sensing is that a surface reflects radiation equally in all directions, independent of topography or solar geometry (*Liou*, 2002; *Petty*, 2006). A surface with this property is also known as a Lambertian or isotropic surface. In the top example in Figure 1.1, the hemispheric reflectance is a simplified example of Lambertian reflectance. Because reflected radiation is equally distributed among all azimuth and zenith angles, directional intensity ($I^{\uparrow}$) and hemispheric irradiance ($F^{\uparrow}$) for a Lambertian surface are related through the equation

$$F^{\uparrow} = \pi I^{\uparrow} \tag{1.2}$$

and the directional irradiance observed at viewing angle θ_v obeys Lambert's cosine law:

$$I(\theta_v) = I(0)cos(\theta_v) \tag{1.3}$$

The Lambertian assumption is most accurate for surfaces that are highly reflective or compose of isotropically-scattering particles near midday, where the incident sunlight is directly overhead (i.e., solar zenith angle is 0°). Freshly fallen snow is an example surface that is commonly assumed to be a Lambertian surface in radiative transfer applications, given its high reflectivity and low surface roughness. However, snow darkens and coarsens as it ages, so it becomes less of a Lambertian reflector, so reflected radiation will preferentially scatter in a single direction. Non-Lambertian, or anisotropic, surfaces preferentially scatter radiation in a single direction, and it becomes prominent for rough surfaces and large solar zenith angles. If left unchecked,

anisotropic reflectance may have significant consequences on reflectance quantities measured by remote sensing platforms, particularly if Lambertian reflectance is assumed. (*Dumont et al.*, 2010; *Liou*, 2002; *Petty*, 2006).

1.1.2 Spectral Dependence of Reflectance

When the reflectivity of a surface is considered, a common metric to use in earth science is the surface's broadband albedo. Broadband albedo is defined as the hemispheric reflectivity of a surface across a range of wavelengths over the electromagnetic spectrum (*Petty*, 2006). Spaceborne sensors such as the Clouds and the Earth's Radiant Energy System (CERES) may be used to measure broadband albedo for shortwave and longwave radiation directly (*Rutan et al.*, 2009). Broadband albedo may also be estimated by performing a weighted integration of multispectral or hyperspectral reflectance, as is obtained from sensors such as the Moderate Resolution Imaging Spectrometer (*Liang*, 2000).

Broadband albedo is most useful for modeling efforts that require simplified radiative transfer calculations, such as climate projections and boundary layer meteorology (*Dickinson*, 1983; *Stull*, 1988; *Hartmann*, 2016). However, it is less effective for monitoring changes in surfaces that experience significant changes in reflectivity over time. Figure 1.2 shows an example with snow of different optical grain sizes, where increasing grain size indicates aging of the snowpack. The left plot shows that the broadband albedo of snow decreases asymptotically from 0.872 to 0.755 as the snow ages, whereas the right figure demonstrates the spectral dependence of changes in albedo. There is only a notable decrease in reflectivity at red wavelengths in the visible spectrum, with green and blue wavelengths showing little change with grain size. The near-infrared spectrum of the snow is more sensitive to aging and grain size increases, and prominent absorption features may be observed at 1.03 μm and 1.3 μm. This information is lost if only a broadband albedo is considered.

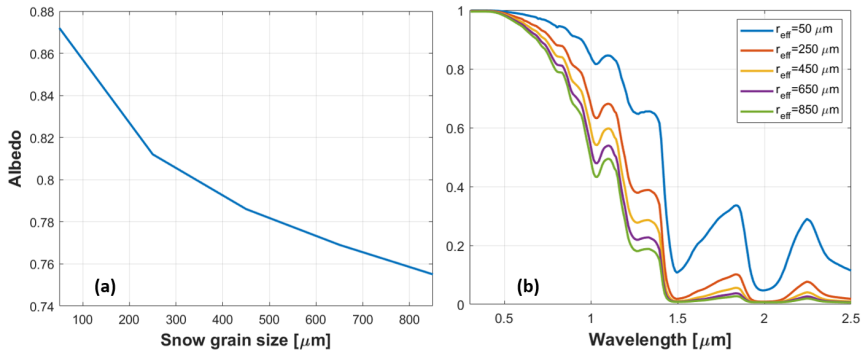

Figure 1.2: (Left) Broadband albedo estimates for a snowpack of 5 optical grain sizes: 50 μm, 250 μm, 450 μm, 650 μm, and 850 μm. (Right) Spectral albedo for the wavelength range 0.3-2.5 μm given the same conditions.

Hyperspectral instruments and models offer the opportunity to exploit spectral information of a surface by recording reflected radiation at hundreds of wavelengths. For example, the reflectances in Figure 1.2 were derived using the Snow, Ice and Aerosol Radiative (SNICAR) model, a hyperspectral radiative transfer model that uses 480 wavelengths to simulate snowpack reflectance in response to changes in incident sunlight and the addition of light-absorbing particles (*Flanner et al.*, 2007). Another example is the Airborne Visible/Infrared Imaging Spectrometer (AVIRIS), a hyperspectral sensor that obtains reflectance measurements of the Earth's surface over 224 bands (*Green et al.*, 1998). Information obtained from hyperspectral methods is useful for surface classification and composition analysis in remotely sensed data. We utilize hyperspectral data to estimate snow grain size using SNICAR and AVIRIS in Chapters 3 and 4.

1.1.3 Active Remote Sensing

The reflectance quantities described in Section 1.1.2 are observed with passive remote sensing, where a sensor detects radiation that originated from the Sun or the Earth. The instrument does not produce its own signal to illuminate the Earth, so passive measurements of reflectance in the visible spectrum are difficult to perform

at night. To observe the Earth's surface in the visible spectrum without solar illumination, a sensor that actively generates its own signal is required. An active sensor transmits a signal toward the surface, and a small portion of backscattered energy returns to the receiver of the sensor. The backscatter is then used to determine information about the surface (*Ulaby et al.*, 1986).

Airborne and spaceborne active sensors utilize signals at specific wavelengths to limit attenuation by the atmosphere. The two most common types of active sensor are radar and lidar, which generate signals in the microwave and the visible or near-infrared, respectively. Radar is most frequently used for operational weather forecasting, for precipitation and large cloud layers are the only aspects of the atmosphere that significantly impact microwave signals (*Ulaby et al.*, 1986). A specialised form for radar known as synthetic aperture radar (SAR) may be used to generate topographic maps and to penetrate ice sheets (*Zhou et al.*, 2009). Lidars transmit their signals at high repetition frequencies, so they are also useful for topographic information. Lidar also has a small footprint relative to radar and passive sensors (centimeters to meters, compared to meters to kilometers), so it has been applied for cloud and aerosol monitoring and forest management (*Liu et al.*, 2004; *Neuenschwander et al.*, 2009). Its high spatial resolution has also made it an effective tool to obtain snow depth and shallow-water bathymetry (*Deems et al.*, 2013; *Brock et al.*, 2002).

The received signal of a lidar includes two critical attributes: the time at which the backscatter was received, and the strength of the received signal (*Liang*, 2018). The received time (t_{rx}) is compared to the transmittance time (t_{tx}) to estimate the distance between the sensor and the surface. Assuming that the signal travels at the speed of light (c), the sensor-surface distance (or range, r) is given by:

$$r = \frac{1}{2}c(t_{rx} - t_{tx}) \tag{1.4}$$

where the one-half term accounts for the signal traveling between the sensor and

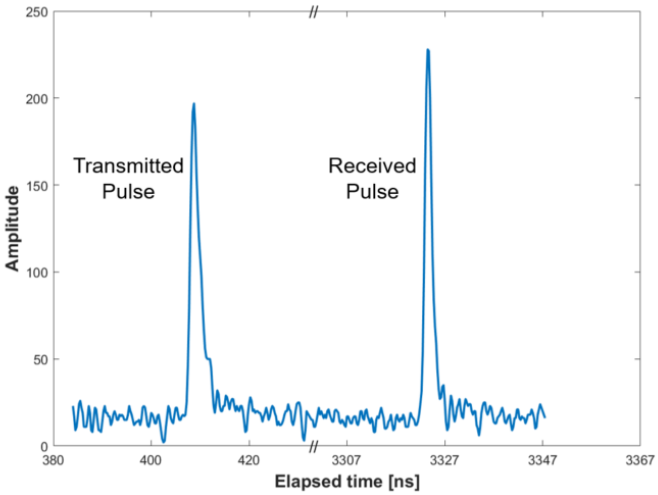

Figure 1.3: An example lidar pulse over ice from the Airborne Topographic Mapper represented using waveforms. The left waveform is the laser pulse transmitted by ATM, whereas the right waveform is the energy received by the detector.

the surface twice. When applied to a modeled ellipsoid of Earth, lidar ranges are converted to fine-scale estimates of elevation above the surface. The signal strength may then be used to infer information about the backscatter target(s), such as the surface composition or the type of atmospheric aerosol.

Lidar beams may have one of two configurations: continuous wave lidar and pulsed lidar. A continuous wave lidar emits a laser pulse continuously, and the signal is processed as a sinusoidal wave. The sensor-surface range is calculated by measuring the phase difference between the transmitted and received pulses. A pulsed lidar transmits its signal in discrete photon pulses at a designed repetition frequency. Each lidar pulse provides a sample of the Earth's surface, with overlap possible between laser pulses depending on the beam footprint size and pulse repetition frequency (*Wehr and Lohr*, 1999). Continuous wave lidars are infrequently used in earth science, so we focus on pulsed lidar systems in this thesis.

Raw lidar data are typically processed using waveforms, which represent the change in amplitude of a signal over time. An example waveform profile is given

in Figure 1.3 for the Airborne Topographic Mapper (ATM), an airborne lidar used for ice and coastal surveys (*Brock et al.*, 2002). The amplitude, or relative strength, of the waveforms are used to determine time of transmitted energy and received energy by taking the median or centroid of each waveform (*Dong and Chen*, 2017). To reduce noise, a threshold may be applied to the digitized waveform. The centroid or median times of the transmitted and received waveforms then serve as input to Equation 1.4 to estimate range. For example, the transmitted and received pulses in Figure 1.3 have centroid times of 408.75 ns and 3311.75 ns, respectively. Using Equation 1.4, we calculate a range of 435.45 m for the given lidar shot.

The shape of the received waveform is highly sensitive to surface features and terrain. If the surface is highly reflective on a cloud-free day, then the received signal may be stronger than the transmitted pulse (Figure 1.3). Conversely, a surface with rough terrain may broaden the width of the received pulse and produce a slight delay in the received time estimate (*Dong and Chen*, 2017). More complex surfaces, such as a tree or pressure ridges on sea ice, will produce multiple pulse echoes that correspond with each layer of the surface feature. Therefore, waveform lidar is useful for quantifying biomass in forests, for it allows discrimination between the tree canopy and the surface (*Neuenschwander et al.*, 2009).

An emerging technology for lidar is a photon-counting system. Instead of using waveforms, photon clusters are time-tagged relative to the last transmitted signal. The time tag is then used to calculate sensor-target range through Equation 1.4. Received photons are classified as signal or background noise, based on the calculated range relative to a digital elevation model. Although the photon-counting approach produces greater noise from the solar background, it also has improved resolution of surface features and terrain (*Popescu et al.*, 2018; *Spinhirne*, 1993). A modern example of a photon-counting lidar is the Ice, Clouds, and land Elevation Satellite-2 (ICESat-2), which takes elevation measurements of the surface at a wavelength of 532

nm. It has a spatial resolution of ∼0.7 m and centimeter-level accuracy (*Neumann et al.*, 2019b), allowing for fine-scale estimates of land ice height, sea ice freeboards, and vegetation canopy height (*Smith et al.*, 2019; *Kwok et al.*, 2020; *Neuenschwander and Pitts*, 2019). The photon-counting system in ICESat-2 is also useful for bathymetric applications (Chapter 2), though it also introduces subsurface noise that often requires additional detection and attribution (Chapter 4).

1.2 Relevant Components of the Cryosphere

The cryosphere contains all aspects of the Earth's surface that concern frozen water, including sea ice, glaciers and ice sheets, and snow. In this section, we discuss the components of the cryosphere relevant to this thesis, i.e. ice sheets and snow, and highlight why they are important to monitor using remotely sensed data.

1.2.1 Ice Sheets

The Greenland Ice Sheet (GrIS) is the second largest ice sheet in the world, with 1.71 million km^2 of ice. The thickness of the ice ranges between 2-3 km for most of the ice sheet (*Morlighem et al.*, 2017), and a complete melting of the GrIS would result in 7.2 m (24 ft) of sea level rise (*Vaughan et al.*, 2013). The GrIS extends between 60°- 85°N, and at these latitudes the ice sheet receives a limited quantity of sunlight throughout the year. Surface temperatures over the ice sheet are therefore below freezing in non-summer months (*Shuman et al.*, 2001). Temperatures approach or exceed the melting point of ice in Northern Hemisphere summer, so the GrIS experiences melting and ice loss during this period (also known as the "melting season").

The GrIS has lost 150 ± 13 Gt yr^{-1} since 1992, contributing a total of 10.8 ± 0.9 mm yr^{-1} to sea level rise (*The IMBIE Team*, 2020). Ice loss has been observed among all regions of the ice sheet, with the greatest loss taking place along the western margin. Dynamical processes such as calving were the primary contributor

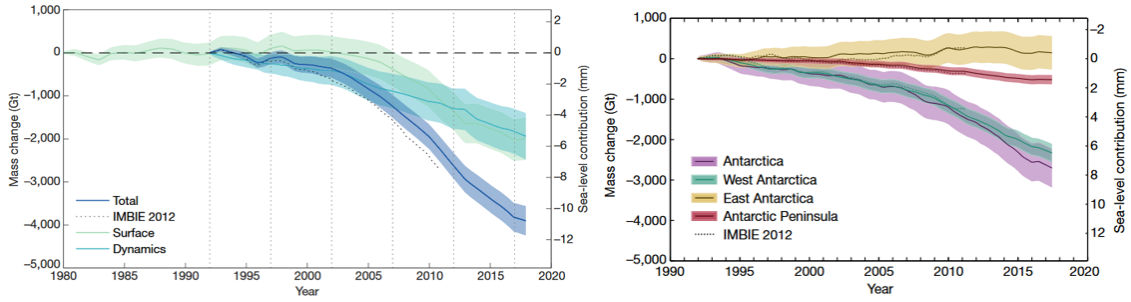

Figure 1.4: Ice mass loss and sea level rise estimates based on observations over Greenland (left) and Antarctica (right). Ice loss estimates are divided into individual processes (Greenland) or regions (Antarctica). Courtesy of *The IMBIE Team* (2020) and *The IMBIE Team* (2018).

to GrIS mass loss at the start of the satellite record, but meltwater runoff has become an increasingly important factor in the past decade (Figure 1.4, left). Ice melt is particularly important in the ice sheet interior, where accumulation exceeds ablation (loss) in the non-summer months, but melting may take place in summer if the air temperature warms sufficiently. In recent years, changes in climate and atmospheric circulation has resulted in ice melt propagating further inland near the Greenland summit (*Bevis et al.*, 2019).

The Antarctic Ice Sheet (AIS) is the world's largest ice sheet and the largest freshwater reservoir, spanning 14 million km^2 around the South Pole. Because of its large size, the AIS is commonly separated into three regions: the East Antarctic Ice Sheet (EAIS), the West Antarctic Ice Sheet (WAIS), and the Antarctic Peninsula Ice Sheet (APIS). The EAIS is the coldest and least documented region. It is also the largest portion of Antarctica, with enough ice to raise sea levels by 53 m (*Fretwell et al.*, 2013). The WAIS is a marine ice sheet, meaning that the bed of the ice sheet is situated below sea level. Although smaller than the EAIS, a complete loss of the WAIS would be sufficient to contribute 3.3 m to sea level rise (*Bamber et al.*, 2009). The APIS is the smallest Antarctic ice mass, with a sea level rise potential of 0.24 m (*Pritchard and Vaughan*, 2007). It is also the warmest region in Antarctica, so it is

more likely to experience ice loss than the other regions.

Although the AIS is larger than the GrIS, its contribution to recent sea level rise is smaller. The AIS has contributed 7.6 ± 3.9 mm to sea level rise since 1992, though there is substantial interannual and regional variability. The WAIS was the only significant contributor until the last decade, and approximately 85% of current Antarctic ice loss is from the WAIS. Recent warming trends over the APIS have resulted in enhanced ice loss over the peninsula, and it currently contributes ∼15% to Antarctic ice loss (Figure 1.4, right). Over the EAIS, satellite observations indicate a slight increase in ice in the past decade on average. However, the limited observation record shows significant interannual variability, so there is substantial uncertainty in accumulation rates and ice loss estimates over the EAIS (*The IMBIE Team*, 2018).

A critical component of ice sheet mass balance is meltwater, or the melting of ice into liquid water. In large quantities, meltwater accumulates into topographic depressions and forms supraglacial lakes and streams (*Echelmeyer et al.*, 1991). Meltwater in these basins may penetrate through the underlying ice and induce hydrofracture, a mechanism that cracks surrounding ice and leads to accelerated mass loss (*Das et al.*, 2008). Upon reaching the ice bed, meltwater can lubricate the ice-rock interface and facilitate ice movement and eventual discharge (*Zwally et al.*, 2002).

The development of meltwater is governed by the surface energy balance of an ice sheet or glacier:

$$R_{net} = S^{\downarrow} + S^{\uparrow} + L^{\downarrow} + L^{\uparrow} + H + E \tag{1.5}$$

In Equation 1.5, the radiative terms are S and L, where S is shortwave radiation (sunlight) and L is Earth's emitted longwave radiation. The terms H and E are the turbulent terms that represent sensible heat flux and latent heat flux, respectively. Sensible heat flux refers to the transfer of thermal energy between the surface and atmosphere through convection, whereas latent heat flux is surface-atmosphere energy

exchanges through phase changes of water. The arrows indicate the direction of propagation for the radiative quantity: downward or "downwelling" radiation is emitted towards the Earth's surface, whereas upward or "upwelling" radiation is emitted to space. The upwelling terms in Equation 1.5 are negative quantities, for they cause the surface to lose energy. The turbulent terms can be positive or negative depending on the local state of the troposphere, but generally both terms are negative when there is energy transferred from the surface to the atmosphere. If R_{net} is positive, the surface has a net gain of energy and warms. Conversely, a negative R_{net} implies a loss of energy and cooling at the surface.

The individual terms of the energy balance equation have an influence on the development and refreezing of meltwater on ice sheets. In late-spring and summer, an ice sheet or glacier will experience a greater amount of incident solar radiation ($S^{\downarrow}$). A portion of it will be reflected back to space ($S^{\uparrow}$) due to the high reflectivity of ice, and the Earth's longwave radiation ($L^{\uparrow}$) will partially compensate for the increase in sunlight. However, the upwelling radiation may be insufficient to offset incident radiation, so regions of the ice will experience a positive R_{net} that initiates melting of the ice. Melting continues until fall, where the decrease in daylight hours will render R_{net} negative and refreeze standing meltwater. Clouds in early fall may absorb upwelling longwave radiation and emit it back to the surface ($L^{\downarrow}$), thereby delaying meltwater refreezing by a few days (*Bennartz et al.*, 2013; *Van Tricht et al.*, 2016). Otherwise, downwelling longwave radiation plays a small role in the ice sheet energy balance. The influence of the turbulent heat fluxes is also small at the regional scale, though meltwater may serve as a latent heat reservoir at micro-scales (*Humphrey et al.*, 2012). Warm air temperatures in the melting season may also generate a significant transfer of sensible heat to a snow or ice surface, thereby enhancing melt rates.

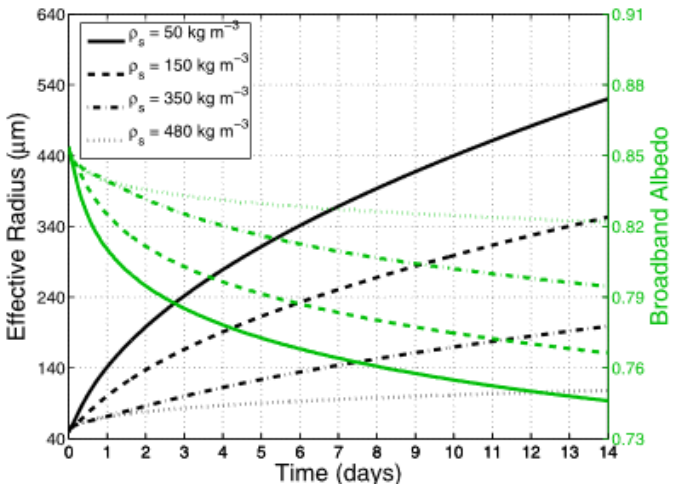

Figure 1.5: The simulated evolution of snow albedo (green) and snow grain size (black) over a period of two weeks, given four snow densities. Courtesy of *Flanner and Zender* (2006).

1.2.2 Snow

Seasonal snow is a critical aspect of climate, ecology, and hydrology. It reflects a significant fraction of incident sunlight back to space, thereby slowing warming rates of the surface. Snow also functions as an effective insulator for underlying vegetation and soil in otherwise harsh winter conditions (*Zhang*, 2005). In the warm season, runoff from melting snow accumulates in rivers and basins that account for a significant portion or the world's freshwater supply (*Bales et al.*, 2006). Many animal and plant species also depend on the snow cover for insulation or camouflage, so the timing of snowfall and snowmelt has a major impact on regional ecosystems (*Penczykowski et al.*, 2017). The duration and extent of seasonal snow is particularly sensitive to a warming climate (*Barnett et al.*, 2005), and there are concerns that current warming trends will have a profound impact on snow-dependent systems. It is for these reasons that the 2017 Decadal Survey lists snow accumulation and melt as factors of critical importance for future science missions (National Academies, 2018).

The state of a snowpack is best described by its age, or the length of time between precipitation and snow melt. When snow is freshly fallen, it starts in the "dry"

regime with low snowpack density and small snow grains. The snow will transition into a "wet" regime if the snow surface temperature exceeds the melting point for a significant duration of time. In the wet regime, the snow density and grain size gradually increase as the snow melts, with both processes decreasing broadband albedo, as seen in Figure 1.5. The snowpack warms more efficiently as the albedo decreases, generating a component of the snow albedo feedback (*Aoki et al.*, 1999; *Flanner and Zender*, 2006). The snow albedo feedback may be further enhanced by the presence of light-absorbing particles or the angle of incident sunlight.

In snow modeling studies, a snowpack is commonly represented as a porous medium composed of an ice structure with air pores (Figure 1.6). The snow is not a continuous medium, but rather is an aggregate of many ice particles. The snow particles are not represented as individual snowflakes in models, as precise estimates and processing of snow grain radius is difficult. Instead, snow modeling studies use a quantity known as the optically-equivalent snow grain size, also referred to as the effective snow grain size (r_{eff}). The effective grain size represents individual snow particles as spheres that have the same optical properties as nonspherical particles of equivalent size (*Warren*, 1982; *Grenfell et al.*, 1994; *Aoki et al.*, 1999). Studies have shown that the spherical particle assumption is valid for bulk snow albedo calculations (*Grenfell and Warren*, 1999; *Grenfell et al.*, 2005), though it is less effective at accurately reproducing snowpack microphysical processes and directional reflectance (*Kokhanovsky and Zege*, 2004).

A snowpack is not always a clean medium, and frequently contains light absorbing impurities (LAPs) such as dust or black carbon (soot). LAPs may be transported hundreds to thousands of kilometers and deposit onto a snow surface. Once deposited, snow impurities can dramatically alter snowpack albedo even in small quantities, though the influence is spectrally-dependent. Albedo in the visible spectrum is especially sensitive to the presence of LAPs (*Wiscombe and Warren*, 1980), and

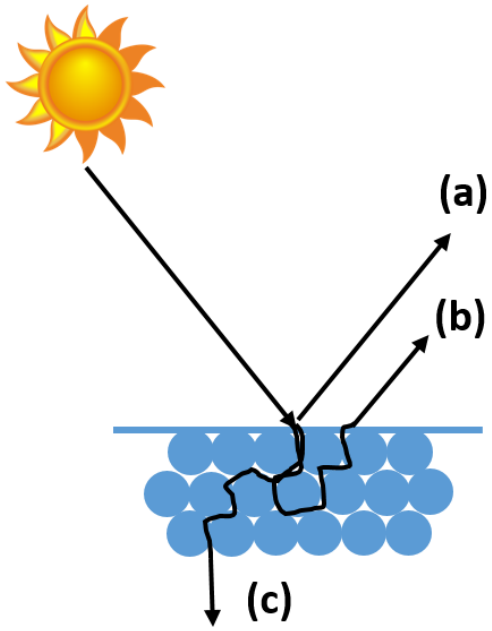

Figure 1.6: A simple schematic of sunlight propagation through a snowpack of spherical snow grains. The light may be reflected from the snow surface (a), scatter through the snowpack before reflection (b), or transmit through the snow after scattering (c).

it decreases significantly as LAP content increases. In sufficient quantities, LAPs in the surface snow layer may lead to an enhanced snow albedo feedback in the melting season (*Flanner and Zender*, 2006). In contrast, large quantities of impurity are required to impact near-infrared albedo, which can actually increase in the presence of dust.

The angle of incident sunlight, also known as solar zenith angle or illumination angle, plays an important role in determining the reflectivity of a snowpack. The reflectance of a snowpack is lowest when the Sun is near-zenith and highest when the Sun is close to the horizon, due to forward scattering by ice particles and shallower penetration of sunlight (*Warren and Wiscombe*, 1980). The solar zenith angle also has a major influence on the direction at which radiation is reflected from a snowpack. At low illumination angles (i.e., near-zenith), reflected radiance is distributed isotropically, or equally in all directions. Reflectance is preferentially scattered in the forward

direction at larger illumination angles, therefore increasing observed reflectance near the horizon and decreasing it at other viewing angles (*Dumont et al.*, 2010). We examine the impacts of solar geometry and anisotropic reflectance in greater detail in Chapter 3.

1.3 Outline of Thesis

The vital role of ice and snow in the climate system necessitates the development and calibration of retrieval methods using remote sensing. In this dissertation, we use a fusion of hyperspectral radiance data and lidar altimetry to answer questions about ice and snow. Chapter 2 uses lidar altimetry to estimate meltwater depth over both the Greenland and Antarctic Ice Sheets. We examine the feasibility of satellite and airborne altimeters for this purpose. We also discuss what is needed in creating an automated algorithm for supraglacial lake depth retrievals. Chapter 3 examines how solar geometry and changes to the snowpack may affect retrievals of snow grain size. We simulated snowpack perturbations using the radiative transfer model SNICAR and a Monte Carlo photon tracking model. The snowpack variables we considered included aspherical ice particles and the addition of LAPs. Chapter 4 utilizes both lidar altimetry and snow grain size retrievals to analyze the effects of snow on lidar signals. We quantify bias in an airborne lidar altimeter with the expectation that the results will be applicable to spaceborne altimetry measurements. Snow grain size retrievals from an airborne hyperspectral imager are used to attribute altimetry errors to volumetric scattering in snow.

CHAPTER II

Supraglacial Lake Depth Retrievals

As Published In: Fair, Z., M. Flanner, K. M. Brunt, H. A. Fricker, and A. Gardner (2020), Using ICESat-2 and Operation IceBridge altimetry for supraglacial lake depth retrievals, *The Cryosphere*, 14, 4253–4263, doi:10.5194/tc-14-4253-2020.

Abstract. Supraglacial lakes and melt ponds occur in the ablation zones of Antarctica and Greenland during the summer months. Detection of lake extent, depth, and temporal evolution is important for understanding glacier dynamics. Previous remote sensing observations of lake depth are limited to estimates from passive satellite imagery, which has inherent uncertainties, and there is little ground truth available. In this study, we use laser altimetry data from the Ice, Cloud, and land Elevation Satellite-2 (ICESat-2) over the Antarctic and Greenland ablation zones and the Airborne Topographic Mapper (ATM) for Hiawatha Glacier (Greenland) to demonstrate retrievals of supraglacial lake depth. Using an algorithm to separate lake surfaces and beds, we present case studies for 12 supraglacial lakes with the ATM lidar and 12 lakes with ICESat-2. Both lidars reliably detect bottom returns for lake beds as deep as 7 m. Lake bed uncertainties for these retrievals are 0.05-0.20 m for ATM and 0.12-0.80 m for ICESat-2, with the highest uncertainties observed for lakes deeper than 4 m. The bimodal nature of lake returns means that high-confidence photons are often insufficient to fully profile lakes, so lower confidence and buffer photons

are required to view the lake bed. Despite challenges in automation, the altimeter results are promising, and we expect them to serve as a benchmark for future studies of surface meltwater depths.

2.1 Introduction

The ice sheets of Antarctica and Greenland modulate rates of sea level rise, contributing 14.0 ± 2.0 mm (Antarctica) and 13.7 ± 1.1 mm (Greenland) since 1979 (*Mouginot et al.*, 2019; *Rignot et al.*, 2019). Current trends indicate greater melt in the coming decades, leading to the contributions from both ice sheets to overtake the contribution of thermal expansion to sea level rise (*Vaughan et al.*, 2013). Meltwater plays vital roles in ice sheet evolution (e.g., *van den Broeke et al.*, 2016), including aggregation on ice sheets as supraglacial lakes, many of which are several meters deep (*Echelmeyer et al.*, 1991). When unfrozen, these lakes exhibit a lower albedo than that of the surrounding ice, allowing them to absorb more incoming solar radiation and melt ice more efficiently, thus generating a positive feedback (*Curry et al.*, 1996). Supraglacial lakes are significant reservoirs of latent heat (*Humphrey et al.*, 2012), and their spectral emissivity in the IR spectrum also differs from bare ice (*Chen et al.*, 2014; *Huang et al.*, 2018), which can lead to potentially significant impacts on the surface energy balance of ice sheets.

A substantial portion of meltwater eventually drains into supraglacial streams or moulins (drainage channels), where it can flow to the ice bed (*Banwell et al.*, 2012; *Catania et al.*, 2008; *Selmes et al.*, 2011). During catastrophic lake drainage events, meltwater penetration into the ice can also lead to hydrofracture, a mechanism through which meltwater facilitates full ice fracture as a result of the stresses induced by the density contrast between liquid water and ice (*Das et al.*, 2008). Meltwater injection to the bed can also modify basal water pressures which in turn modify the resistance to ice flow and thus can impact sliding velocity and ice discharge.

(*Parizek and Alley*, 2004; *Zwally et al.*, 2002). Hydrofracture can lead to significant ice loss for outlet glaciers and ice shelves (*Banwell et al.*, 2013). Current observations and modeling efforts indicate a propagation of supraglacial lakes farther inland as the climate warms (*Howat et al.*, 2013; *Leeson et al.*, 2015; *Lüthje et al.*, 2006), raising further concerns for accelerated mass loss. For these reasons, knowledge of supraglacial lakes is important for our understanding of ice sheet evolution.

Previous studies developed techniques for detecting supraglacial lakes and retrieving depth, areal coverage, and volume. In-situ observations employed sonar and radiometers to approximate lake depth and albedo (*Box and Ski*, 2007; *Tedesco and Steiner*, 2011). However, the harsh conditions of Antarctica and Greenland, the transience of meltwater, and the sheer size of the ice sheet ablation zones restrict the potential for extensive in-situ measurements, encouraging lake depth and areal coverage estimates from passive remote sensing data such as Landsat-8, MODIS, and Sentinel-2 A/B. Supraglacial water is darker than surrounding ice in visible and IR bands, allowing the use of band ratios between blue and red reflectance (*Stumpf et al.*, 2003). The normalized water difference index (NWDI) and dynamic thresholding techniques have also been considered for lake detection (*Fitzpatrick et al.*, 2014; *Liang et al.*, 2012; *Moussavi et al.*, 2016; *Pope*, 2016; *Williamson et al.*, 2017; *Moussavi et al.*, 2020). Other methods implemented radiative transfer models (*Georgiou et al.*, 2009) or positive degree day models (*McMillan et al.*, 2007) to estimate lake albedo and meltwater volume, respectively. By comparing surface reflectance data of supraglacial water to that of ice and optically deep water, empirical relationships have been derived to approximate lake depth (*Philpot*, 1989; *Sneed and Hamilton*, 2007).

Image-based empirical techniques rely on approximations of lake bed albedo and an attenuation parameter, both of which are subject to uncertainties from lake heterogeneity and cloud cover (*Morassutti and Ledrew*, 1996). Furthermore, *Pope et al.*

(2016) found that band ratios were insensitive to lakes deeper than 5 m, leading to errors that may exceed 1 m. Parameter fitting in the empirical equations requires supplementary depth retrievals, often from in-situ sources. More accurate methods for supraglacial lake detection are needed to improve image-based estimates.

In September 2018, the Ice, Cloud and land Elevation Satellite-2 (ICESat-2) with the primary objective of obtaining laser altimetry measurements of the polar regions (*Abdalati et al.*, 2010; *Markus et al.*, 2017; *Neumann et al.*, 2019b). Observations using the Airborne Topographic Mapper (ATM) and Multiple Altimeter Beam Experimental Lidar (MABEL) indicated the potential for shallow water profiling with laser altimetry (*Brock et al.*, 2002; *Brunt et al.*, 2016; *Jasinski et al.*, 2016), and ICESat-2 applications were recently demonstrated by *Ma et al.* (2019) and *Parrish et al.* (2019). In this study, we identify test cases from ICESat-2 and ATM altimetry data and use these pilot cases to develop an algorithm for detecting supraglacial lakes and retrieving lake depth. The algorithm is designed as a semi-automatic method to find supraglacial lakes within select altimetry granules.

2.2 Data Description

2.2.1 ICESat-2

ICESat-2 is a polar orbiting satellite with an inclination of 92 degrees that carries the Advanced Topographic Laser Altimeter System (ATLAS), a 532 nm micro-pulse laser that is split into six distinct beams with names based on the ground track: GT1L/R, GT2L/R, and GT3L/R. The beams are configured in pairs with a 90-meter separation between beams within a beam-pair and 3.3-kilometers between pairs. With an operational altitude of ∼500 km and a 10 kHz pulse repetition rate, ICESat-2 records a unique laser pulse approximately every 0.7 m along-track over a 91-day repeat cycle.

The ATLAS product used here is the ATL03 Global Geolocated Photon Data V002 (*Neumann et al.*, 2019a), which consists of retrieved photons tagged with latitude, longitude, received time, and elevation. Each photon pulse also carries a classification as either signal or background (noise). The differentiation between signal and background is performed using a statistical algorithm outlined by *Neumann et al.* (2019b). Signal photons are further classified by confidence level, such that photons labeled as "high confidence" are most likely to originate from the surface. Generally, cloudy or variable profiles exhibit "medium/low confidence" or noise photons, whereas low slope surfaces, such as water and ice sheets, result in more "high confidence" photons (*Neumann et al.*, 2019b). In thin layers of water, high confidence photons are observed from both the water surface and the underlying ice.

Our study focused on the central strong beam (GT2L), as the number of lakes was deemed sufficient for our purposes. While we recognize that the other strong beams could be useful for depth retrievals, we did not consider them here. We speculate that the weak beams may avoid issues with multiple scattering and specular reflection, but their power is too low to reliably detect lakes deeper than 4 m. Ground-based validation by *Brunt et al.* (2019b) indicates an accuracy of <5 cm in ATL03 photons over ice sheet interiors. The use of medium, low, and "buffer" photons slightly decreases measurement precision, but a less truncated transmit pulse gives better agreement with ATL06 and ground-based data (*Brunt et al.*, 2019b).

2.2.2 Airborne Topographic Mapper

The Operation IceBridge (OIB) campaign was designed to fill the gap in polar altimetry between ICESat and ICESat-2. Its scientific payload included the Airborne Topographic Mapper, a 532 nm lidar that has been used for ice sheet and shallow water measurements since 1993. The ATM lidar conically scans at 20 Hz, providing a 400 m swath width along-track (*Brock et al.*, 2002; *Krabill et al.*, 2002). The

ATM Level-1B Elevation and Return Strength (ILATM1B) product converts analog waveforms into a geolocated elevation product to emulate ATLAS data (*Studinger*, 2018). Although it lacks a statistical confidence definition, ATM applies a centroid model to digitized waveforms to retrieve high-confidence photons. *Brunt et al.* (2019a) found that ATM errors were -9.5 to 3.6 cm relative to ground-based measurements. Here, the ATM results presented serve as a proof of concept for the lake detection algorithm.

2.3 Methods

2.3.1 Lake Detection

Supraglacial lake surfaces are much flatter than surrounding terrain. We thus performed topography checks with the expectations that (i) lake surfaces would be identifiable in photon histograms and (ii) lake beds may be found via statistical inference in the region of the lake surface. To simplify the identification of lake features, we separated them into two arrays: one for the surface and one for the bed, which we refer to as "lake surface-bed separation" (LSBS). For both lidars, the procedure for separation was identical, and is as follows (see Figure 2.1 for a schematic view):

i. We divided each data granule into discrete along-track windows to reduce the data volume to $\sim 10^4$-10^5 photons per window. This photon count is equivalent to ∼1-10 km in along-track distance for ICESat-2 and ∼0.15-1.5 km for ATM. If a supraglacial lake appeared on the edge of the window, the window size was adjusted to include the full observed water feature.

ii. Each data window was binned into elevation-based histograms. We assumed that the lake surface dominates the total bin count within each window of photons. We check the flatness of the window by computing the standard

deviation (σ) of high-confidence signal photons within the upper 85th-percentile of bin count. We define a "flat" surface for regions where $\sigma \leq 0.05$ m for ATL03 data, and ≤ 0.02 m for ILATM1B data. We selected these values by comparing the "flatness" of lake surfaces to that of surrounding ice topography. If data were within the appropriate flatness threshold, they were verified as a lake surface using Landsat-8 OLI imagery. This step was included to filter non-glacial features, such as ocean or fjords.

iii. If the satellite image(s) confirmed the presence of a lake, the data were assigned to a new array for the height of the lake surface ($\underline{h_{sfc}}$). The horizontal extent of the lake surface served as a constraint for where the lake bottom data could be defined. Within these horizontal bounds, photons were defined as a lake bottom if they satisfied the condition: $h_{sfc} - a\,\sigma_{sfc} \leq h \leq h_{sfc} - b\,\sigma_{sfc}$, where σ_{sfc} is the standard deviation of lake surface photons. The constraints a and b were derived through trial-and-error, such that $a = 1.0(1.8)$ and $b = 0.5(0.75)$ for ICESat-2 (ATM). We set these constraints to reduce the impacts of multiple scattering and specular reflection on depth estimates. If these conditions were met, then the data were placed in an array for the height of the lake bottom, $\underline{h_{btm}}$.

iv. A series of filters were applied to improve surface/bed estimates. For ICESat-2, lakes shallower than 1.3 m or smaller than 200 m in horizontal extent were considered too noisy or ill-defined for further analysis (see Section 5.2 for more details). To remove water bodies with deep bed returns (e.g., oceans or fjords) or with no bed returns, the algorithm counted the number of bed photons present for both lidars. If the number of bed photons was very small (100 or less), then the scene was marked as a probable false positive.

v. If the data were obtained from ICESat-2, then we followed a photon refinement

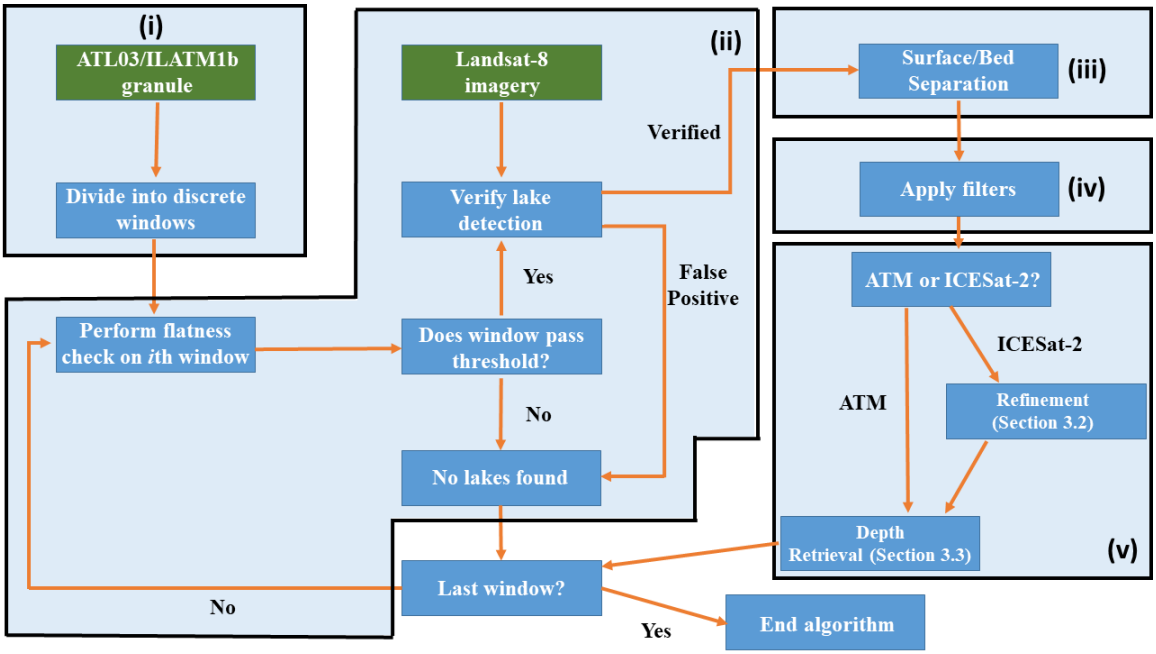

Figure 2.1: Schematic for the workflow of the lake surface-bed separation algorithm.

routine that is described in more detail in Sect. 3.2. Calculations for lake depth were then performed for both ATM and ICESat-2 retrievals and corrected for refraction (Sect. 3.3).

2.3.2 ATL03 Refinement

The above steps were sufficient to obtain lake profiles within the ATM data, but melt lake bottoms observed by ICESat-2 were significantly noisier as a consequence of higher background (noise) photon rates. After the initial LSBS procedure, we manually assessed bed estimates for each lake. For lakes that did not pass qualitative assessment, we adopted photon refinement procedures initially used for the ATL06 surface-finding algorithm (*Smith et al.*, 2019). In short, ATL03 photon aggregates within overlapping 40 m segments were used to estimate lake surfaces and beds with greater precision via least-squares linear fitting applied to the aggregates. These linear fits were used to approximate a window of acceptable surface or bed photons

for every 20 m along-track. A more detailed description of the ATL06 algorithm is given in *Smith et al.* (2019).

The linear regression in ATL06 accounts for all ATL03 photons (background or signal), and the technique performs a background-corrected spread estimate to narrow the range for acceptable photons. This is an iterative scheme; the refinement process repeats its acceptable photon filter until no photons are removed. As a consequence, the ATL06 algorithm assumes a single returning surface, so over a melt lake it will compute a height for either the lake bottom or the lake surface, depending on their return strengths.

The condition for acceptable surface photons in ATL06 is given by:

$$|r - r_{med}| < 0.5H_w \tag{2.1}$$

Within a 40 m photon segment, r is the residual of a photon relative to the linear regression, r_{med} is the median residual, and H_w is window height. The height of the window is taken as the maximum of the observed photon spread, the window height (if any) and 3 m, and photons within the window range are defined as the surface. The LSBS algorithm follows a similar procedure, but the flatness of the lake surface and relatively low photon density of the corresponding beds rendered iterating unnecessary. The lake bed is then defined as photons not within the window and below the surface. In other terms, lake bed photons satisfy the conditions:

$$|r - r_{med}| > 0.5H_w, \quad h < h_{sfc} \tag{2.2}$$

As with the initial guess, the lake bottom was only defined within the horizontal bounds of the lake surface, and the improved guesses were assigned to h_{sfc} and h_{btm}.

As a final adjustment to lake photons, we applied a refraction correction algorithm to account for slowing down of light as it enters water. The correction follows the

methods utilized by *Parrish et al.* (2019) by approximating refractive biases as a function of depth and beam elevation angle. The center strong beam for ICESat-2 is near-nadir, so the horizontal offset was determined to be small relative to the size of lakes (∼3 cm, far below the horizontal geolocation uncertainty for ICESat-2). However, vertical offsets of 1 m or more were found for lakes ≥4 m in depth, necessitating the use of refraction correction.

2.3.3 Lake Depth and Extent Estimations

Once we obtained h_{sfc} and h_{btm}, lake depth from the altimeter signal (z_s) was estimated using:

$$z_s = \overline{h}_{sfc} - \overline{h}_{btm} \tag{2.3}$$

where $\overline{h}_{sfc}$ and $\overline{h}_{btm}$ represent the moving mean of the surface elevation and the bottom elevation, respectively. The moving mean was used to account for signal attenuation and scattering at the lake bottom, a problem most evident for ICESat-2 retrievals.

For deep or inhomogeneous lakes, attenuation of photon energy in water resulted in fewer signal photons observed at lake bottoms (Figure 2.4). In these situations, we fitted polynomial or spline fits to all lake profiles with bounds at the lake edges. Lakes observed by ATM typically featured "bowl" shapes and attenuation at the deepest parts, so 3rd-order polynomials were sufficient. In ICESat-2 data, the retrieved lake beds showed greater complexity, so we tested polynomial fits and splines on a case-by-case basis. Lake depths approximated with curve fitting were denoted as z_p. We compare z_s and z_p over lakes with well-defined bottoms, and show in Sect. 4 that the two generally agree to within 0.88 m.

To test the limits of the algorithm relative to lake size, we utilized the great-circle formula (ATM) or pre-defined along-track distance (ICESat-2) to approximate

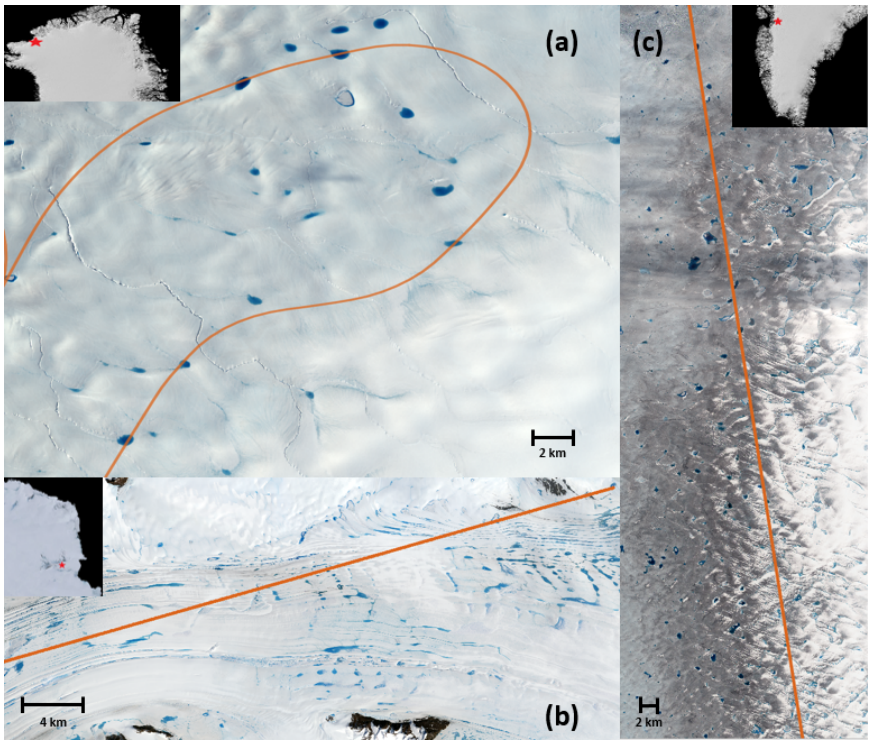

Figure 2.2: True-color Landsat-8 composites of Hiawatha Glacier on 18 July, 2017 (a), the Amery Ice Shelf on 1 January, 2019 (b), and the western Greenland ablation zone on 17 June, 2019 (c). Flight tracks for Operation IceBridge (a) and ICESat-2 (b, c) are shown in dotted orange.

along-track extent L. We acknowledge the desire to retrieve lake volume from laser altimetry, but we leave the development of such an algorithm for a future study. For example, depth retrievals from ICESat-2 could potentially be combined with lake radius and shape estimations determined from visible satellite imagery to derive water volume.

2.3.4 Case Study Locations

We present cases over the Amery Ice Shelf on 2 January, 2019 (ICESat-2 Track 0081; 68.271-73.798°S, 63.057-78.620°E), the western Greenland ablation zone for 17 June, 2019 (ICESat-2 Track 1222; 66.575-69.582°N, 48.284-49.239°W), and Hiawatha Glacier in 19 July, 2017 (ATM; 77.780-79.3119°N, 65.279-67.484°W) (Figure 2.2). Comparisons between Landsat-8 imagery and ICESat-2/OIB flight tracks confirmed

supraglacial lake overpasses for study. In Spring 2019, an early onset of the Arctic melt season resulted in both ICESat-2 and Operation Icebridge surveying supraglacial lakes near Jakobshavn Isbræ in May. However, there were no lakes sampled at the time by both ICESat-2 and OIB.

2.4 Results

We detected 12 melt lakes with sufficient bed returns from the ATM data and 16 potential melt lake surfaces overall. The melt lake profiles are shown in Figure 2.3, with maximum depths of 0.98-7.38 m and extents of 180-730 m. The algorithm reliably distinguishes between lake surfaces and the surrounding ice terrain. The mean spread among lake surface photons is 0.0087 m, or well within the flatness threshold of 0.02 m. Lake bottoms are well-defined when $d_s < 8$ m. Lake bottoms deeper than 8 m exhibit fewer signal returns, for the associated return signal is below the threshold required to be digitized (*Martin et al.*, 2012). The average depth estimate for the lakes in Figure 2.3 was 1.95 m (Table 2.1), and lakes at this depth typically featured adequate bed returns. In deeper lakes, the polynomial estimate produced reasonable guesses for the lake bed location, with the most effective fitting seen in lakes 2.3e, 2.3g, and 2.3h. With the polynomial-based depths, mean lake depth increased to 2.15 m, and the maximum modeled depth was 8.83 m.

The spread in ATM lake bed photons is low (Table 1, Column 7), with a maximum of 0.2 m for lake 2.3g. The highest uncertainties are observed for lake depths greater than 3 m, perhaps influenced by low signal-to-noise ratios or the conical scanning of the OIB lidar instrument. Polynomial estimation errors are 0.41 m on average. Several depth errors are below this mean, but a strong standard error (1.03 m) in lake 2.3g, due to difficulties in capturing its steep bed slope, slightly skews the mean error. Excluding this value, the mean error among ATM polynomial estimates reduces to 0.35 m.

Table 2.1: Cumulative statistics for ATM supraglacial lakes explored in this study, including mean and maximum signal-based depth (d_s) and polynomial-based depth (d_p), along-track extent L, mean lake depth uncertainty ($\overline{\sigma}_d$), and mean polynomial estimation error ($\overline{\epsilon}_p$). Units are in meters.

Lake	$\overline{d}_s$	$max(d_s)$	$\overline{d}_p$	$max(d_p)$	L	$\overline{\sigma}_d$	$\overline{\epsilon}_p$
3a	0.98	1.69	0.91	1.51	270	0.08	0.31
3b	2.25	3.75	2.32	3.49	640	0.15	0.45
3c	1.33	2.39	1.33	2.24	440	0.09	0.25
3d	0.64	0.98	0.71	1.09	180	0.10	0.38
3e	1.81	2.98	2.37	4.11	520	0.05	0.42
3f	1.70	2.70	1.97	3.15	470	0.10	0.49
3g	4.32	7.38	5.50	8.83	630	0.20	1.03
3h	3.64	5.91	3.90	6.37	730	0.15	0.41
3i	1.56	2.38	1.48	2.37	510	0.12	0.15
3j	3.17	5.18	3.39	5.29	650	0.11	0.65
3k	0.60	1.06	0.55	0.97	350	0.09	0.21
3l	1.45	2.32	1.39	2.18	590	0.11	0.15
Mean	1.95	3.23	2.15	3.47	500	0.11	0.41

Table 2.2: As with Table 1, but for ICESat-2 tracks.

Track	Lake	$\overline{d}_s$	$max(d_s)$	$\overline{d}_p$	$max(d_p)$	L	$\overline{\sigma}_d$
0081	4a	2.32	4.57	2.62	4.00	3170	0.25
	4b	1.48	2.67	1.48	1.70	8570	0.80
	4c	2.02	2.86	2.08	2.41	3790	0.28
	4d	1.39	2.32	1.46	1.96	3860	0.77
	Mean	1.80	3.11	1.91	2.52	4850	0.53
1222	4e	2.24	3.43	2.28	2.98	1990	0.28
	4f	2.31	5.22	2.66	3.44	2980	0.26
	4g	3.52	7.15	3.76	5.78	1370	0.49
	4h	1.22	1.47	1.24	1.50	211	0.12
	4i	1.52	2.88	1.55	2.37	2070	0.23
	4j	4.13	6.56	4.13	6.01	530	0.73
	4k	1.65	3.13	2.04	3.08	780	0.22
	4l	1.93	2.76	1.93	2.78	360	0.15
	Mean	2.32	4.08	2.45	3.49	1290	0.31

We examined an additional 12 supraglacial lakes with ICESat-2, eight in Greenland and four on the Amery Ice Shelf in Antarctica. Three of the Antarctic melt lakes (2.4a, 2.4b, 2.4d) are highlighted in *Magruder et al.* (2019) and *Fricker et al.* (2021). The refined algorithm captures lake surfaces and beds reasonably well (Figure 2.4), with a mean uncertainty of 0.015 m for surface photons and 0.38 m for bed photons. The lake edges partially account for the bed photon uncertainty, for the limited number of acceptable photons produces a slight bias in bed estimates. Antarctic melt lakes were generally shallower than those seen on Greenland (Table 2.2) - only lake 2.4a exceeded 3 m in depth, whereas the mean maximum depth over Greenland was 4.08 m. Melt lakes on the Amery Ice Shelf were 3-8 km in extent, thus facilitating detection in histograms. Greenland lakes exhibited a wider range of sizes, but the algorithm successfully performed retrievals for lakes as small as 200 m in extent.

On average, the noisier data from ICESat-2 produces uncertainties greater than 0.2 m for the Antarctic lakes and 0.3 m for the Greenland lakes, as seen in Table 2.2, Column 8. The inclusion of lower-confidence photons increases uncertainty despite the restricted bed photon criteria, for the larger photon cloud increases the spread of the entire lake profile. The curve fits improved depth estimates for lakes 2.4b, 2.4f, and 2.4i. Of these lakes, only 2.4i used a polynomial estimate due to poor spline fitting. The inclusion of interpolants increased the mean depth estimates of 2.4b, 2.4f, and 2.4i by 0.08 m, 0.04 m, and 0.03 m, respectively. The spline fitting significantly increased the maximum observed depth in lake 2.4b from 2.67 m to 3.27 m. The remaining lakes featured more complete bed profiles, meaning that the fitting estimates were less important.

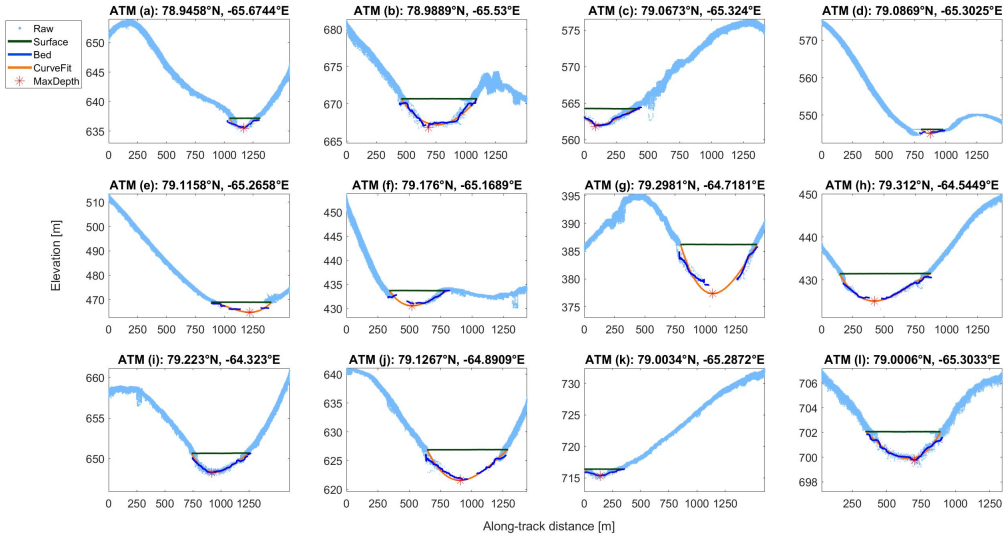

Figure 2.3: ATM lake profiles from 17 July, 2017 fitted using lake surface-bed separation, including the raw ILATM1B product, the lake surface signal, the lake bottom signal, the polynomial-/spline-fitted bottom, and the point of maximum depth. Along-track distance is relative to the start of a data granule.

2.5 Discussion

2.5.1 Algorithm Performance

The conical scanning of the ATM lidar produced oscillations in 1D elevation profiles that dampened over lake surfaces, so lakes generally were easier to identify with the airborne retrievals. Flights conducted during the OIB campaign actively avoided cloudy conditions, reducing attenuation sources and further simplifying the lake-finding process over common melt regions. The data volume per granule was lower than ATL03, resulting in less time needed to run the algorithm. However, the number of retrievals possible with ATM is limited, so observations with the lidar best serve as a validation and correction tool for ICESat-2 and other retrieval methods.

The laser power and detector sensitivity of the ATLAS instrument on board ICESat-2 are sufficient to reliably detect lake beds, and a high along-track resolution

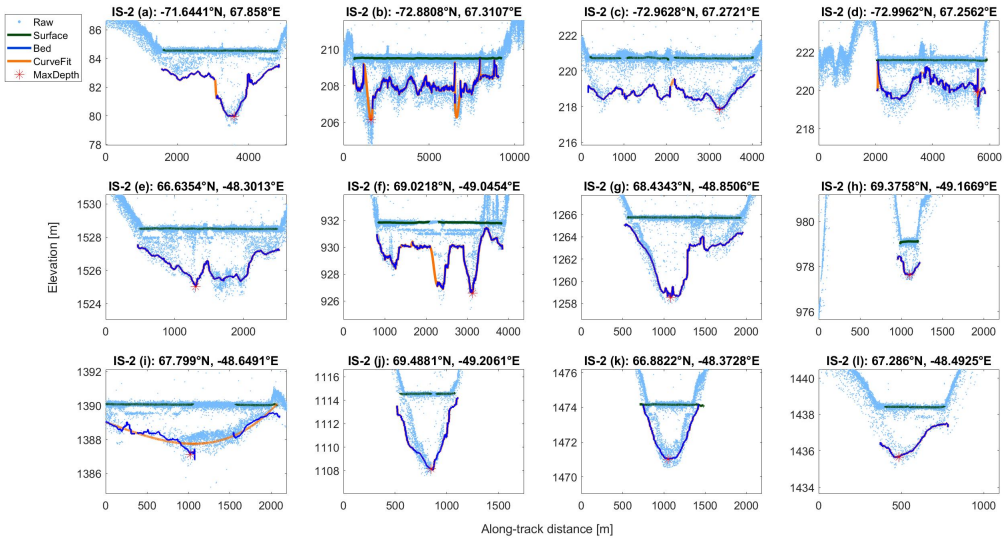

Figure 2.4: Supraglacial lakes and melt ponds detected by ICESat-2 over the Amery Ice Shelf (a-d) and western Greenland (e-l), using Tracks 0081 and 1222, respectively.

will correspond to improved estimates of lake bed topography, water depth, and water volume. Despite strong advantages, significant difficulties must be considered before automatic lake detection is feasible. At its operational altitude, the ATLAS laser is subject to first-photon-bias, solar background radiation, and scattering and absorption by blowing snow and clouds. Clouds are common over the fringes of Antarctica and Greenland (*Bennartz et al.*, 2013; *Lachlan-Cope*, 2010; *Van Tricht et al.*, 2016), and often their optical depth is sufficient to render the surface undetectable. Handling the large data volumes in ATL03 granules also presents a significant challenge. A single granule provides coverage over hundreds of kilometers, so the running time of the algorithm increases relative to ATM granules. Lakes smaller than 1 km are difficult to automatically detect with the algorithm, but LSBS may still be performed for lakes as small as 200 m if the location of a lake is known through other means (e.g., Landsat-8 imagery or ATM retrievals).

We observed differences in lake topography for ICESat-2 lakes, and we attribute

them to the underlying ice surfaces. Supraglacial lakes on Greenland typically form into smooth basins within depressions formed by the underlying bedrock, and their location is independent of ice motion (*Echelmeyer et al.*, 1991). In contrast, meltwater on the Amery Ice Shelf originates from the blue ice zone, propagating along the ice surface in streams. The location of lakes and ice topography are thus tied to the flowlines of the ice shelf surface. These features are flooded in the Antarctic melt season, producing melt lakes and streams up to 80 km in length (*Mellor and McKinnon*, 1960; *Phillips*, 1998; *Kingslake et al.*, 2017).

A potential issue for lake depth retrievals concerns specular reflection. When photons interact with a flat water surface, they may reflect directly back to the detector with minimal energy loss. The excessive return energy produces a "dead time" in the ATLAS detector, and the return signal is represented by multiple subsurface returns below the actual surface (*Neumann et al.*, 2020). An example of this phenomenon may be seen in Figure 2.4f, where a prominent subsurface return 1 m below the true surface is featured along the lake extent. However, because the subsurface echo is smaller than the true surface when viewed through histograms, the LSBS algorithm is able to avoid biases caused by specular reflection.

The success of this method for lake depth retrievals is governed by spatial and temporal sampling of the instruments across the lakes when they are full. The methods presented here are most effective when the altimeter passes directly over the deep part of a lake rather than at its edge. This provides a lake depth profile that is more representative of the complete lake, allowing for improved estimates of lake depth and extent. A complete lake profile also provides sufficient information to the LSBS algorithm, reducing the risk of false negatives that occur with small lakes or incomplete profiles. The temporal sampling of ICESat-2 and ATM is infrequent (every 91-days for ICESat-2 and random for ATM), and so the same lakes will not always be present every time these data are required. Therefore, coincident satellite imagery is desirable

to simplify the lake-finding process.

2.5.2 Automation Challenges

The identification of lake beds in the LSBS algorithm is based on a window of acceptable photons. The photon window is constrained by the coefficients a and b (for ICESat-2, $a = 1.0$, $b = 0.5$). Lake beds detected in this manner had a height uncertainty of 0.38 m (Table 2). The coefficients for ATM ($a = 1.8$, $b = 0.75$), resulted in more accurate retrievals on an individual basis. However, implementing varying a and b values proved difficult to automate, as other values may produce more accurate depths.

The challenges in full automation are related to three key issues. First, the observed extent of lakes varied considerably, especially over Greenland. The diversity in lake sizes complicated attempts to derive a universal "flatness" check. Smaller lakes present fewer lake surface photons, so a smaller data window ($\sim 10^4$ photons) is required to prevent false positives. However, larger lakes may not be fully represented in smaller windows. A larger data window ($\sim 10^5$ photons) will fully capture the largest lakes, but smaller lakes may then be overlooked.

Second, multiple scattering at the lake bed increases the photon spread and thus also increases the uncertainty of depth retrievals. Most supraglacial lakes observed by ATM featured smooth beds, so photons experienced one or few scattering events before returning to the detector. The instrument digitizer automatically filters return signals with low photon counts, reducing the spread of bed photons, at the cost of deep lake bottom detection. In contrast, the lakes observed with ICESat-2 exhibited more heterogeneous beds, leading to increased scattering events by photons and delays in return pulses. In these cases, the given values for a and b may not produce the most accurate bed solution. Furthermore, if the return is significant for a given photon window, then it may lead to a false negative for a portion of the lake (Figure 2.4i).

To reduce uncertainty in lake depth retrievals, future improvements in working with ICESat-2 data should focus on identifying and filtering multiple scattering.

Finally, the ATL03 signal-finding algorithm is conservative in that it accepts false positives (background photons classified as signal photons) to ensure that all signal photons are passed to higher-level products. Thus, uncertainties in the ATL03 photon classification contribute to noise in the water column and the lake bed. The classification algorithm uses pre-defined surface masks to allocate statistical confidence to ATL03 photons for multiple surface types (e.g. "*inland water*", "*land ice*", "*land*"), with overlap possible between masks (*Neumann et al.*, 2020). Melt lakes are categorized as "*land ice*" (lake surface) and "*land*" (lake surface and bed). Because the "*land*" classification also includes the bed, it includes more potential signal photons than *land ice*, so our recommendation is to only use *land* photons for supraglacial lake depth retrievals. It must be noted, however, that a lake bed profile is fully resolved only with the inclusion of low-/medium- confidence and "buffer" photons. The buffer photons ensure that all photons identified as surface signal are provided to the appropriate upper-level data product algorithms. However, they can introduce greater noise to the profile, so more sophisticated filtering techniques are needed to distinguish between signal photons and the solar background.

2.6 Conclusions

We present a method to detect supraglacial lakes and estimate lake depth from 532 nm laser altimetry data. We establish test cases for lake detection over two regions of Greenland (Hiawatha Glacier, 19 July, 2017 and Jakobshavn Isbræ, 17 June, 2019) and East Antarctica (Amery Ice Shelf, 2 January, 2019), and our results demonstrate that depth retrievals are possible using laser altimetry. Verification of lake detection is given with lake surface flatness tests, where we observe low topographical variance over lake surfaces relative to surrounding ice. Lake bottoms are easy to identify once

lake surfaces are established, given that the lakes are not deeper than 7 m.

We introduce lake a surface-bed separation scheme for ATM and ICESat-2 geolocated photon data to determine the maximum depth of lakes. Our results indicate that altimetry signals reliably detect bottoms as deep as 7 m, after which absorption of the photons in water reduces the number of reflected photons. Heterogeneity at the lake bed also produces attenuation, complicating retrieval attempts for lakes with rough bed topography or with high impurity concentration. Additional work is required to assess the impacts of lake impurities and geometry on altimetry signals and to improve estimates for such cases. Despite these shortcomings, we anticipate retrieval capability to improve as observations from the 2019 and 2020 Arctic melt seasons are released.

We establish the feasibility for estimates of supraglacial lake depth over Antarctica and Greenland. The high accuracy of 532 nm laser altimeters allow these results to serve as a benchmark for future retrieval studies. Future studies need to examine the accuracy of ICESat-2 lake retrievals relative to ATM where applicable, with additional comparisons to depth estimates from passive imaging sensors.

CHAPTER III

Sensitivity of Snow Grain Size Retrievals

Abstract. Snow effective grain size (r_{eff}) can be derived from spaceborne and airborne radiance measurements due to strong attenuation of near-infrared energy by ice. Consequently, a snow grain size inversion technique that uses hyperspectral radiances and exploits variations in the 1.03 μm ice absorption feature was developed for use with airborne imaging spectroscopy. A suite of studies has since demonstrated the effectiveness of the technique, though there has yet to be a quantitative assessment of the retrieval sensitivity to other snowpack properties or solar geometry. In this study, we use the Snow, Ice, and Aerosol Radiative (SNICAR) model and a Monte Carlo photon tracking model to examine the sensitivity of snow grain size retrievals to changes in dust and black carbon content, anisotropic reflectance, changes in solar illumination angle (θ_0), and scattering asymmetry parameter (g). Our results show that changes in these variables can produce large grain size errors, especially when $r_{eff} \geq 500$ μm. Dust content of 1000 ppm induces errors exceeding 800 μm, with the highest biases associated with small particles. Aspherical ice particles and perturbed solar zenith angles produce maximum biases of $\sim$600 μm and $\sim$400μm respectively, when spherical snow grains and $\Delta\theta_0 = 60^\circ$ are assumed in the generation of the retrieval calibration curve. Retrievals become highly sensitive to viewing angle when reflectance is anisotropic, with biases exceeding 1000 μm in extreme cases.

We demonstrate that knowledge of snowpack state and solar geometry are important when determining snow grain size through hyperspectral remote sensing.

3.1 Introduction

The optical grain size of snow is a critical factor in the determination of snowpack albedo and metamorphism. The term "optical grain size" does not refer to the actual size of individual snowflakes, but instead represents the radius of snow particles as simple shapes, such as spheres or rods. These simplified shapes have optical properties that are similar to those of the actual snow grains (*Warren*, 1982). Snow grains experience rapid changes in size and morphology after snowfall, notably once the snowpack is warmed to its melting point. In dry snow, the gradual coarsening of individual snow grains decreases albedo and enhances the warming process (*Picard et al.*, 2012). The presence of liquid water or light absorbing impurities also accelerates snow metamorphism, leading to positive feedbacks between grain growth and snow albedo (*Skiles et al.*, 2017; *Tuzet et al.*, 2017). Grain size has a limited impact on albedo in the visible spectrum, but albedo in the near-infrared varies inversely with optical grain size (*Wiscombe and Warren*, 1980). Thus, snow grain size is a vital component of snowpack modeling.

The importance of snow grain size has led to the development of retrieval algorithms from spectral reflectance and spectral imaging. Qualitative classifications of grain size were presented by *Dozier and Marks* (1987), who used Landsat Thematic Mapper data to sort snow into coarseness regimes. *Nolin and Dozier* (1993) introduced the first quantitative approach using radiance data from a single spectral band of the Airborne Visible/Infrared Imaging Spectrometer (AVIRIS). A more sophisticated technique was developed by *Nolin and Dozier* (2000) that utilized multiple AVIRIS bands centered at the ice absorption feature at 1.03 μm to generate an inversion model. A suite of studies has applied the Nolin and Dozier method (henceforth

referred to as ND2000) since its inception through contact and imaging spectroscopy (*Donahue et al.*, 2020; *Dozier et al.*, 2009; *Painter et al.*, 2007, 2013; *Seidel et al.*, 2016; *Skiles et al.*, 2017).

Studies using the ND2000 retrieval algorithm often rely on three assumptions: (i) individual ice particles are treated as spheres (*Donahue et al.*, 2020; *Painter et al.*, 2007), (ii) the snowpack impurity content is negligible (*Nolin and Dozier*, 2000; *Seidel et al.*, 2016), and (iii) illumination and viewing angles need to be considered (*Donahue et al.*, 2020; *Nolin and Dozier*, 2000). Previous studies established that the spherical particle assumption works for bulk albedo calculations (*Grenfell et al.*, 2005; *Grenfell and Warren*, 1999; *Neshyba et al.*, 2003), but it overestimates the scattering asymmetry parameter (g), leading to inaccuracies in snow radiative transfer models that assume spheres (*Dang et al.*, 2016; *Kokhanovsky and Zege*, 2004; *Libois et al.*, 2013). Furthermore, if dust content is sufficiently high, the dust may increase albedo at near-infrared wavelengths and interfere with grain size retrievals (*Nolin and Dozier*, 2000).

If a surface is a diffuse reflector (i.e. reflects light in all directions equally), it is known as a Lambertian surface because reflectance can be described by Lambert's cosine law. Snow can be assumed to be a Lambertian surface when the solar illumination angle is near-nadir over flat surfaces. However, snow reflectance in the NIR is anisotropic, preferentially scattering light in the forward direction at higher illumination angles (*Dumont et al.*, 2010; *Li*, 2007; *Picard et al.*, 2020). Because snow is typically found at high latitudes or on sloped terrain, the illumination and viewing angles must be considered when retrieving snow properties from spectral reflectance. Therefore, a quantitative assessment of the potential impacts of solar geometry and snowpack state on the ND2000 algorithm is needed.

In this study, we used radiative transfer models to examine the sensitivity of snow grain size retrievals to changes in dust content and anisotropic reflectance. We per-

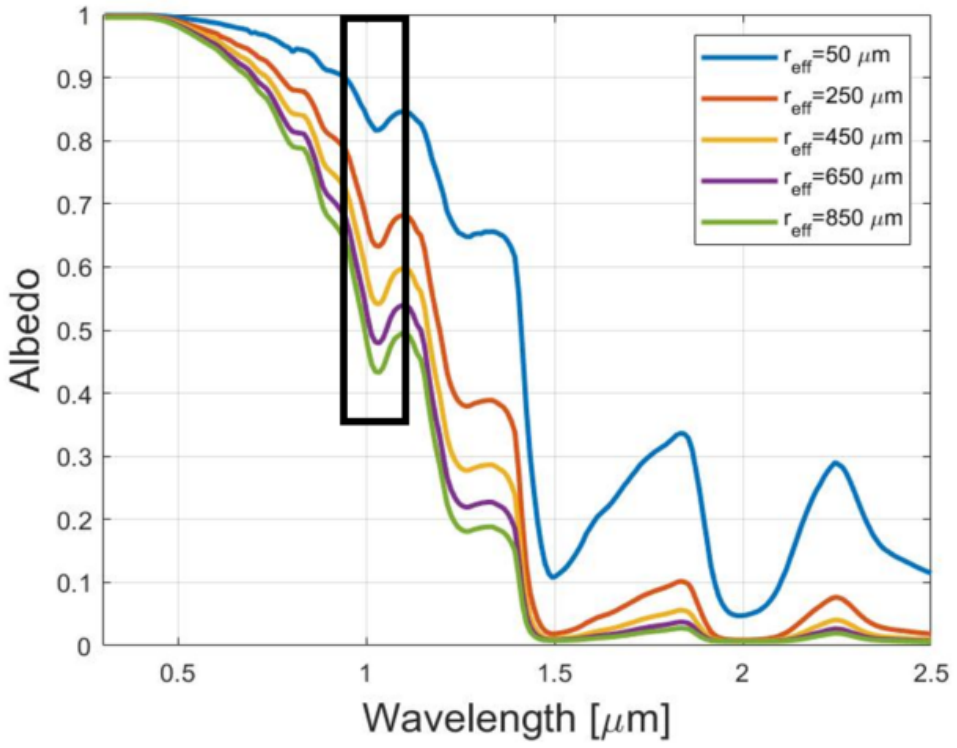

Figure 3.1: The spectral dependence of snow directional-hemispherical albedo as a function of effective snow grain size, as derived by SNICAR. The black box highlights the domain used for grain size retrievals.

formed additional analyses for changes in solar zenith angle and scattering asymmetry parameter to examine sensitivity to solar geometry and ice particle asphericity. The paper is organized as follows: we first describe the methods we used to assess grain size sensitivity, and the radiative transfer models used for this purpose. Section 3 shows the results of our sensitivity tests and discusses the implications for actual grain size retrievals. Section 4 concludes the paper with recommendations for future work.

3.2 Methods

3.2.1 General description of grain size retrievals

The ND2000 technique estimates snow grain size using directional reflectance at the ice absorption feature centered at 1.03 μm. Reflectance in this feature decreases as snow grain size increases (3.1), leading to an increase in depth of the absorption feature. Preliminary research by *Nolin and Dozier* (1993) demonstrated that band depth at 1.04 μm could be used to derive snow grain size, though the method was subject to sensor noise and uncertainties due to local topography. *Nolin and Dozier* (2000) accounted for the latter issue by scaling band depth relative to continuum reflectance, or the reflectance linearly interpolated between 0.95 μm and 1.09 μm. This scaling generates a continuum-removed spectrum that is independent on the magnitude of reflectance. The former issue was accounted for by instead deriving a scaled band area:

$$A_{b,s} = \int_{0.95\mu m}^{1.09\mu m} \frac{R_c - R_b}{R_c}\, d\lambda \tag{3.1}$$

where R_b is the spectral reflectance and R_c is the continuum reflectance. The term inside the integrand of Equation 3.1 is the scaled band depth at each wavelength within the absorption feature.

Band area is computed from an observation of spectral reflectance and best matched to a band area within a lookup table or to a calibration curve of modeled band areas. Previous studies derived lookup tables of scaled band area using the Discrete-Ordinates Radiative Transfer (DISORT) model (*Stamnes et al.*, 1988). Here, we instead derived calibration curves using the SNICAR model (*Flanner et al.*, 2007) and a Monte Carlo photon tracking model (*Schneider et al.*, 2019) to derive hemispherical albedo and directional reflectance, respectively. We fitted a second-

order polynomial to each calibration curve to relate grain size to band area for a given set of solar zenith angles. We also used SNICAR and the Monte Carlo model to produce synthetic observations of hyperspectral snow albedo to assess the influence of snowpack variables. This allowed us to evaluate how these features affect grain size retrievals when they are or are not considered in the creation of the retrieval function.

We quantified the bias of simulated grain size retrievals (Δr) as the difference between retrieved grain size (r') and the true grain size (r_0):

$$\Delta r = r' - r_0 \tag{3.2}$$

If Δr is negative, then the retrieved grain size is smaller than the actual grain size. Conversely, a positive Δr implies a larger retrieved grain size than the actual snow grain size.

3.2.2 Simulated snowpack perturbations

3.2.2.1 SNICAR

The Snow, Ice, and Aerosol Radiative (SNICAR) model incorporates a two-stream radiative transfer solution derived by *Toon et al.* (1989) over a single-layer, semi-infinite snowpack to simulate spectral reflectance at 10 nm resolution. By default, ice particles are treated as spheres using Mie properties derived by *Warren and Brandt* (2008). Solar zenith angle and snow impurity optics serve as inputs to the model, allowing for estimates of spectral albedo given solar geometry or perturbed snowpack conditions. The SNICAR model is less computationally expensive than the Monte Carlo model, so we used it for case studies not focused on anisotropic reflectance, which is not resolved by two-stream models like SNICAR. As a baseline, we generated a calibration curve for snow grain sizes of 50-1000 μm at 50 μm intervals, assuming a solar zenith angle of 60° and zero impurity content. We compared the grain size

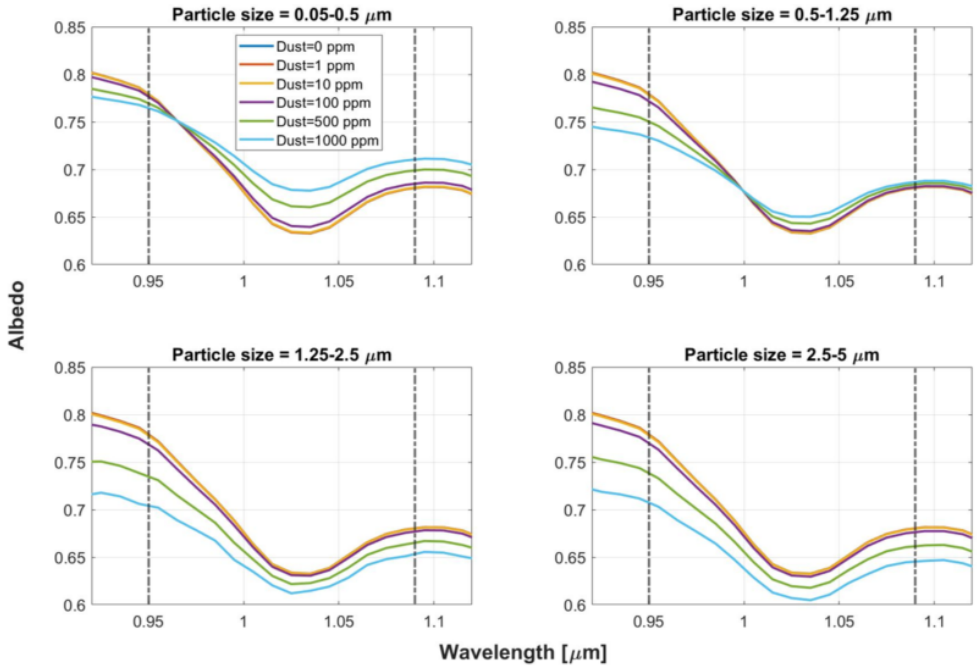

Figure 3.2: Spectral albedo of snow derived from SNICAR as a function of Saharan dust content at near-infrared wavelengths, given four particle size distributions and r_{eff} = 250 μm. The dashed lines indicate the bounds for band area calculations.

retrievals of perturbed snowpacks to this baseline when SNICAR was used.

3.2.2.2 Snowpack perturbations

We assessed each snowpack variable independently to highlight their individual effects on grain size retrievals. We assumed direct sunlight for all simulations. Spectra were modeled for a range of solar zenith angles (θ_0), asymmetry parameters, and LAP concentrations. For our analysis on solar zenith angle, we considered angles at near-horizon or near-zenith unlikely for most grain size retrieval conditions, so we restricted our simulations to $\mu_0 = cos\,\theta_0$ = 0.3, 0.4, 0.5, 0.6, 0.7. To mimic the influence of ice particle asphericity, we selected g values consistent with non-spherical particles previously determined by *Dang et al.* (2016), i.e. g = 0.75, 0.78, 0.81, 0.84, 0.87. The Mie properties used for spherical particles produce values of g = 0.88-0.9 over the part of the spectrum used for retrievals. The ice absorption feature contains slight

variations in g within this range, but these differences are negligible compared to the modeled perturbations. For cases of perturbed asymmetry parameter, we held g constant within the ice absorption feature. Grain size retrieval errors are calculated relative to calibration functions that do not account for variations in solar zenith angle or scattering asymmetry parameter.

We analyzed retrieval errors of contaminated snow with four different types of light-absorbing particles: Saharan dust (*Balkanski et al.*, 2007), San Juan dust (*Skiles et al.*, 2017), Greenland dust (*Polashenski et al.*, 2015), and black carbon. The Saharan and San Juan species were assessed at four size distributions: 0.05-0.5 μm, 0.5-1.25 μm, 1.5-2.5 μm, and 2.5-5.0 μm. The Greenland dust incorporated varying levels of absorptive potential (low, central, or high), whereas black carbon (BC) was analyzed for only one size distribution. We selected dust concentrations based on their impact on near-infrared reflectance. Dust only affects NIR albedo when its content is high ($\geq$100 ppm), otherwise changes are restricted to the visible spectrum (Figure 3.2). We therefore examined five concentrations for dust: 1 ppm, 10 ppm, 100 ppm, 500 ppm, and 1000 ppm. To account for its greater impacts on albedo, BC concentrations are given in amounts of parts-per-*billion* (ppb) rather than parts-per-million. Grain size retrieval errors are then calculated via calibration functions that assume pure snow.

3.2.3 Anisotropic reflectance modeling

3.2.3.1 Monte Carlo model

To analyze the importance of anisotropic reflectance, we used a Monte Carlo model originally developed by *Schneider et al.* (2019), which calculates azimuthally-averaged bidirectional reflectance factors (BRF) for idealized snowpack configurations. In the model, photons propagate through a highly scattering medium of ice particles until they are terminated (absorbed) or escape (reflected). Ice particles are configured as

spheres suspended in air, with their scattering asymmetry represented by the Henyey-Greenstein phase function (*van de Hulst*, 1968). Given solar zenith angle (θ_0) and reflected/viewing angle (θ_v), the BRF is calculated using

$$BRF(\theta_0;\theta_v) = \frac{\int_0^{2\pi} \Phi_r(\theta_v,\phi_v)\, d\phi_v}{2\Phi_i(\theta_0) sin(\theta_v) cos(\theta_v)} \tag{3.3}$$

where $\Phi_i(\theta_0)$ is the incident photon flux from solar angle θ_0 and $\Phi_r(\theta_v,\phi_v)$ is the photon flux received by a sensor at azimuth angle ϕ_v and elevation angle θ_v, assuming that 0° is nadir. The azimuthally-averaged BRF is defined using Lambert's cosine law, so the averaging requires a weighting factor of $\omega(\theta_v) = (2\, sin\, \theta_v\, cos\, \theta_v)^{-1}$. In this form, the BRF represents a ratio between actual reflectance and reflectance over a Lambertian surface.

3.2.3.2 Anisotropy configurations

We performed Monte Carlo simulations each with one million photons, which offered a compromise between reduced noise and increased computational expense. Photons that escaped from the top of the snowpack were used to estimate BRF using Equation 3.3. The calculated reflectances were distributed among 30 bins of zenith angle at 3°resolution for five snow grain sizes: 50 μm, 250 μm, 450 μm, 650 μm, and 850 μm. Although using fewer grain sizes reduces the resolution of the calibration curve, we deemed it a necessary step to reduce computational cost.

Spectral reflectance measurements are often made at near-nadir viewing angles (*Gao et al.*, 1993), so we tested for anisotropy at θ_v = 0-15°, which we henceforth refer to as the bidirectional reflectance or BRF. Directional reflectance calculated with Monte Carlo techniques is subject to random photon noise, so we applied a second-order polynomial fit to the spectral BRF output to smooth out noisy features. Preliminary analysis shows that directional-hemispherical reflectance derived from the Monte Carlo model agrees very closely with SNICAR hemispheric albedo at the

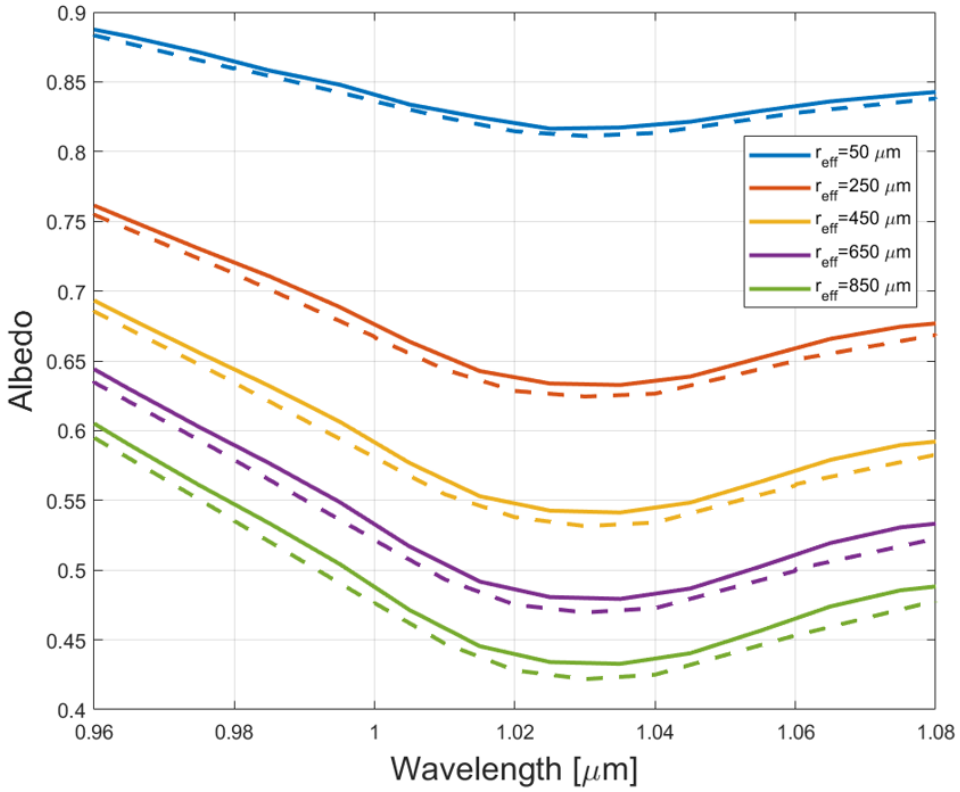

Figure 3.3: Spectral (directional-hemispherical) reflectance of snow without impurities calculated using the SNICAR model (solid) and the Monte Carlo model (dashed). The reflectances were derived for multiple grain sizes using $\theta_0 = 60°$.

given snow grain sizes (Figure 3.3).

Previous studies by *Nolin and Dozier* (2000) and *Donahue et al.* (2020) established that scaling band area relative to a continuum removes its dependence on the magnitude of reflectance, thereby reducing the impact of illumination angle variability. To validate this point, we performed additional anisotropy tests using unscaled band area $A_{b,u}$, which is given by

$$A_{b,u} = \int_{0.95\mu m}^{1.09\mu m} R_c - R_b \, d\lambda \tag{3.4}$$

For both scaled and unscaled band area, we performed three tests dependent on the reflectance quantities used for lookup table generation and for simulated retrievals. The first test applied a calibration curve derived from hemispheric reflectance and also assumed that hemispheric reflectance (i.e., albedo) is also the measured snow reflectance quantity. This configuration is equivalent to the snow grain size retrievals performed with SNICAR. The second test instead used BRF for the measured reflectance and left the calibration curve unchanged. Snow grain size retrievals performed with this configuration demonstrated the effects of anisotropy without corrections. The final test utilized BRF for both the calibration curve and the measured reflectance and thus served as a correction for anisotropy.

3.3 Results and Discussion

3.3.1 Solar zenith angle

For this analysis, the band areas used to create both the calibration curves and the modeled retrievals and the corresponding grain size errors were derived using hemispheric albedo from SNICAR. Our results for the solar zenith angle sensitivity study are given in Figure 3.4. Band area changes proportionally to the cosine of the illumination angle (μ_0), as reported by *Donahue et al.* (2020). Band area is most

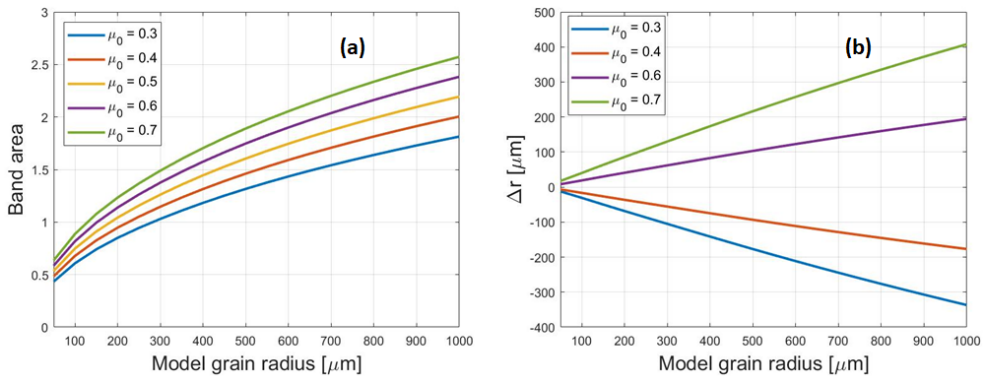

Figure 3.4: Band area as a function of grain size and solar zenith angle (a) and the corresponding grain size biases (b). The term "μ_0" refers to the cosine of the solar zenith angle. Biases are computed relative to the baseline calibration function assuming $\theta_0 = 60°$ ($\mu_0 = 0.5$)

sensitive to μ_0 when the Sun approaches the horizon ($\mu_0 = 0.3$ case), where reflectance is higher and less wavelength-dependent. When θ_0 is close to our calibration baseline of 60°, biases remain reasonably low for all but the largest snow grain sizes ($\geq$500 μm). Errors may exceed 300 μm as θ_0 deviates from the baseline, but otherwise remain within 100 μm.

When solar zenith angle changes, the likelihood of photon absorption within the snowpack also changes. Incident sunlight penetrates into a snowpack more effectively as θ_0 approaches zenith, allowing for more opportunities for absorption or multiple scattering and decreasing spectral albedo. To the retrieval algorithm, this "darker" surface corresponds to a deeper absorption feature, increasing scaled band area and apparent snow grain size. The opposite is true when θ_0 approaches the horizon. The biases described above illustrate the importance of incorporating solar zenith angle into the retrieval of grain size when applying the ND2000 algorithm.

3.3.2 Scattering asymmetry parameter

The results for our scattering asymmetry parameter sensitivity study (Figure 3.5) show a significant increase in bias when g deviates from values of spherical particles

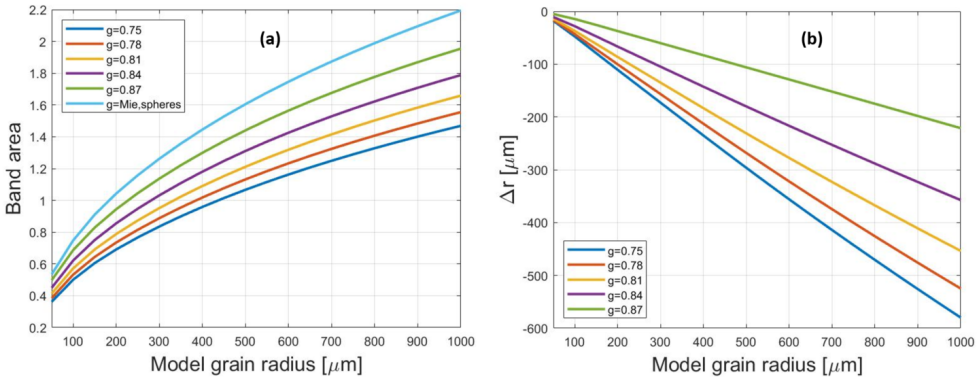

Figure 3.5: Same as Figure 3.4, but for changes in scattering asymmetry parameter. Estimated biases are relative to g derived from Mie calculations of spheres using *Warren and Brandt* (2008) ice refractive indices ("Mie, spheres" in left figure).

and when particles are assumed in the creation of the calibration function. Differences in band area are non-negligible between spherical and hexagonal ($g = 0.75$) particles. The band area decreases notably between $g = 0.87$ and $g = 0.84$, but lower values of g exhibit lower sensitivity. At 1000 μm, the difference in band area between g for spherical ice particles and $g = 0.87$ is 0.24, compared to a difference of 0.09 between $g = 0.75$ and $g = 0.78$. The biases are large for model grain sizes of 500 μm or higher at all g values, with a maximum bias of 580 μm for $g = 0.75$. However, bias appears to be significant only when model grain size is greater than 200 μm. At smaller grain sizes, retrieval errors are less sensitive to particle asphericity.

When the asymmetry parameter changes value, it affects reflectance in ways similar to solar zenith angle. Spherical particles scatter visible and NIR radiation in the forward direction more strongly than other particle shapes, leading to a lower observed albedo. As with near-nadir illumination angles, the lower albedo is interpreted as a larger grain size by the algorithm. If the true particle shape is sufficiently non-spherical, the albedo will increase in the ice absorption feature and reduce retrieved snow grain size. In nature, freshly fallen snow generally begins as small, non-spherical particles before aggregating into larger spheroids (*Sturm and Benson*, 1997). The

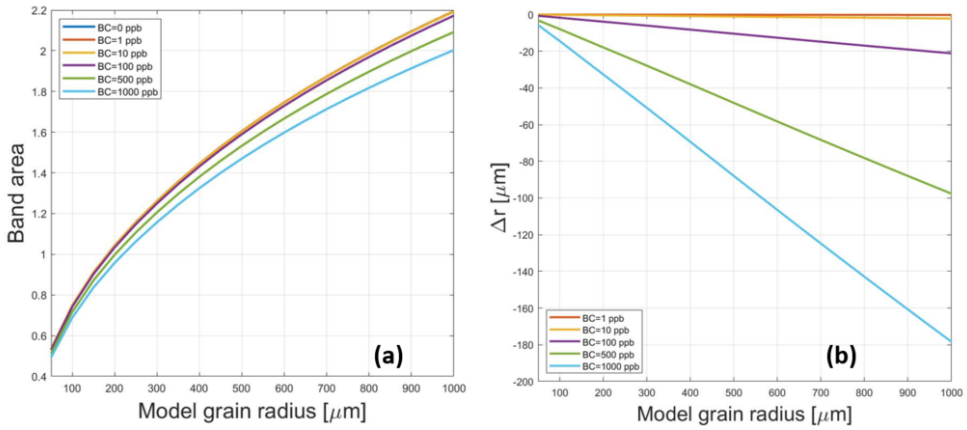

Figure 3.6: Same as Figures 3.4 and 3.5, but for changes in black carbon content. Grain size errors are calculated from calibration curves assuming no impurity content.

spherical particle assumption is therefore most valid for aged snow, whereas a fresh snowpack may be less predictable due to the larger variety in grain shapes.

3.3.3 Black carbon and dust

Relative to a clean snow case, we found that a snowpack requires a high concentration of black carbon to impact the 1.03 μm ice absorption feature. Relative to the baseline with no impurity content, calibration curves with concentrations below 500 ppb show minimal effect on band area or grain size retrievals (Figure 3.6). Band area decreases more efficiently when black carbon exceeds 500 ppb, implying that it begins to supplant ice absorption at these levels. However, this circumstance only occurs for coarse-grained snow. The maximum observed bias is 178 μm at 1000 ppb, but bias decreases to below 100 μm or less for grain sizes smaller than 500 μm.

The three dust species show similar trends in band area and grain size bias for all concentrations and particle size distributions (PSD). The results in Figures 3.7 and 3.8 therefore represent all species, despite slight differences in absorptivity. For all PSD, band area is unperturbed when dust content is 10 ppm or less, and larger PSD show further insensitivity at 100 ppm. The differences become more significant

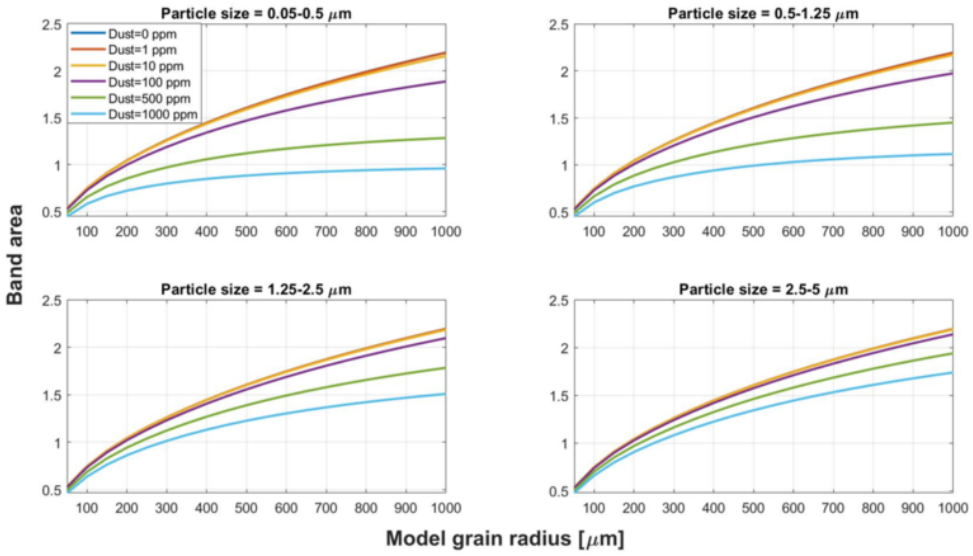

Figure 3.7: Band area sensitivity to modeled snow grain size and San Juan dust content. Sensitivities are given for the four particle size distributions.

at larger concentrations, namely for large snow grain sizes and small PSD. Retrieval biases become substantial in extreme situations, with 1000 pm of dust producing an error of 829 μm for true grain size $r_0 = 1000$ μm and particle radius = 0.05-0.5 μm. When dust content is $\geq$500 ppm, biases are significant ($\Delta r \approx 200$ μm) even at small grain sizes. The bias diminishes with larger particles, though it still exceeds 300 μm when 1000 ppm of dust is present. The decrease in band area with dust also appears to saturate at large concentrations, as the ice absorption feature becomes obscured.

The impact of high dust content on dampening of the absorption feature was recognized by *Skiles et al.* (2017), but it was not quantitatively investigated. Both *Seidel et al.* (2016) and *Skiles and Painter* (2019) also postulated that dust influences snow grain size through enhanced metamorphic processes, an effect verified by *Schneider et al.* (2019) in near-freezing, clear-sky conditions. The results here suggest that dust "masks" the ice absorption feature by reducing albedo at the left shoulder. Dust with small PSD also appears to increase albedo at 1.03 μm, therefore reducing band area further. Although there is uncertainty in the refractive indices of dust and black carbon, particularly in the near-IR, we expect any impurity in sufficient quantity to

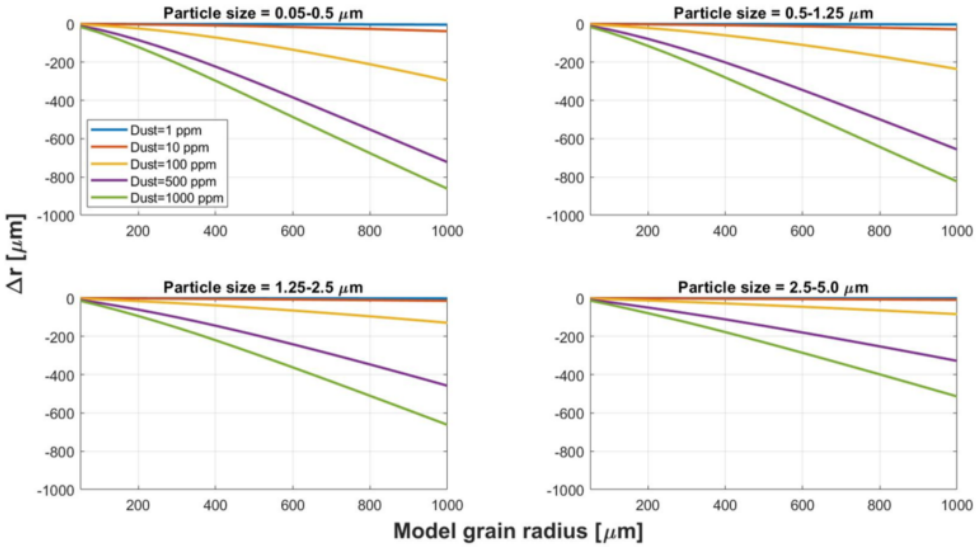

Figure 3.8: Grain size retrieval biases for San Juan dust of four size distributions. Biases are relative to a clean snow case (i.e. Dust=0 ppm).

flatten the 1.03 μm ice absorption feature because this feature is unique to H_2O. The measured band area of a dirty snowpack will be small, leading to a strong negative bias in the retrieved grain size. The impacts are most severe for small particle sizes, which cause greater extinction per unit mass of impurity than larger particles. In worst case scenarios (e.g., Figure 3.8a), a retrieval performed over a snowpack with $r_0 = 1000$ μm would return a grain size of less than 200 μm. Prior knowledge of snowpack impurity content is therefore essential to avoid biases when measuring dirty, coarse-grained snow.

On a per-mass basis, black carbon exhibits a stronger influence on NIR reflectance than dust. A snowpack with 1 ppm of dust shows no bias in grain size, whereas this concentration of black carbon affects retrievals by 100 μm or more when $r_0 \geq 500$ μm. However, such concentrations of black carbon are uncommon in nature, only occurring near heavy BC sources (*Flanner et al.*, 2007). Natural BC concentrations are typically much less than 100 ppb, which are shown in Figure 3.6 to have minimal impact on grain size retrievals. Episodic dust deposits are more likely to generate significant biases at regional scales, as evidenced by the 8000 ppm of dust observed

by *Skiles and Painter* (2017) in the San Juan Mountains. Although dust deposited on Greenland has the theoretical potential to induce errors, significant dust or black carbon deposits are rare over the ice sheet (*Polashenski et al.*, 2015; *Ward et al.*, 2018), so the risk is reduced relative to mid-latitude locations. However, parts of the Greenland ablation zone are very dark due to algae and other organic matter (*Cook et al.*, 2020), so similar impurity-related biases could exist in these regions.

3.3.4 Anisotropic reflectance

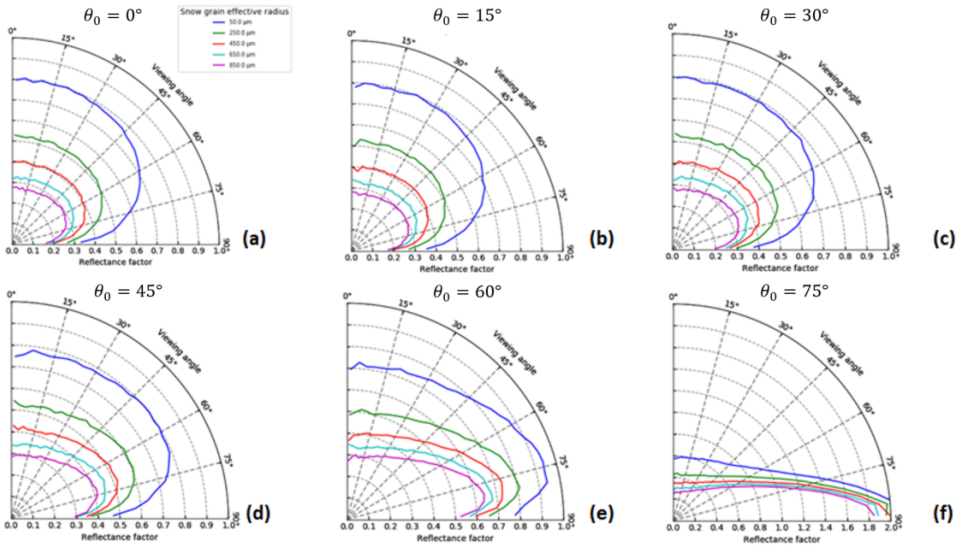

Figure 3.9: Polar plots of azimuthally-averaged bidirectional reflectance factors (BRF) of modeled snowpacks with various snow grain radii, six illumination angles, and $\lambda = 1.035$ μm.

The angular distribution of BRF is shown in Figure 3.9 for six illumination angles at 1.035 μm: 0°, 15°, 30°, 45°, 60°, and 75°. When $\theta_0 \leq 30°$, the BRFs are effectively isotropic for viewing angles up to 45° and small snow grain sizes, and the magnitude of reflectance decreases as θ_v approaches the horizon. The BRF distribution is more uniform at grain sizes of 650 μm and 850 μm, with BRF reductions occurring at $\theta_v \geq 60°$. Anisotropy becomes more pronounced at larger solar zenith angles. Reflectance decreases at near-zenith angles and peaks near the horizon, meaning that forward

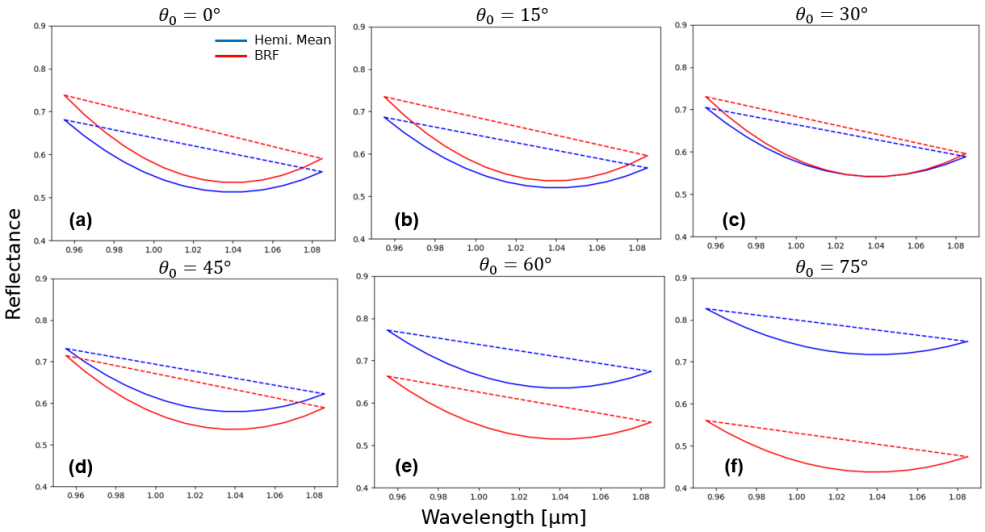

Figure 3.10: Spectral reflectance integrated across a hemisphere ("Hemi. Mean", blue) and for the average BRF received at 0-15° ("BRF", red) for $r_{eff} = 250$ μm at the prescribed illumination angles. The dashed lines represent continuum reflectance for the corresponding spectral curves.

scattering peaks at large angles due to a shallower penetration depth. The BRF is nearly 2.0 when $\theta_0 = 75°$ and $\theta_v \geq 75°$, suggesting that reflectance substantially exceeds that of a white (or lossless) Lambertian reflector at these angles.

Spectral reflectance curves derived from hemispheric reflectance and BRF (Figure 3.10) shapes at the ice absorption feature, despite differences in reflectivity. The BRF exceeds the hemispheric reflectance when illumination angle is near-zenith, as seen in Figures 3.10a and 3.10b, and there is little change in reflectivity between the two angles. At $\theta_0 = 30°$, the reflectance curves are nearly identical, with slight overestimates in the hemispheric albedo at 0.95 μm and underestimates at 1-1.07 μm. The continuum reflectance (the dotted lines in Figure 3.10) of BRF is higher for 0.95-1.07 μm before converging to the hemispheric mean at the right shoulder of the absorption feature.

The BRF decreases significantly at near-nadir viewing angles when anisotropy increases, as suggested by Figures 3.9d-f. The unscaled band area at large illumination angles is similar between reflectance curves (Figure 3.11) despite differences in

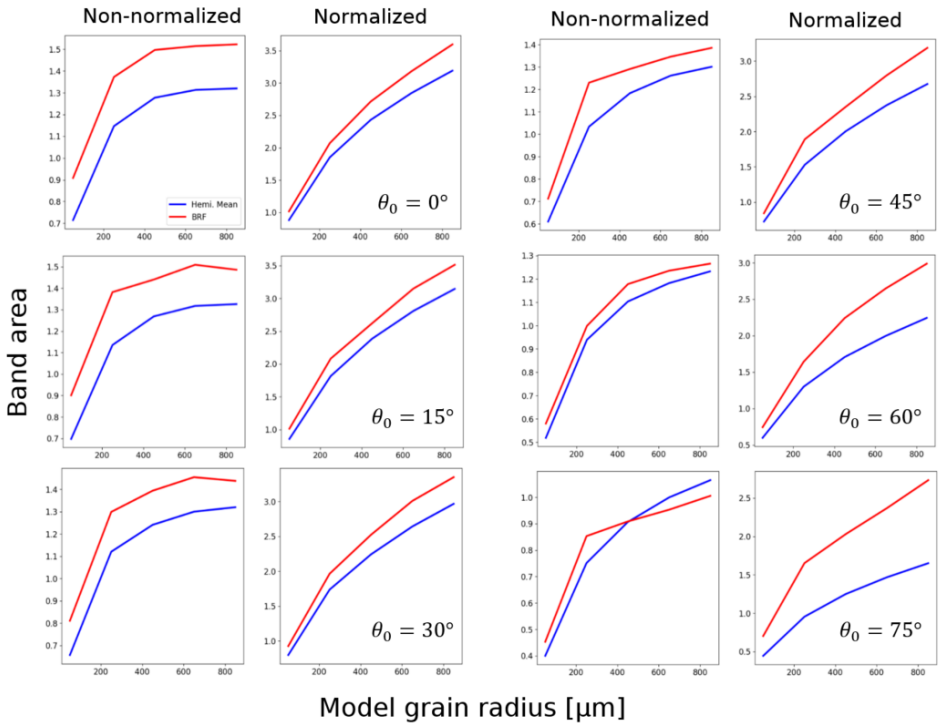

Figure 3.11: Calibration curves for band area vs. model grain radius, derived using hemispheric reflectance (blue) and BRF (red) at six illumination angles. Columns 1 and 3 use band area without continuum scaling (Equation 3.4) whereas Columns 2 and 4 are calculated using Equation 3.1.

θ_0	**Model: Hemi. Mean Retrieval: Hemi. Mean**	**Model: Hemi. Mean Retrieval: BRF**	**Model: BRF Retrieval: BRF**
	Non-normalized		
0°	83.9	791.7	97.2
15°	74.3	641.5	99.6
30°	53.8	485.4	92.7
45°	38.5	266.7	8.8
60°	35.0	126.5	61.2
75°	19.1	101.9	14.1
Mean	50.8	402.3	62.3
	Normalized		
0°	4.6	158.5	2.7
15°	4.8	149.5	9.1
30°	1.6	170.6	6.9
45°	2.2	240.3	11.0
60°	4.0	464.8	7.5
75°	2.8	1053.0	17.0
Mean	3.3	372.8	9.0

Table 3.1: Root mean square errors of retrieved snow grain size using non-normalized band area (top half) and normalized band area (bottom half). In the header, "Model" refers to the reflectance quantity used to generate the lookup table, whereas "Retrieval" is the type of reflectance assumed to be measured.

absolute reflectance. Agreement in $A_{b,u}$ between hemispheric reflectance and BRF decreases as θ_0 decreases, with the most significant differences occurring between 250 μm and 450 μm. However, Figure 3.11 also demonstrates that agreement in $A_{b,s}$ improves when $\theta_0 < 45°$, with RMSE decreasing from 0.79 at 75° to 0.29 at 0°. There is little change in agreement between 0° and 30°, which is expected given the results from Figures 3.9 and 3.10.

The effects of anisotropy on grain size retrievals are given in Table 3.1 for the six illumination angles. The errors shown in Columns 2 and 3 are with calibration curves derived from hemispheric albedo, whereas Column 4 uses a calibration function derived from directional reflectance. The RMSE range for the baseline simulation is 1.6-4.8 μm for scaled band area, implying that uncertainties inherent to the ND2000 method are small. The unscaled band area shows greater uncertainty at all angles

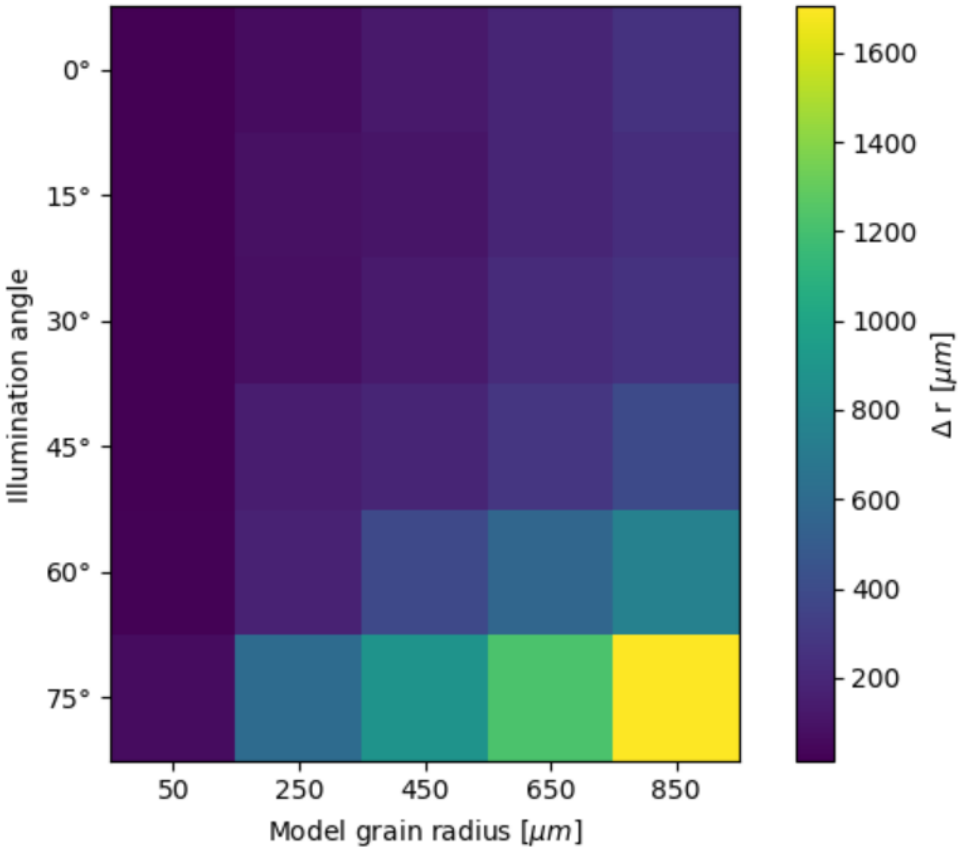

Figure 3.12: Retrieval errors as a function of model grain size and illumination angle, if using normalized band area. The errors assume that the inputs for the calibration curve and the retrieval are hemispheric reflectance and BRF, respectively.

but is smallest when θ_0 is large. When the modeled retrieval implements BRF (Table 3.1, Column 3), RMSE in grain size remains within 200 μm when reflectance is nearly isotropic. The errors increase exponentially as anisotropy becomes more significant, with Δr exceeding 1000 μm at illumination angle 75° for grain sizes $\geq$650 μm (Figure 3.12). When the calibration curve was derived using BRF, errors dropped significantly across all illumination angles. Figure 3.13 shows that the maximum RMSE among the corrected retrievals is 17 μm at 75°, corresponding with a maximum Δr of 23.2 μm at input grain size 250 μm.

The sensitivity of band area to anisotropic reflectance depends on the usage of continuum scaling. Band area without scaling performs best at high solar zenith

angles, where retrieval errors resulting from the Lambertian assumption remain low even when no correction is applied. Reflectance spectra exhibit fewer differences in curve shape, thereby reducing retrieval errors. In contrast, reflectance at smaller illumination (zenith) angles is nearly isotropic. The hemispheric reflectance and BRF generally agree to within 0.02, but because $A_{b,u}$ is small, it is highly sensitive to differences in BRF and consequently produces significant grain size errors even when the correct retrieval scheme is used. When band area is scaled, grain size retrievals become more accurate at lower illumination angles. Although small differences exist between hemispheric reflectance and BRF, $A_{b,s}$ is larger in magnitude than $A_{b.u}$, so it is relatively insensitive to noise in isotropic profiles. Scattered radiation tends more strongly to the horizon as illumination angle increases, leading to the large differences seen in Figure 3.11.

For both $A_{b,u}$ and $A_{b,s}$, there is a dependence on illumination angle and model grain size. As r_0 increases, the potential bias in a retrieval also increases. Figure 3.12 shows that errors originating from the Lambertian reflectance assumption at illumination angle 0° start at 14.3 μm before gradually increasing to a peak of 260.5 μm at large grain sizes. Errors remain within 75 μm when $r_0 = 50$ μm at all illumination angles, but increase exponentially with grain size and solar zenith angle. The increase in error is greatest when solar zenith angle increases from 60° to 75°, indicating a significant change in the directionality of reflectance. Biases also increase significantly between grain sizes at θ_0 =75°. When directional reflectance is used to generate the calibration curve, biases are reduced drastically (Figure 3.13).

We attribute the significant errors in $A_{b,s}$ at θ_0 =75° to changes in continuum reflectance. Figures 3.10f and 3.11f indicate that differences in unscaled band area between hemispheric reflectance and BRF are small at large illumination angles. The lack of disparity in $A_{b,u}$ implies that spectral band depth is nearly equal for hemispheric reflectance and BRF, so it can be concluded that anisotropy is not significantly

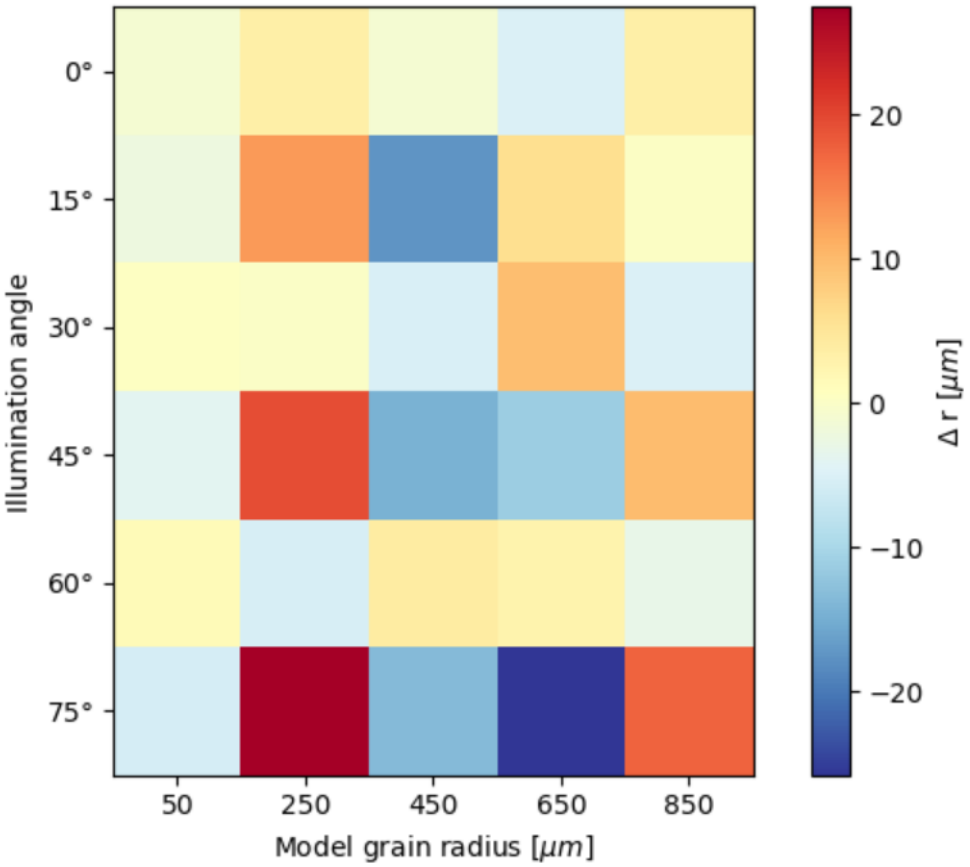

Figure 3.13: Same as Figure 12 but instead using BRF as input for both the calibration curve and the retrieval.

impacting the 1.03 μm ice absorption feature. Instead, a notable decrease in continuum reflectance is observed for BRF at large illumination angles, so $A_{b,s}$ will appear much larger than that of hemispheric reflectance, despite similarities in band depth.

3.4 Conclusions

We examined the potential sensitivity of snow grain retrievals that exploit the 1.03 μm ice absorption feature to assumptions about solar illumination angle, snowpack properties, and anisotropic reflectance. Simulations with the SNICAR model showed that retrieval biases are normally small, but incorrect handling of illumination angle and uncertainty in ice particle shape may lead to significant errors when the true grain size is large. Black carbon has relatively minor impacts even at large concentrations, despite its large influence on visible reflectance. Dust can produce large biases when present in high concentration, so estimations of snow dust content may be needed when attempting to retrieve snow grain size, especially in regions affected by large episodic deposition events.

We also assessed the utility of directional reflectance into the retrieval lookup tables. Our results indicate that hemispheric mean reflectance is an acceptable input into ND2000 at small snow grain sizes and near-zenith illumination angles, where reflected radiation is nearly isotropic. However, errors become significant at large illumination angles even for smaller grain sizes. Our Monte Carlo simulations suggest that band depth is similar between hemispheric reflectance and BRF when anisotropy is significant, but differences in continuum reflectance lead to anomalously large normalized band area for BRF. The retrieval errors decrease substantially when directional reflectance is used to generate the lookup table, so it is imperative for future snow grain size retrieval efforts to consider viewing angle, solar geometry, and local topography.

The results presented here only apply simulated reflectances to evaluate retrieval

biases and carry the benefit of having exact knowledge of the "true" grain size. Future studies, however, should explore such retrieval biases with observed hyperspectral data and coincidental in-situ measurements. We do not anticipate significant errors for airborne and field retrievals in mid-latitude clean snow, for these collections occur during the day with nadir-viewing sensors. However, we expect that anisotropic reflectance would contribute more significant errors to grain size retrievals over Greenland, where solar zenith angle is high. Future hyperspectral satellite missions, such as Surface, Biology and Geology (SGB) and the Copernicus Hyperspectral Imaging Mission for the Environment (CHIME), may perform acquisitions at different times of day, so anisotropic reflectance will also be a factor in spaceborne retrievals. We considered each snow perturbation separately, so possible relationships and co-dependencies between variables could be assessed in future studies. This is especially true for anisotropic reflectance, where the presence of dust or aspherical particles may further exacerbate retrieval errors.

CHAPTER IV

Lidar Volumetric Scattering

4.1 Introduction

The Ice, Clouds, and Land Elevation Satellite-2 (ICESat-2) was launched in September 2018 to perform altimetry measurements of surface height over glaciers and ice sheets (*Neumann et al.*, 2019b). Since then, ICESat-2 data products have been developed to estimate land ice height, vegetation canopy height, and sea ice freeboard (*Smith et al.*, 2019; *Kwok et al.*, 2019; *Neuenschwander and Pitts*, 2019). The sole onboard instrument, the Advanced Topographic Laser Altimeter System (ATLAS), operates at 532 nm to minimize attenuation by clouds and liquid water. The reduced water attenuation allows for further applications of shallow water bathymetry over coastal regions and supraglacial lakes (*Parrish et al.*, 2019; *Fair et al.*, 2020; *Fricker et al.*, 2021). These applications are facilitated by a high spatial resolution (17.4 m footprint diameter and a 10 kHz pulse repetition frequency) and a mandated accuracy of 0.4 cm yr^{-1} for ice sheet elevation change (*Markus et al.*, 2017).

Ice and snow absorb weakly in the visible spectrum compared to the near-infrared (*Warren and Wiscombe*, 1980), so a laser shot from ICESat-2 may experience multiple scattering events within a snow layer before returning to the detector (*Perovich*, 2007). The issue is greatest in clean, coarse-grained snow, where the increased path length between scattering events will introduce a significant delay time in the returned laser

pulse (*Beaglehole et al.*, 1998). Over high-latitude ablation zones, snow impurity content is relatively low during the melt season (*Flanner et al.*, 2007), reducing the absorption potential within snow and raising further concern for altimetry biases.

Previous studies have assessed the potential impacts of snow on ICESat-2 measurements. *Harding et al.* (2011) found that return waveforms from an airborne 532 nm lidar experienced significant pulse broadening over snow, resulting in range biases on the order of a few centimeters. A modeling study by *Kerekes et al.* (2012) found centimeter-level bias in a 532 nm laser when snow grain size was 500 μm or more, and the amplitude of received waveforms was low relative to fine-grained snow returns. *Smith et al.* (2018) simulated ICESat-2 measurements over a snow-covered surface using a suite of surface height estimation techniques. The authors concluded that elevation biases exceeded 0.45 m for clean, coarse-grained snow if the current ICESat-2 surface height scheme is used, though biases could be mitigated if other techniques were considered.

The above studies were published prior to the launch of ICESat-2, so a quantitative assessment on bias in 532 nm lidar acquisitions is needed. At the time of writing, the ICESat-2 mission has collected over 2 years of altimetry measurements over high-latitude regions, yet there have been no documented efforts to quantify altimetry bias over snow. As part of an extensive validation effort, Operation IceBridge (OIB) launched a series of flight campaigns to Greenland late in the melt season. The flights collected elevation measurements using the Airborne Topographic Mapper (*Brock et al.*, 2002), a lidar that collected surface height data at both 532 nm and 1064 nm during the 2019 flights over Greenland. Near-coincident flights were performed with the Airborne Visible/Infrared Imaging Spectrometer (AVIRIS-NG; *Green et al.*,1998) to retrieve hyperspectral reflectance and snow grain size.

In this study, we use AVIRIS-NG hyperspectral data to attribute biases in ATM altimetry measurements to volumetric scattering in snow. Snow grain sizes derived

from AVIRIS-NG reflectance data serve as input to a Monte Carlo ray tracing model to simulate expected bias over the Greenland ablation zone. In parallel, the traveled distance (e.g., range) of received ATM pulses from the 532 nm laser are compared to those from the 1064 nm laser to estimate observed bias. Waveforms derived from the transmitted and returned laser energy are examined for features unique to coarse-grained snow or rough topography. The findings presented here will serve as a benchmark for an ICESat-2 bias assessment over snow-covered surfaces.

4.2 Data Description

4.2.1 Airborne Topographic Mapper

The Airborne Topographic Mapper (ATM) is an altimetry instrument that has been used for high-latitude elevation measurements since 1993 (*Brock et al.*, 2002; *Krabill et al.*, 2002). In recent years, it has been used to validate ICESat-2 surface height estimates over sea ice and the 88°S transect of Antarctica (*Kwok et al.*, 2020; *Brunt et al.*, 2019b) as part of Operation IceBridge. The instrument suite is composed of two laser altimeters that feature off-nadir scan angles of 15° and 2.5°, which correspond to swath widths of 245 m and 40 m at the typical flight altitude. The 2.5° altimeter, also known as the "narrow swath" track, is a dual-color laser that operates at 532 nm (green) and 1064 nm (NIR) simultaneously. The footprint diameter of the 1064 nm is 0.91 m, or 40% larger than the 532 nm beam (0.64 m).

Here, we used two Level-1B Narrow-Swath data products: the Elevation and Return Strength with Waveforms (ILNSAW1B) and the Near-Infrared Waveforms (ILNIRW1B). Both data products include information about waveforms derived from ATM laser pulses, including the amplitude and pulse width for transmitted and received waveforms. It also contains calibrated aircraft-surface range estimates derived from the waveform parameters. Further information about how ATM ranges are

calculated may be found in Appendix A. The ILNSAW1B data includes a geolocated elevation product derived from digitized waveforms to emulate ICESat-2 data (*Studinger*, 2018). The ILNIRW1B data lacks this product, so comparisons between the two data sets must instead use the waveforms and range estimates. *Brunt et al.* (2019a) found that the 532 nm laser agrees well with ground-based measurements over the 88°S transect of Antarctica, with centimeter-level bias relative to other elevation estimates.

4.2.2 AVIRIS-NG

The AVIRIS-NG instrument is an airborne hyperspectral imager that has been used to retrieve surface radiances since 1986 (*Gao et al.*, 1993; *Green et al.*, 1998). Originally operating at 10 nm spectral resolution, the instrument now observes the Earth's surface at wavelengths between 380 nm and 2510 nm at a spectral resolution of 5 nm. By applying an atmospheric correction and orthocorrection to the radiances, one can derive spectral reflectance of the Earth's surface. Reflectances derived in this manner generally have an accuracy within 2-5% (*Thompson et al.*, 2019). The spectrometer has been used for a suite of applications since its inception, including vegetation mapping, trace gas identification, and snow grain size retrievals (*Kokaly et al.*, 2003; *Thorpe et al.*, 2016; *Nolin and Dozier*, 2000).

We use AVIRIS-NG reflectances in this study to derive snow grain sizes for comparison against the altimetry data. Snow grain size is estimated using an inversion algorithm derived by *Nolin and Dozier* (2000), which relates changes in spectral band depth within the ice absorption feature centered at 1.03 μm to changes in snow grain size. The retrieval algorithm assumes that the snow is composed of spherical ice particles, the impurity content is negigible, and the reflectance has a dependence on illumination and viewing geometry. Snow grain sizes derived in this manner have a mean uncertainty of $\sim$50 μm. Although impurities and anisotropic reflectance may

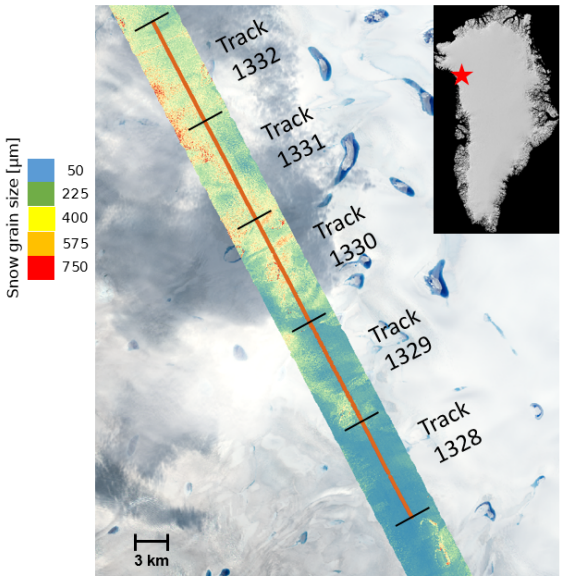

Figure 4.1: Landsat-8 real-color composite of the study location over Greenland on September 6, 2019. The false color swath represents AVIRIS-NG snow grain sizes. The orange line is the ATM flight path over the region, segmented into five data tracks.

bias retrievals without proper consideration (Chapter 3), we assume that impurity content in our region of interest is negligible and that directional reflectance is factored into the retrieval algorithm. We also assume that ice particle shape will have negligible influence on the path lengths traveled by ATM signal photons.

4.3 Methods

4.3.1 Case Study Location

We performed a case study over the northwestern Greenland ablation zone on September 6, 2019. The region is located at coordinates 75.316°-75.438°N, 56.528°-56.778°W, as highlighted in Figure 1. This date and location correspond with a significant overlap between ATM and AVIRIS-NG flights, with ∼100 km of OIB flight data co-registering with AVIRIS-NG surveys. The ice surface features many crevasses and refreezing supraglacial lakes during this time of year, several of which

were observed by ATM and AVIRIS-NG. The lakes are characterized by anomalously high snow grain sizes in the AVIRIS-NG data, whereas the ATM data in both lasers exhibits a higher degree of noise over crevassed ice. These features are small relative to the size of the data swaths, so we applied a moving mean filter with a window size of 500 data samples to mitigate noise in the grain sizes and biases.

4.3.2 Bias Estimation and Attribution

4.3.2.1 Monte Carlo Modeling

We first generated modeled bias estimates using a combination of AVIRIS-NG grain sizes and Monte Carlo modeling. The model fires photons into a simulated semi-infinite snowpack and records their path length until they are absorbed or leave the medium (*Schneider et al.*, 2019). The snowpack is assumed to have spherical ice particles and snow grain size and density prescribed by the user. The model has additional inputs for solar zenith angle, surface roughness, and snowpack impurities, but we assumed (i) the snow surface was smooth, (ii) there were no impurities within the snow, and (iii) the solar zenith angle was equal to the mean solar geometry observed by AVIRIS-NG at the time and location of flight. We used the Monte Carlo model to make accurate estimates of lidar delay time in the snowpack.

We ran a total of 160 Monte Carlo simulations for different permutations of photon wavelength, snow density, and snow grain size. The simulations launched 10^5 photons into a snowpack at wavelengths 532 nm and 1064 nm to simulate the ATM dual-colored lidar pulse interacting with a snow-covered surface. We performed these simulations for snow grain sizes 50-1000 μm at 50 μm intervals, after which we applied a linear interpolation scheme to improve the resolution to 1 μm. This process was executed for snow densities consistent with several stages of snow aging: ρ_s = 100, 200, 300, 400 kg m^{-3}. We obtained the path length traveled by photons that escaped from the top of the snowpack, and for each wavelength the median path length of

escaped photons was calculated to replicate the reference photon technique employed by ICESat-2 (*Neumann et al.*, 2020). The median path length was treated as the surface height offset from an unbiased measurement. If we treat the 532 nm path lengths as biased heights (h_{532}) and the 1064 nm path lengths as idealized height measurements (h_{1064}), then we can derive a modeled bias estimate of path length (Δh):

$$\Delta h = h_{532} - h_{1064} \tag{4.1}$$

In this configuration, a positive Δh implies that 532 nm photons traveled a greater median path length in the snowpack, which would suggest a negative bias in a surface height estimate. Conversely, the 1064 nm path length (surface height) will be biased high (low) if there is a negative Δh. We then placed the biases into lookup tables, depending on the density quantity used in the simulation. The result was four lookup tables that each had 1000 bias estimates as a function of grain size. We consider these lookup tables to be the biases that should be observed in ATM acquisitions over idealized snowpacks, or the "expected bias".

4.3.2.2 Observed Bias

We look for bias in the ATM data by comparing calibrated range estimates between the two beams. In short, these ranges are derived using the centroid of digitized waveforms from the transmitted and received signals. A more detailed description of ATM waveforms and how they are used to derive range and surface height may be found in Appendix A. The beams occasionally did not record laser pulses, so we applied a co-registration algorithm to match data samples from both beams. Because both beams fire simultaneously, the algorithm co-registers shots between beams using the time stamps recorded for each laser pulse. We speculate that crevasses and melt ponds may impact the signals, for we found that signal loss was greater in flight

tracks where rougher terrain is present. We recorded a maximum signal loss of 21% in Track 1331, with a ∼17% signal loss in Tracks 1330 and 1332. In Tracks 1328-1329, signal loss was lower at 4%. Calibrated ranges from the co-located lasers were used to approximate observed bias using Equation 1. We also refer to this quantity as the "actual bias". Because ATM computes range and elevation using digitized waveforms, we examined received waveforms to find differences in maximum amplitude and pulse width over regions of large snow grain size.

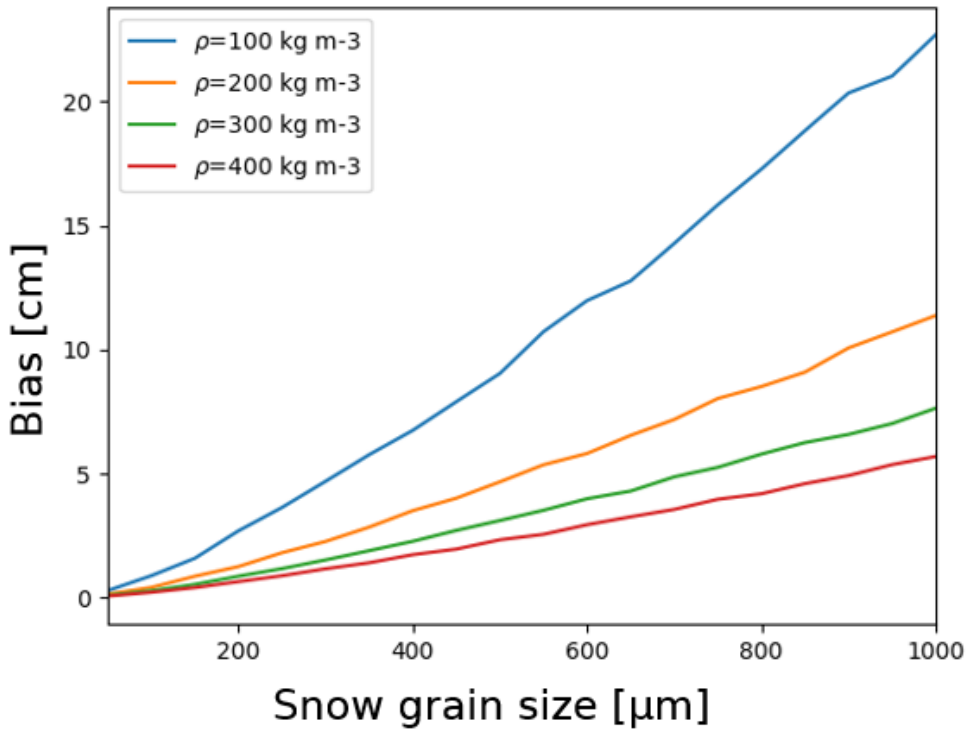

Figure 4.2: Modeled ("expected") laser bias derived using median path length estimates as a function of snow grain size and snowpack density. Positive values indicate greater penetration bias in a 532 nm laser.

To attribute altimetry bias to snow grain size, we needed to co-register ATM lidar pulses with AVIRIS-NG grain size estimates. We extracted geographical information from AVIRIS-NG files using ENVI, after which we matched ATM beam data with the spectrometer pixel-by-pixel. We then mapped each pixel with an estimate for expected bias by matching observed grain sizes with the closest values found in each

lookup table. In other words, each AVIRIS-NG pixel co-registered with ATM had four modeled bias estimates that corresponded with the different assumed snow densities. The pixels were large relative to the shot rate of ATM, with each pixel containing up to 200 ATM shots. We therefore took the average observed bias in each pixel to avoid redundancy with modeled estimates. We note that ATM measurement variability within an AVIRIS-NG pixel may be useful to analyze the effects of topography on altimetry bias, but we leave this topic open for a future study.

The observed biases were compared to co-registered model biases at the four snow densities. If the actual bias agreed with one of the modeled estimates, then we could conclude that (i) the lidar biases are linked to the optical grain size of snow and (ii) the bias is consistent with one of the given snow densities. If the two bias quantities disagreed, then we examined the elevation and waveform data for other potential sources of bias.

4.4 Results

Model-derived estimates of laser bias have a strong dependence on snow grain size and density, as seen in Figure 4.2. At smaller grain sizes, bias has a smaller dependence on the snow density unless $\rho_s = 100$ kg m^{-3}. Biases show little sensitivity to density changes at $\rho_s \geq 200$ kg m $^{-3}$ when snow grain size is 400 μm or less. Larger grain sizes exhibit greater dependence on snow density, especially between 100 and 200 kg m^{-3}. The largest biases occur for $\rho_s = 100$ kg m^{-3}, up to a maximum of 23 cm for $r_{eff} = 1000$ μm. The bias asymptotically approaches zero for all snow densities at very small grain sizes, implying that little laser bias should be expected in fine-grained snow or over a bare surface.

The AVIRIS-NG snow grain sizes co-registered with ATM are shown in Figure 4.3. The southern regions of the flight track are characterized by grain sizes of $\leq$150 μm that gradually increase near crevassed terrain. Grain size increases in the northern

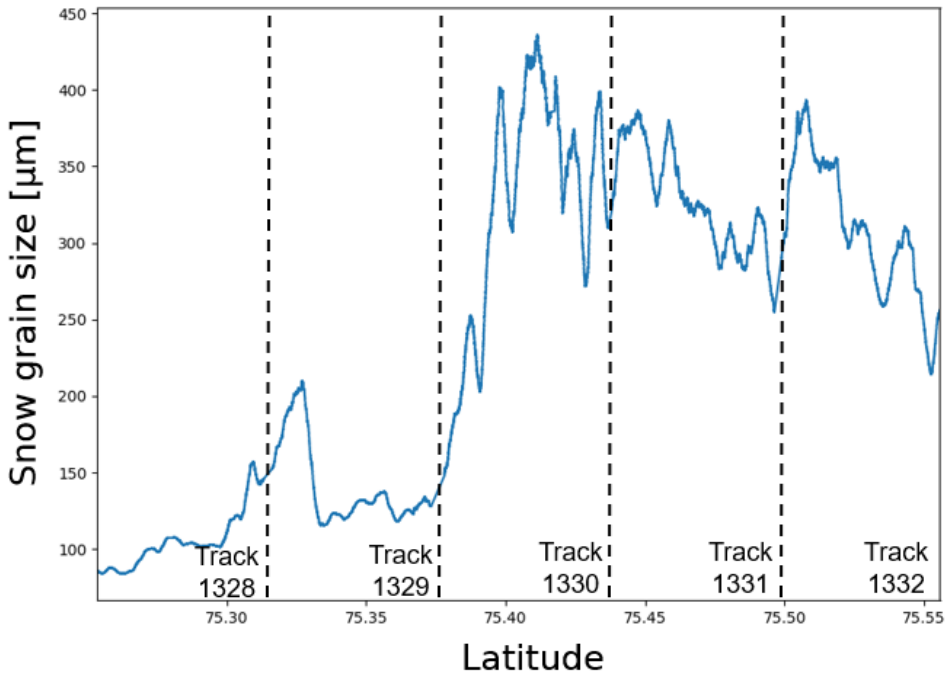

Figure 4.3: Snow grain sizes for AVIRIS-NG pixels co-registered with ATM footprints. A moving mean filter was applied to mitigate noise. The dotted lines indicate boundaries between flight tracks.

reaches of the region to 300-400 μm on average. This increase corresponds with a gradual decrease in surface elevation (Figure 4.4), implying a possible relationship between snow grain size and surface height. The northern tracks (e.g., ATM Tracks 1331 and 1332) exhibit sub-surface scattering several meters deep, indicating the presence of heavy crevassing. As seen in Figure 4.1, a few instances where grain size exceeds 700 μm appear most frequently near crevasses and melt ponds, where low NIR reflectance may impact grain size estimates. Figure 4.1 also reveals significant interpixel variability in grain size, suggesting that surface topography and variable snow aging are significant factors at the pixel scale.

The co-registered snow grain sizes were then used to model altimetry bias of the study region. We selected bias estimates at ρ_s = 200 kg m^{-3} as a baseline for comparison against the observations, given that snowpacks at this density are somewhat aged or wet. Figure 4.5 shows that the small grain sizes in Tracks 1328 and 1329

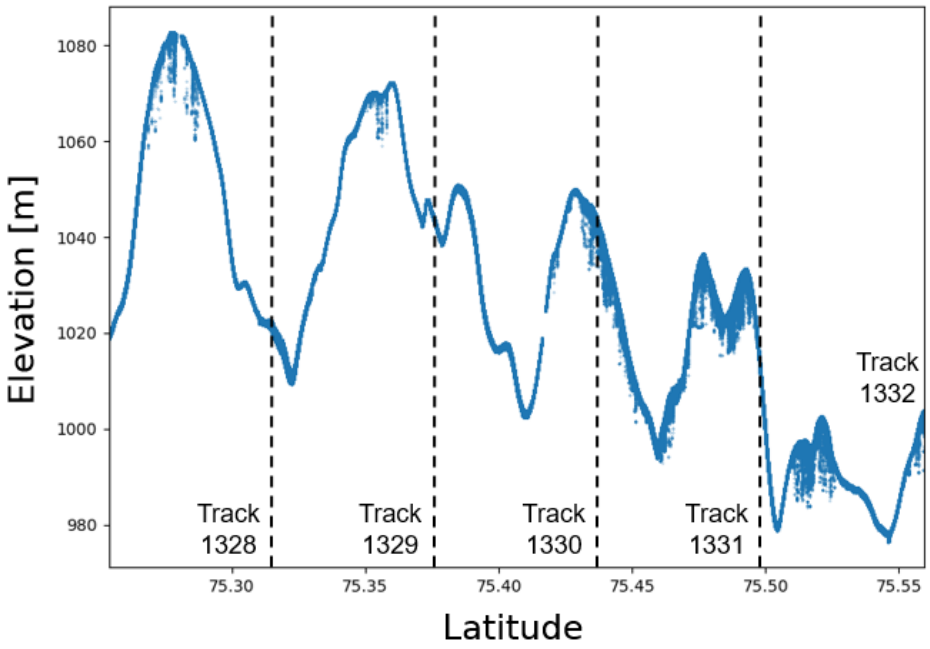

Figure 4.4: Two-dimensional elevation measurements obtained from the 532 nm ATM laser. The surface heights were derived from received waveforms and geolocated to imitate ICESat-2 measurements.

correspond with negligible model bias and low uncertainty. In regions with larger grain sizes, the bias increases to 2.5-4 cm, though the uncertainty due to snow density also increases. The observed bias in the 532 nm ATM beam generally agrees with modeled estimates. The trend in ATM bias closely follows that of the modeled estimates in Tracks 1330-1332, particularly when snow grain size is at least 200 μm. There are small underestimates relative to the model at 200 kg m^{-3}, but the actual bias generally shows consistency with expected bias at snow densities of 200-300 kg m^{-3}. The mean bias observed over Tracks 1330-1332 is 2.14 cm, with variable snow densities causing a potential mean uncertainty of $\pm$1.96 cm.

The agreement between observed and modeled bias weakens at small grain sizes (i.e., $r_{eff} \leq 150$ μm). In ATM tracks 1328 and 1329, there is a notable discrepancy between the model and observations, regardless of snow density. The observed bias appears to follow patterns in the grain size trend, but it becomes negative when grain

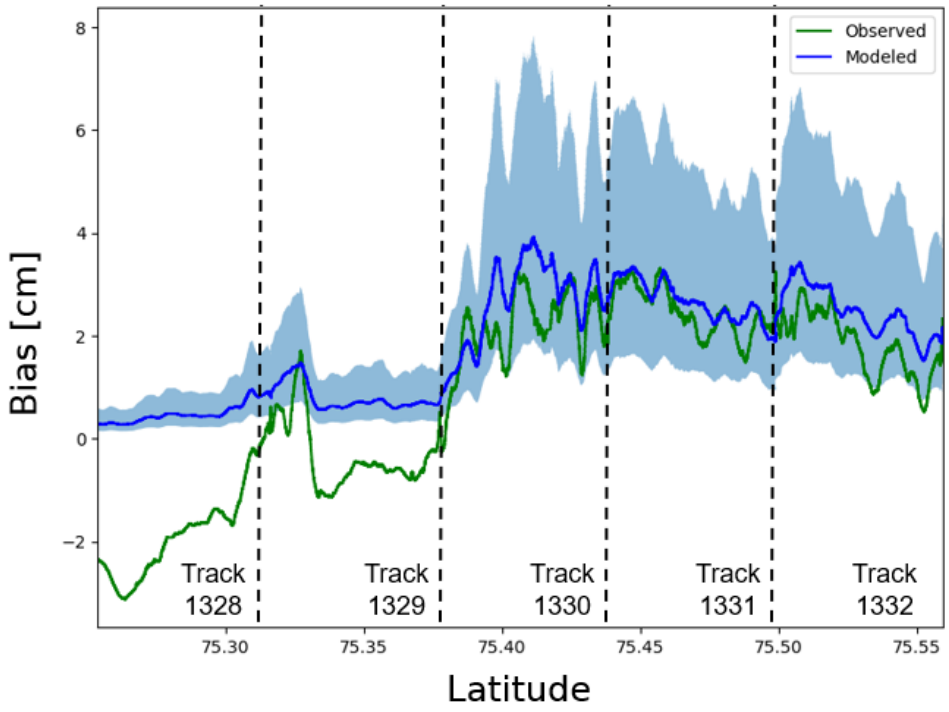

Figure 4.5: Along-track ATM (observed, green) and modeled (blue) bias estimates. AVIRIS-NG snow grain sizes were compared to the lookup table for ρ_s = 200 kg m^{-3} to derive modeled bias. The uncertainty shading represents the modeled bias for ρ_s = 400 kg m^{-3} (lower bound) and ρ_s = 100 kg m^{-3} (upper bound).

size is 150 μm or lower, implying that the NIR beam is biased relative to the green beam. We should expect negligible bias in the NIR beam over any snow surface, so an instrument calibration issue may be present in the data (see Section 4.5.2 for more details). The difference is most notable in Track 1328, where snow grain size is below 100 μm and laser bias approaches -3 cm. As seen in Figure 4.5, the modeled bias decreases to zero over this region. The mean observed bias in Track 1328 is -1.74 cm, compared to a mean modeled bias of 0.5±0.38 cm, and the average observed and modeled bias across Tracks 1328-1329 is -1.07 cm and 0.64±0.48 cm, respectively. Despite these differences, the observed bias follows trends in the snow grain size in all flight tracks.

Generally, the amplitudes should scale with surface reflectance, so regions of

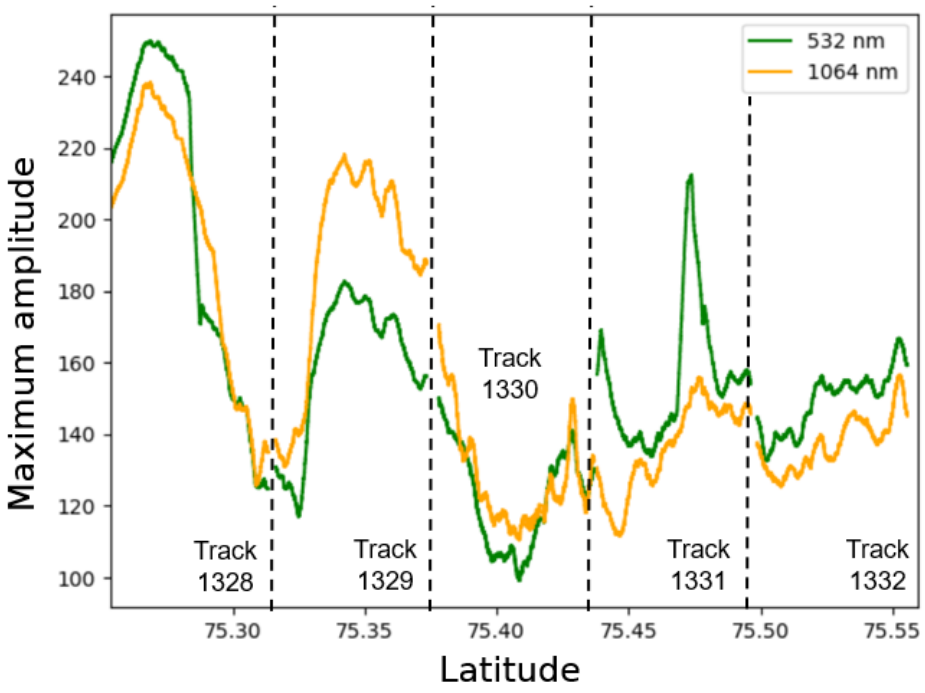

Figure 4.6: The maximum amplitude of received waveforms from the ATM beams across the study region. The amplitudes represent signal strength relative to a peak value of 255.

smaller grain size will have higher waveform amplitudes, particularly in the NIR signal. As Figure 4.6 shows, the maximum received amplitudes appear to inversely relate to snow grain size, given that the amplitudes in Tracks 1330-1332 are generally lower than those observed in Tracks 1328-1329. The amplitudes in both ATM beams peak in Track 1328 near the region of small grain size and negative bias. The 532 nm amplitudes are larger than those of the 1064 nm beam in this region. The beginning of Track 1329 exhibits a strong decrease in the amplitudes that corresponds with an increase in snow grain size. The decrease is followed by an increase that introduces a notable disparity between beam amplitudes and occurs with a negative observed bias. The beam amplitudes show better agreement in Tracks 1330-1332, with the green amplitudes slightly higher on average. It is unclear what produces the distinct local maxima in the Track 1331 green waveforms, but we theorize that small melt ponds or ice may be inducing specular reflection and increasing reflected laser energy.

The pulse width is defined as the maximum width, in number of digitizer samples, of a waveform above a prescribed noise threshold (Appendix A). The width of a received waveform may be broadened in a medium that produces volumetric scattering, such as over coarse snow or crevasses. Received waveform widths show similar patterns to the amplitudes, as seen in Figure 4.7. The width of waveforms is positively correlated with snow grain size and bias in Track 1328, with both the green and NIR beams experiencing pulse broadening. The other tracks are less conclusive, but we observe an overall increase in pulse width that matches with changes in grain size. The green waveforms feature localized pulse broadening in Tracks 1329 and 1331, and Figure 4.4 shows that these regions have crevassed terrain that may produce volumetric scattering in the received waveforms. Otherwise, the green waveforms are less sensitive to changes in terrain than the NIR waveforms, which show significant small-scale variability in Tracks 1330-1332.

4.5 Discussion

4.5.1 532 nm Ranges and Waveforms

The relationship between snow grain size and altimetry bias is correlated with the path length of signal photons incident upon a snow surface. When a lidar signal interacts with snow, there are three potential outcomes. The first outcome is that the signal is reflected from the surface with minimal subsurface scattering. This case is most common for fine-grained snow, where ice particles are numerous enough to efficiently scatter the signal away from the surface. In cases of near-surface reflection, the altimetry bias is near-zero, as seen in the modeled results over Tracks 1328 and 1329. Received near-infrared signals are also generally reflected near to the surface, as NIR photons that penetrate into a snowpack have a high probability of absorption.

In the second outcome, signal photons reflect from a snow surface after experi-

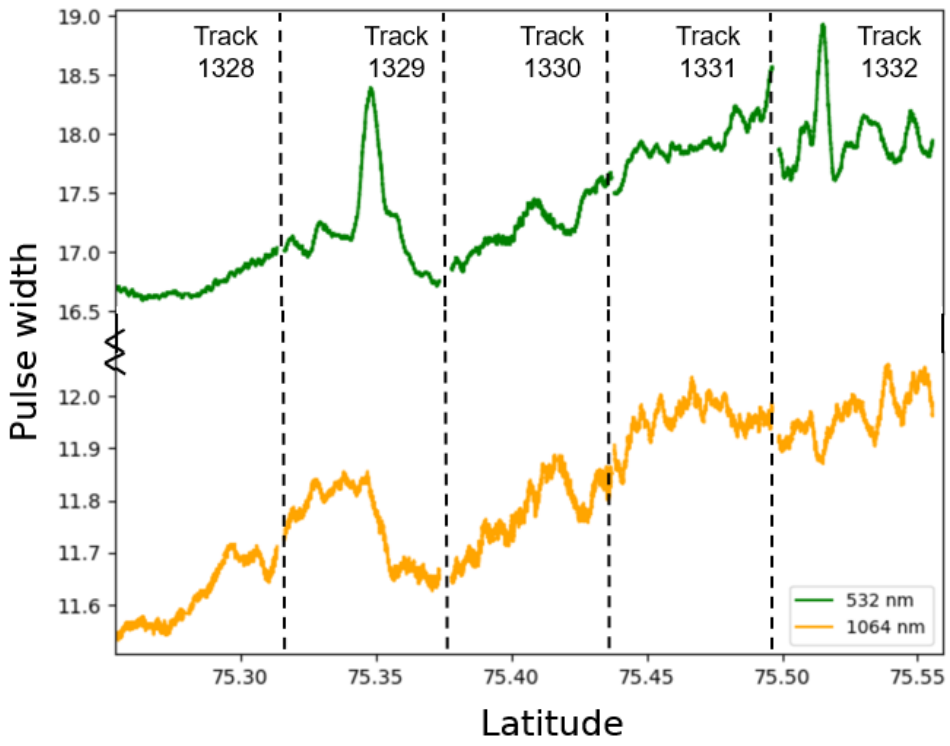

Figure 4.7: The width of received waveforms from the ATM beams. Waveform pulse width is taken as the number of digitized samples above the noise threshold.

encing multiple scattering events within the snowpack. The optical grain size of the snowpack is inversely related to its specific surface area, which determines the spacing between individual ice particles. As specific surface area (grain size) decreases (increases), the average distance traveled between refraction events increases, therefore also increasing the path length and delay time experienced by a lidar signal. The wavelength of the lidar signal influences the number of scattering events likely to occur, with a 532 nm beam expected to scatter multiple times within a snowpack before reflection or absorption. A 1064 nm beam is more likely to experience the third outcome in coarse-grained snow, where the signal is lost due to absorption. We observe this pattern in both the models and observations in Tracks 1330-1332, given the consistently positive bias over the region.

A bias in the ATM ranges implies that there is a change in the amplitude and width

of green waveforms. As shown by *Smith et al.* (2018), volumetric scattering by coarse snow grains should lower the amplitude and increase the tails (e.g., pulse width) of received waveforms. Our results indicate that snow grain size impacts the waveform amplitude to an extent, but the pulse widths are less conclusive. We attribute the lack of definitive change in ATM waveform width to the waveform tracking strategy utilized by the lidar to estimate range. ATM uses a Gaussian-threshold model to filter background noise and estimate range (Appendix A), and this approach ignores the tails of waveforms unless the maximum amplitude is low or the pulse width is large. Although we observe changes in amplitude that show consistency with grain size trends, an increase in the waveform tail will only impact the pulse width parameter for snow grain sizes exceeding $\sim$750 μm unless the snow is highly porous. Snow grain sizes of this magnitude were rare over the study location, but we expect more noticeable changes in received waveform shape where coarse-grained snow is located, such as melting snow over mid-latitude mountain ranges.

4.5.2 1064 nm Range Bias

The NIR beam appears to have an inherent bias relative to the green beam that is not calibrated and is dependent on surface type. To examine the potential errors between the two beams over different surface media, we performed a brief case study in northern Greenland on September 4, 2019 (ATM Track 1740; 76.6292-76.7005°N, 69.0253-69.0801°W). The surface is characterized as mostly deep water with a small region of dark land at the start of the flight track (Figure 4.8). Although we should expect negligible bias between the two beams over both surface types, Figure 4.8 demonstrates that NIR ranges were 3 cm larger than green ranges even over open water. This observation implies that the NIR beam penetrates water surfaces deeper than the green beam, despite the high absorptivity of near-infrared light by water. Additional case studies were performed over different surface types (not shown), but

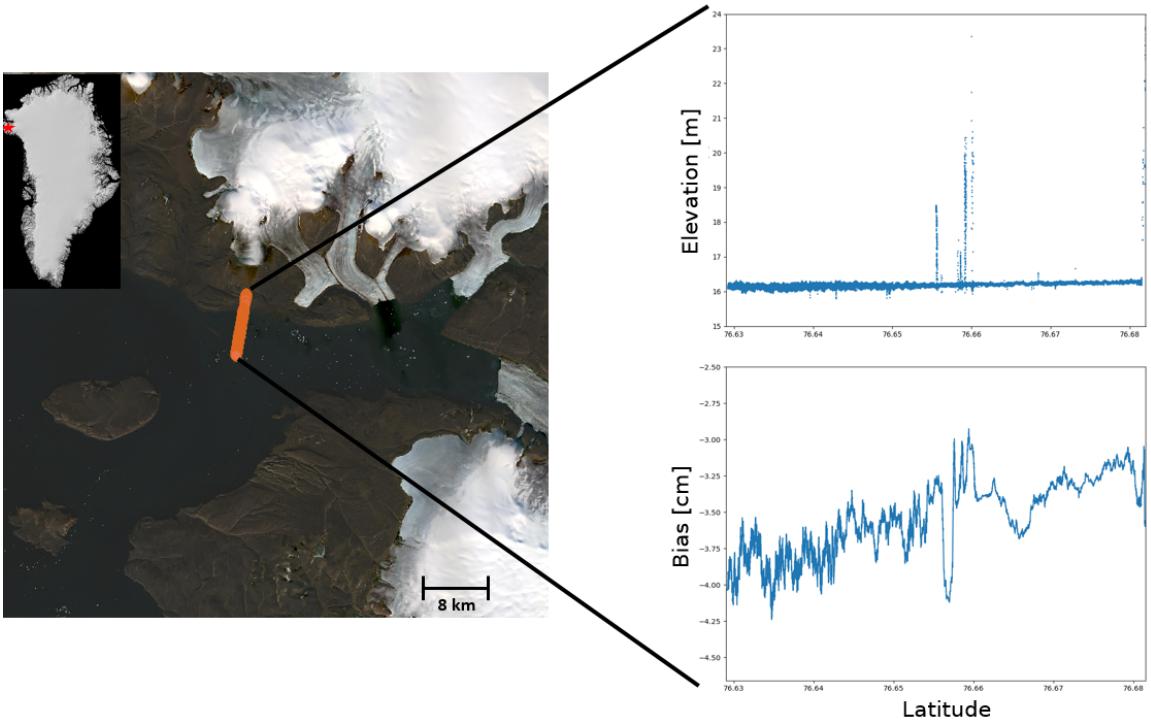

Figure 4.8: (left) Landsat-8 image (September 4, 2019) of the secondary case study location in Northern Greenland. The orange line indicates ATM flight track 1740. (top right) 2-D elevation profile over the region of interest. (bottom right) ATM laser bias over the flight track, where negative values indicate bias in the NIR beam.

the biases were more variable, suggesting that the range bias is dependent on surface media.

There have been no documented efforts prior to this study that perform an accuracy assessment between the two ATM beams. The exact cause for the NIR biases over fine-grained snow is unknown, but we speculate that it partly originates from the design of the ATM instrument suite. The two beams are transmitted simultaneously, but the near-infrared beam has two important differences. First, the temporal response of the NIR detector is slower than the green detector, and this slowed response produces a delay time of ∼60 ns between recorded transmitted pulses (*Manizade*, 2020). Such a delay time would result in 9-10 m of altimetry bias, which is not observed in the case studies considered here. The delay time is likely corrected in

post-processing, though uncertainties may persist due to systematic errors (*Martin et al.*, 2012).

The NIR beam also features a footprint diameter of 0.91 m on the surface, compared to the 0.64 m footprint of the green beam. The NIR beam therefore has twice more surface areal coverage per laser pulse than the green beam. The larger footprint allows for slightly greater areal coverage per pulse, but it also decreases the photon density of received signals, therefore also decreasing the signal-to-noise ratio. In theory, the corresponding waveforms would have a lower maximum amplitude and a larger pulse width relative to smaller-footprint lidars (*Gatziolis and Andersen*, 2008), but we observed greater pulse widths in the green beam. The NIR waveform amplitudes are generally lower and more variable than those of the green waveforms, so the bias may also be a consequence of NIR waveform sensitivity to surface media.

The NIR range bias has two important implications for the results presented here. First, if the NIR bias is observed across all snow surfaces, then snow grain sizes of 100-150 μm will mitigate bias in the NIR beam. In other terms, a snowpack shortly after snowfall will reflect ATM laser pulses at nearly equal intensity, independent of wavelength or laser footprint. Conversely, an inherent negative bias suggests that the observed biases in Figure 4.5 are $\leq$3 cm too small in coarse-grained snowpacks. We do not anticipate a uniform 3 cm bias throughout the study location, though a calibration of 1.5-3 cm in regions of small grain size would improve agreement with the models. Additional research is needed to separate intrinsic ATM laser bias from bias induced by coarse snow grains, but we speculate that a correction would produce consistency between observations and models at snow densities 150-200 kg m^{-3}.

4.5.3 Uncertainties in Grain Size and Signal Range

The conclusions by *Smith et al.* (2018) imply that bias could be significant in clean, coarse-grained snow, though the severity of the errors depends on the lidar

waveform processing approach used to estimate elevation. The ATM instrument uses the centroid of each received waveform, for which *Smith et al.* (2018) found a maximum bias of ∼14 cm, or 2-4 cm for the grain sizes generally found over our study location. However, the modeling results by *Smith et al.* (2018) only consider a constant snow density of 400 kg m^{-3}. The trends in Figure 4.5 demonstrate that snow density has a strong impact on potential altimetry bias. The spread in bias is low at small grain sizes, for the altimetry signal is more likely to be scattered away from the snow surface. For larger snow grain sizes, the density of a snowpack determines the spacing between ice particles, so it is an important control on the path lengths experienced by signal photons. Thus, the bias observed at large snow grain sizes is highly sensitive to snow density.

Both snow density and grain size tend to increase as the snow ages, so we anticipate that aged snow will exhibit altimetry biases comparable to modeled results at $\rho_s =$ 200-300 kg m^{-3}. The results in Figure 4.5 generally agree with this assessment. It is more difficult to infer snow density when the snow grain size is small, for the observed bias becomes smaller than modeled estimates at all snow densities.

Although there is a clear relationship between snow grain size and ATM bias, we recognize that local topography and snow impurity content are important drivers of uncertainty. For example, the study region features many crevasses and melt ponds, both of which are darker than the surrounding ice. The snow grain size retrieval algorithm implemented by AVIRIS-NG does not mask or correct for naturally dark surfaces, so grain sizes near crevasses and melt ponds will appear larger and skew modeled bias estimates. Similarly, the retrieval algorithm does not account for dust or black carbon in the snow, and a significant quantity of either impurity would reduce the retrieved grain size (Chapter 3). Black carbon in sufficient concentrations also absorbs a 532 nm lidar signal more efficiently than clean snow, so contaminated snow will have lower observed bias (*Smith et al.*, 2018).

Crevasses are significant volumetric scatterers for the lidar wavelengths considered in this study. Figure 4.4 demonstrates that the study region is highly rugged with many crevasses, particularly in Tracks 1331 and 1332. Volumetric scattering from crevasses produces significant bias in observed ranges, and both beams may be scattered by the walls of a crevasse. Because the effects of crevasses on altimetry signals are less predictable than the effects of snow, further research is needed to discriminate between these surface features.

4.5.4 Implications for ICESat-2

Based on the results in Figure 4.5, we anticipate that ICESat-2 bias over snow-covered regions will be governed by the optical grain size of the snow. Studies by *Brunt et al.* (2019a) and *Brunt et al.* (2019b) demonstrated that ICESat-2 and ATM exhibit comparable biases over ice sheets, so we assume that snow-induced bias signatures will also be similar between the two altimeters. ICESat-2 error trends over the Greenland ablation zone will generally follow that of modeled snowpacks with density $\sim$200 kg m^{-3}, and biases will be 2-4 cm on average. We expect little to no bias when snow grain size is small, e.g. $\leq$150 μm. Although these errors are within the accuracy requirements of the mission (*Neumann et al.*, 2019b), we cannot rule out more significant errors produced by regions of porous, coarse-grained snow, especially during the Northern Hemisphere melting season.

4.6 Conclusions

In this study, we used airborne altimetry data from ATM to quantify volumetric scattering bias in lidar signals. A fusion of airborne snow grain size retrievals and Monte Carlo modeling was used to predict altimetry bias over the western Greenland ablation zone. The green ATM beam was compared to the near-infrared beam to estimate observed bias. Despite an inherent range bias in the NIR beam, our re-

sults demonstrate a positive correlation between the optical grain size of snow and altimetry bias. The modeled bias shows that snowpack density is an important driver for volumetric scattering, but observed biases in the study location generally remain within 10 cm. We expect more significant biases near the peak of the Northern Hemisphere melting season, when snow grain coarsening will enhance volumetric scattering at all snow densities. Additional work is needed to assess ICESat-2 elevation measurements over the study region, for it lacks the thresholding technique implemented by ATM to filter noise.

The results presented here only consider the biases induced by volumetric scattering within a snowpack. Further research is needed to identify changes in altimetry bias due to snow impurities or crevasses. Dust and black carbon are difficult to quantify without in-situ measurements, so there is a need for accurate airborne and satellite retrievals of surface impurity content. Similarly, a correction for volumetric scattering from crevasses is necessary, given that they impact both ATM beams and introduce noise to trends in bias related to grain size. The ATM waveforms and ICESat-2 photon classification scheme may prove useful in identifying and correcting these issues.

CHAPTER V

Conclusions

5.1 Summary of Research Findings

The cryosphere has experienced unprecedented changes in ice mass balance and snow cover in recent decades. Both the Greenland and Antarctic ice sheets have contributed ∼27 mm to global sea level rise since the start of the satellite era, and ice loss is expected to increase in the coming decades (*Shepherd et al.*, 2019; *Rignot et al.*, 2019; *Vaughan et al.*, 2013). Similarly, the seasonality of snow cover is sensitive to current warming trends, with consequences for water resources and ecosystems (*Bales et al.*, 2006; *Penczykowski et al.*, 2017). Although computer modeling is useful to predict long term changes to the cryosphere, there is also a need for observations to constrain the models and to assess the current state of ice and snow. Remote sensing is therefore a powerful tool that allows for measurements of ice and snow at multiple spatial and temporal scales. At the small scale, unmanned vehicles may be used for fine-scale observations that may also support simultaneous in-situ measurements. At larger scales, airborne and spaceborne instrumentation facilitates interseasonal measurements of ice and snow.

A suite of technologies may be used to remotely sense the cryosphere, but here we focus on lidar and hyperspectral imaging. The ICESat-2 and ATM instruments are lidar altimeters with sub-meter level spatial resolution, allowing for precise mea-

surements of ice sheets and sea ice. Both altimeters apply lasers with a 532 nm wavelength, so there is the potential for meltwater bathymetry, as discussed in Chapter 2. Hyperspectral radiative transfer and imaging is demonstrated as a tool for determining the impacts of changes in solar geometry or impurity content over a snowpack (Chapter 3). Together, dual-colored lidar and hyperspectral imaging may be used to attribute altimetry bias to surface composition, such as changes in optical snow grain size over Greenland (Chapter 4).

In Chapter 2, we posed the following science question: *Can lidar altimetry be used to approximate supraglacial lake depth over Antarctica and Greenland?* We used altimetry measurements from ICESat-2 and the Airborne Topographic Mapper to search for lakes over Antarctica and Greenland in their respective melting seasons. An algorithm was developed that detected supraglacial lakes using along-track histograms of surface height. Lake surfaces and beds were then separated into individual data sets through statistical inference, and depth was taken as the difference between the surface and the bed. Through this algorithm, we retrieved the depths of 24 supraglacial lakes, 12 of which were observed by ATM and the remaining 12 seen by ICESat-2. The algorithm profiled supraglacial lakes with reasonable accuracy, with an average uncertainty of 0.11 m for ATM, 0.53 m for ICESat-2 Antarctic lakes, and 0.31 m for ICESat-2 Greenland lakes. Both altimeters were capable of consistently detecting lake bottoms as deep as 7 m. Water bodies deeper than 7 m may be profiled by ICESat-2 (*Parrish et al.*, 2019), but the statistical confidence in received signal photons decreases with depth. The ATM lidar is less effective at detecting lake beds below 7 m, for the return signal is too weak to be recorded by the receiver. We also outlined opportunities to improve supraglacial lake depth retrievals when using altimetry data, including improved automation and the consideration of lake bed impurities and rough topography.

We focused on snow and hyperspectral radiative transfer in Chapter 3. Two-

stream radiative transfer modeling was used to answer the question: *How does the presence of light absorbing impurities, aspherical particles, or anisotropic reflectance impact snow grain size retrievals?* The ice absorption feature at 1.03 μm was exploited to observe changes in snow grain size when solar geometry or snowpack impurity content were perturbed. We used the SNICAR model to generate spectral albedo curves for simulated snowpacks with prescribed impurity contents, scattering asymmetry parameters, and solar zenith angles, from which calibration curves were derived to relate snow grain size to band area within the absorption feature. This same method was applied to a Monte Carlo model to simulate anisotropic reflectance over snow-covered surfaces. Our results indicate that incorrect handling of solar illumination angle generates significant bias in snow grain size retrievals. The bias due to ice particle shape is somewhat mitigated due to larger snow grains becoming spherical as they age, but fresh snow may introduce uncertainty due to the large variety in grain shapes. Black carbon and dust are potentially large contributors to retrieval biases, though the concentrations needed are generally rare in nature. However, episodic dust events may deposit up to 8000 ppm of dust onto a snowpack, so retrieval errors may be significant if the dust content is not properly accounted for. Finally, we found that snowpack reflectance is nearly isotropic at near-zenith illumination angles, but anisotropy becomes significant at larger angles. Grain size retrievals that do not account for anisotropy may observe snow reflectances much lower than expected, thereby introducing substantial errors in snow grain size. Because of these factors, knowledge of snowpack state and solar geometry are vital for snow grain size retrievals.

Our work in Chapter 4 uses the experience and knowledge we gathered from Chapters 2 and 3 to answer the question: *What are the biases we observe in 532 nm airborne altimetry data over Greenland, and how much originates from volumetric scattering by snow?* A fusion of lidar altimetry and hyperspectral imaging was used

to attribute altimetry biases to snow grain size. Snow grain sizes from AVIRIS-NG hyperspectral data served as input to the Monte Carlo model from Chapter 4, and we estimated the median path length traveled by photons at 532 nm and 1064 nm for 1000 snow grain sizes and four snow densities. The path lengths were converted to modeled altimetry bias as a function of snow grain size. The modeled results were compared to biases between the ATM 532 nm and 1064 nm beams over the northwest Greenland ablation zone. Trends in the observed biases were similar to those in AVIRIS-NG snow grain sizes, indicating a possible link between grain size and altimetry bias. When compared to the modeled bias, the observations agreed best for modeled snowpacks with density 200-250 kg m^{-3}, particularly for larger snow grain sizes, and we observed an average altimetry bias of 2.14 cm. We noted disagreement between observations and the model when $r_{eff} \leq 150$ μm, and subsequent analysis revealed a centimeter-level range bias in the ATM NIR beam. Despite this issue, the observations exhibited similar trends to grain size even with small snow grains, so we expect similar trends in snowpacks coarser than those observed in Chapter 4. We also anticipate that ICESat-2 biases will be comparable to those from the green ATM beam over the study region, and we will pursue a follow-up study quantifying these biases.

5.2 Future Research Directions

Our supraglacial lake study in Chapter 2 demonstrates that ICESat-2 may be used for shallow water bathymetry. However, more work is needed to address automation challenges and to reduce uncertainty from melt pond beds. The issue of volumetric scattering at the beds of supraglacial lakes is particularly challenging, as the time delays that signal photons may experience at a pond bed are not yet quantified. A follow-on study may then use Monte Carlo modeling to simulate the interactions between signal photons, the melt pond, and the underlying ice. Other research may

develop more sophisticated filtering techniques for photons at the pond bed, particularly for ponds that exceed 7 m in depth. An improved filtering algorithm would also be useful for surface detection, given that the LSBS algorithm struggles with ponds that are too small. Other lake depth retrieval algorithms are highlighted by *Fricker et al.* (2021), several of which also hold promise for automation improvements, though we also speculate that machine learning may facilitate an improved photon filtering process. A follow-on study also needs to compare depth retrievals between ICESat-2 and ATM. Although such a comparison would be limited to the OIB 2018-2019 Greenland campaigns, it would be beneficial to directly compare the accuracy of the altimeters over co-registered lakes.

The snow grain size retrieval study was exclusively a modeling effort, so further research needs to assess retrievals using hyperspectral imaging or contact spectroscopy. Observing changes in retrieved grain size will be difficult in typical field campaigns, so laboratory experiments may be required to assess the perturbations considered in Chapter 3. For instance, *Donahue et al.* (2020) assessed albedo and grain size retrieval errors due to changes in illumination angle, where sunlight was simulated using an artificial light source. A specialized radiometer could then be used to measure differences in hemispheric and directional reflectance. Conversely, *Skiles et al.* (2017) observed a major dust deposition event within the San Juan snowpack, so field measurements of dust-induced retrieval errors may be possible through contact spectroscopy. Assessment of errors due to asymmetry parameter will be more difficult, but a follow-on study could predict snow grain shapes if the age of a snowpack is known. If a modeling study were to be performed, then the possible relationships and co-dependencies between snow perturbations should be considered, given that a combination of perturbations may significantly reduce or increase snow grain size retrieval errors.

5.2.1 ICESat-2 Calibration Over Snow-Covered Surfaces

In Chapter 4, we examine the impacts of uncertainty in snow grain size on airborne lidar altimetry. In a follow-up study, we expect to perform the same analysis for satellite altimetry from ICESat-2. We will perform the bias assessment over the region of Greenland analyzed in Chapter 4 (Figure 4.1). We will examine near-coincident ICESat-2 overpasses, with tracks from September 7 and 11 as suitable candidates for this analysis. ICESat-2 observations will need to be co-registered with ATM and AVIRIS-NG data from September 6. Although there is a time delay between the spaceborne and airborne data, we do not expect significant changes in surface composition to have occured over the study area.

We will generate pseudo-waveforms from the co-registered ICESat-2 data using surface height histograms derived from the ATL03 Global Geolocated Photon Product (*Neumann et al.*, 2019b). The pseudo-waveforms will be generated by aggregating ATL03 signal photons into 20 m segments and creating a histogram for each segment. We will then compare ATL03 pseudo-waveforms to ATM waveforms to identify common signatures from snow surface returns and to estimate bias. As in Chapter 4, we will derive expected bias estimates using the Monte Carlo model developed by *Schneider et al.* (2019) and AVIRIS-NG snow grain size data. We expect to develop a bias correction algorithm after this analysis that will consider snow cover extent, density, and grain size. Ideally, the correction algorithm will be applicable to ICESat-2 height measurements over all snow surfaces.

If a bias correction algorithm is developed, we anticipate that ICESat-2 data could be used for global snow depth measurements. Such a study would require validation from airborne and in-situ sources, so initial snow depth retrievals could be performed over regions where these studies were undertaken. For example, the NASA SnowEx mission is a series of campaigns designed to answer questions related to snow, and it includes useful snow depth measurements from locations across the western United

States. The study could then be expanded to perform global measurements of snow depth by using a mixture of satellite imagery and reanalysis data to retrieve snow properties and constrain the bias correction algorithm. The ICESat-2 data (and retrieved snow depths) could be further processed over forested regions by using the ATL08 Land and Vegetation Height Product (*Neuenschwander and Pitts*, 2019).

APPENDICES

APPENDIX A

Deriving Surface Heights Using Airborne Topographic Mapper Waveforms

Unlike ICESat-2, the raw data product from the Airborne Topographic Mapper (ATM) does not compose of geolocated spot measurements of the surface. Instead, the ATM instrument digitizes transmitted and received laser pulses into waveforms based on the time of detection and the strength of the signal. Each waveform has a series of digitized samples that are obtained every 0.25 ns, and each sample is assigned a signal strength, or amplitude. The amplitude recorded by the receiver is capped at a value of 255, so the true signal strength of a surface target may be lost. This issue is most common over specular surfaces, such as water or fresh snow.

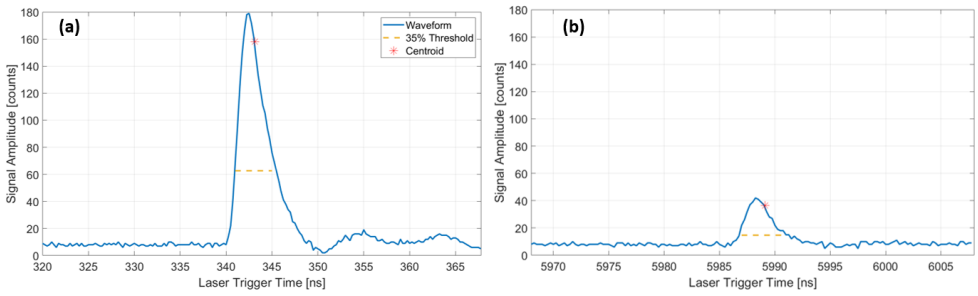

Figure A.1: An example ATM laser pulse digitized into a transmitted waveform (a) and a received waveform (b). The signal threshold and centroid are highlighted using dotted lines and stars, respectively.

To derive surface heights from ATM waveforms, the digitized data is first time-tagged and classified based on the time of transmittance. The data sometimes features signal returns that originate from the aircraft windows, and these window reflections are typically recorded before the transmitted and received waveforms. The transmittance time and shape of the transmitted waveform is generally constant between laser pulses, though imperfections in the design may result in slight differences in the timing and the waveform amplitude. Figure A.1 shows sample transmitted and received waveforms by the 532 nm detector. The waveforms were obtained over optically deep water, so the received signal has a much weaker signal than the initial pulse. From these waveforms, a threshold is determined to distinguish the signal from background noise. The ATM detector uses a threshold of 35% of the maximum amplitude, as shown by the dashed lines in the example waveforms. The range is then calculated using the centroid time of each waveform, with the waveforms assumed to be quasi-Gaussian waves. The pulse width is taken as the maximum width, or number of digitizer samples, of the waveform above the noise threshold. For instance, both waveforms in Figure A.1 have a pulse width of 19 digitized samples.

In Figure A.1, the centroid time for the transmitted and received pulses is 343.125 ns and 5989.1 ns, respectively. Using Equation 1.4, we calculate an uncalibrated aircraft-surface range of 846.9 m. This range is then calibrated relative to ground-based instrument bias assessments. The calibrated range serves as input to a reference geoid model along with the aircraft location and baseline pointing data to estimate surface elevation from the lidar signal. In the given example, the calculated range corresponds to a surface elevation of $\sim$476.7 m.

BIBLIOGRAPHY

BIBLIOGRAPHY

Abdalati, W., et al. (2010), The ICESat-2 laser altimetry mission, *Proceedings of the IEEE*, *98*, 735–751, doi:10.1109/JPROC.2009.2034765.

Aoki, T., T. Aoki, M. Fukabori, and A. Uchiyama (1999), Numerical simulation of the atmospheric effects on snow albedo with a multiple scattering radiative transfer model for the atmosphere-snow system, *Journal of the Meteorological Society of Japan*, *77*, 595–614, doi:https://doi.org/10.2151/jmsj1965.77.2_595.

Bales, R. C., N. P. Molotch, T. H. Painter, M. D. Dettinger, R. Rice, and J. Dozier (2006), Mountain hydrology of the western United States, *Water Resources Research*, *42*, W08,432, doi:10.1029/2005WR004387.

Balkanski, Y., M. Schulz, T. Claquin, and S. Guibert (2007), Reevaluation of Mineral aerosol radiative forcings suggests a better agreement with satellite and AERONET data, *Atmospheric Chemistry and Physics*, doi:10.5194/acp-7-81-2007.

Bamber, J. L., R. E. M. Riva, B. L. A. Vermeersen, and A. M. LeBrocq (2009), Reassessment of the potential sea-level rise from a collapse of the West Antarctic Ice Sheet, *Science*, *324*, 901–903, doi:10.1126/science.1169335.

Banwell, A. F., N. S. Arnold, I. C. Willis, M. Tedesco, and A. P. Ahlstrøm (2012), Modeling supraglacial water routing and lake filling on the Greenland Ice Sheet, *Journal of Geophysical Research: Earth Surface*, *117*, doi:10.1029/2012JF002393.

Banwell, A. F., D. R. MacAyeal, and O. V. Sergienko (2013), Breakup of the Larsen B Ice Shelf triggered by chain reaction drainage of supraglacial lakes, *Geophysical Research Letters*, *40*, 5872–5876, doi:10.1002/2013GL057694.

Barnett, T. P., J. C. Adam, and D. P. Lettenmaier (2005), Potential impacts of a warming climate on water availability in snow-dominated regions, *Nature*, *438*, 303–309, doi:https://doi-org.proxy.lib.umich.edu/10.1038/nature04141.

Beaglehole, D., B. Ramanathan, and J. Rumberg (1998), The UV to IR transmittance of Antarctic snow, *Journal of Geophysical Research Atmospheres*, doi:10.1029/97JD03604.

Bennartz, R., M. D. Shupe, D. D. Turner, V. P. Walden, K. Steffen, C. J. Cox, M. S. Kulie, N. B. Miller, and C. Petterson (2013), July 2012 Greenland melt extent enhanced by low-level liquid clouds, *Nature*, *496*, 83–86, doi:10.1038/nature12002.

Bevis, M., C. Harig, S. A. Khan, A. Brown, and F. J. Simons (2019), Accelerating changes in ice mass within Greenland, and the ice sheet's sensitivity to atmospheric forcing, *Proceedings of the National Academy of Sciences*, *116*, 1934–1939, doi: https://doi.org/10.1073/pnas.1806562116.

Box, J. E., and K. Ski (2007), Remote sounding of Greenland supraglacial melt lakes: implications for subglacial hydraulics, *Journal of Glaciology*, *53*, 257–265, doi:10.3189/172756507782202883.

Brock, J. C., C. W. Wright, A. H. Sallenger, W. B. Krabill, and R. N. Swift (2002), Basis and methods of NASA Airborne Topographic Mapper lidar surveys for coastal studies, *Journal of Coastal Research*, *18*, 1–13.

Brunt, K. M., T. A. Neumann, J. M. Amundson, J. L. Kavanaugh, M. S. Moussavi, K. M. Walsh, W. B. Cook, and T. Markus (2016), MABEL photon-counting laser altimetry data in Alaska for ICESat-2 simulations and development, *The Cryosphere*, *10*, 1707–1719, doi:10.5194/tc-10-1707-2016.

Brunt, K. M., T. A. Neumann, and C. F. Larsen (2019a), Assessment of altimetry using ground-based GPS data from the 88S Traverse, Antarctica, in support of ICESat-2, *The Cryosphere*, *13*, 579–590, doi:https://doi.org/10.5194/tc-13-579-2019.

Brunt, K. M., T. A. Neumann, and B. E. Smith (2019b), Assessment of ICESat-2 ice sheet surface heights, based on comparisons over the interior of the Antarctic Ice Sheet, *Geophysical Research Letters*, *46*, 13,072–13,078, doi: 10.1029/2019GL084886.

Catania, G. A., T. A. Neumann, and S. F. Price (2008), Characterizing englacial drainage in the ablation zone of the Greenland ice sheet, *Journal of Glaciology*, *54*, 567–578, doi:10.3189/002214308786570854.

Chen, X., X. Huang, and M. G. Flanner (2014), Sensitivity of modeled far-IR radiation budgets in polar continents to treatments of snow surface and ice cloud radiative properties, *Geophysical Research Letters*, *41*, 6530–6537, doi: 10.1002/2014GL061216.

Cook, J. M., et al. (2020), Glacier algae accelerate melt rates on the south-western Greenland Ice Sheet, *The Cryosphere*, *14*, 309–330, doi:10.5194/tc-14-309-2020.

Curry, J. A., W. B. Rossow, D. Randall, and J. L. Schramm (1996), Overview of Arctic Cloud and Radiation Characteristics, *Journal of Climate*, *9*, 1731–1764.

Dang, C., Q. Fu, and S. G. Warren (2016), Effect of snow grain shape on snow albedo, *Journal of the Atmospheric Sciences*, doi:10.1175/JAS-D-15-0276.1.

Das, S. B., I. Joughin, M. D. Behn, I. M. Howat, M. A. King, D. Lizarralde, and M. P. Bhatia (2008), Fracture propagation to the base of the Greenland Ice Sheet during supraglacial lake drainage, *Science*, *320*, 778–781, doi:10.1126/science.1153360.

Deems, J. S., T. H. Painter, and D. C. Finnegan (2013), Lidar measurement of snow depth: a review, *Journal of Glaciology*, *59*, 467–479, doi:10.3189/2013JoG12J154.

Dickinson, R. E. (1983), Land surface processes and climate—surface albedos and energy balance, *Advances in Geophysics*, *25*, 305–353, doi: https://doi.org/10.1016/S0065-2687(08)60176-4.

Donahue, C., S. M. Skiles, and K. Hammonds (2020), In situ effective snow grain size mapping using a compact hyperspectral imager, *Journal of Glaciology*, pp. 1–9, doi:10.1017/jog.2020.68.

Dong, P., and Q. Chen (2017), *LiDAR Remote Sensing and Applications*, CRC Press.

Dozier, J., and D. Marks (1987), Snow Mapping and Classification from Landsat Thematic Mapper Data, *Annals of Glaciology*, doi:10.3189/s026030550000046x.

Dozier, J., R. O. Green, A. W. Nolin, and T. H. Painter (2009), Interpretation of snow properties from imaging spectrometry, *Remote Sensing of Environment*, doi: 10.1016/j.rse.2007.07.029.

Dumont, M., O. Brissaud, G. Picard, B. Schmitt, J.-C. Gallet, and Y. Arnaud (2010), High-accuracy measurements of snow Bidirectional Reflectance Distribution Function at visible and NIR wavelengths – comparison with modelling results, *Atmospheric Chemistry and Physics Discussions*, doi:10.5194/acpd-9-19279-2009.

Echelmeyer, K., T. S. Clarke, and W. D. Harrison (1991), Surficial glaciology of Jakobshavns Isbrae, West Greenland: Part I. Surface morphology, *Journal of Glaciology*, *37*, 368–382.

Fair, Z., M. Flanner, K. M. Brunt, H. A. Fricker, and A. Gardner (2020), Using ICESat-2 and Operation IceBridge altimetry for supraglacial lake depth retrievals, *The Cryosphere*, *14*, 4253–4263, doi:10.5194/tc-14-4253-2020.

Fitzpatrick, A. A. W., et al. (2014), A decade (2002-2012) of supraglacial lake volume estimates across Russell Glacier, West Greenland, *The Cryosphere*, *8*, 107–121, doi: 10.5194/tc-8-107-2014.

Flanner, M., and C. Zender (2006), Linking snowpack microphysics and albedo evolution, *Journal of Geophysical Research*, *111*, doi: http://doi.org/10.1029/2005JD006834.

Flanner, M. G., C. S. Zender, J. T. Randerson, and P. J. Rasch (2007), Present-day climate forcing and response from black carbon in snow, *Journal of Geophysical Research Atmospheres*, doi:10.1029/2006JD008003.

Fretwell, L. O., H. D. Pritchard, D. G. Vaughan, J. L. Bamber, N. E. Barrand, R. Bell, et al. (2013), Bedmap2: improved ice bed, surface and thickness datasets for Antarctica., *The Cryosphere*, *7*, 375–393, doi:https://doi.org/10.5194/tc-7-375-2013.

Fricker, H. A., et al. (2021), ICESat-2 meltwater depth retrievals: application to surface melt on Amery Ice Shelf, East Antarctica, *Geophysical Research Letters*, *48*, doi:10.1029/2020GL090550.

Gao, B. C., K. B. Heidebrecht, and A. F. Goetz (1993), Derivation of scaled surface reflectances from AVIRIS data, *Remote Sensing of Environment*, doi:10.1016/0034-4257(93)90014-O.

Gatziolis, D., and H. E. Andersen (2008), A guide to lidar data acquisition and processing for the forests of the Pacific Northwest, *Tech. rep.*, United States Forest Service.

Georgiou, S., A. Shepherd, M. McMillan, and P. Nienow (2009), Seasonal evolution of supraglacial lake volume from ASTER imagery, *Annals of Glaciology*, *50*, 95–100, doi:10.3189/172756409789624328.

Green, R., et al. (1998), Imaging spectroscopy and the Airborne Visible/Infrared Imaging Spectrometer (AVIRIS), *Remote Sensing of Environment*, *65*, 227–248, doi:10.1016/S0034-4257(98)00064-9.

Grenfell, T. C., and S. G. Warren (1999), Representation of a nonspherical ice particle by a collection of independent spheres for scattering and absorption of radiation, *Journal of Geophysical Research Atmospheres*, doi:10.1029/1999JD900496.

Grenfell, T. C., S. G. Warren, and P. C. Mullen (1994), Reflection of solar radiation by the Antarctic snow surface at ultraviolet, visible, and near-infrared wavelengths, *Journal of Geophysical Research*, *99*, 18,669–18,684, doi: https://doi.org/10.1029/94JD01484.

Grenfell, T. C., S. P. Neshyba, and S. G. Warren (2005), Representation of a nonspherical ice particle by a collection of independent spheres for scattering and absorption of radiation: 3. Hollow columns and plates, doi:10.1029/2005JD005811.

Harding, D., P. Dabney, S. Valett, A. Yu, A. Vasilyev, and A. Kelly (2011), Airborne polarimetric, two-color laser altimeter measurements of lake ice cover: A pathfinder for NASA's ICESat-2 spaceflight mission, in *International Geoscience and Remote Sensing Symposium*, doi:10.1109/IGARSS.2011.6050002.

Hartmann, D. L. (2016), *Global Physical Climatology*, Elsevier.

Howat, I. M., S. de la Peña, J. H. van Angelen, J. T. M. Lenaerts, and M. R. van den Broeke (2013), Brief Communication: Expansion of meltwater lakes on the Greenland Ice Sheet, *The Cryosphere*, *7*, 201–204, doi:10.5194/tc-7-201-2013.

Huang, X., X. Chen, M. Flanner, P. Yang, D. Feldman, and C. Kuo (2018), Improved representation of surface spectral emissivity in a global climate model and its impact on simulated climate, *Journal of Climate*, *31*, 3711–3727, doi:10.1175/JCLI-D-17-0125.1.

Humphrey, N. F., J. T. Harper, and W. T. Pfeffer (2012), Thermal tracking of meltwater retention in Greenland's accumulation area, *Journal of Geophysical Research: Earth Surface*, *117*, doi:10.1029/2011JF002083.

Jasinski, M. F., J. D. Stoll, W. B. Cook, M. Ondrusek, E. Stengel, and K. Brunt (2016), Inland and near-shore water profiles derived from the high-altitude Multiple Altimeter Beam Experimental Lidar (MABEL), *J. Coast. Res.*, *76*, 44–55.

Kerekes, J., A. Goodenough, S. Brown, J. Zhang, B. Csatho, A. Schenk, S. Nagarajan, and R. Wheelwright (2012), First principles modeling for lidar sensing of complex ice surfaces, in *2012 IEEE International Geoscience and Remote Sensing Symposium*, pp. 3241–3244, IEEE, doi:10.1109/IGARSS.2012.6350733.

Kingslake, J., J. C. Ely, I. Das, and R. E. Bell (2017), Widespread movement of meltwater onto and across Antarctic ice shelves, *Nature*, *544*, 349–352, doi:10.1038/nature22049.

Kokaly, R. F., D. G. Despain, R. N. Clark, and K. E. Livo (2003), Mapping vegetation in Yellowstone National Park using spectral feature analysis of AVIRIS data, *Remote Sensing of Environment*, *83*, 437–456, doi:10.1016/S0034-4257(02)00133-5.

Kokhanovsky, A. A., and E. P. Zege (2004), Scattering optics of snow, *Applied Optics*, doi:10.1364/AO.43.001589.

Krabill, W. B., W. Abdalati, E. B. Frederick, S. S. Manizade, C. F. Martin, J. G. Sonntag, R. N. Swift, R. H. Thomas, and J. G. Yungel (2002), Aircraft laser altimetry measurement of elevation changes of the Greenland Ice Sheet: technique and accuracy assessment, *Journal of Geodynamics*, *34*, 357–376, doi:10.1016/S0264-3707(02)00040-6.

Kwok, R., S. Kacimi, T. Markus, N. T. Kurtz, M. Studinger, J. G. Sonntag, S. S. Manizade, L. N. Boisvert, and J. P. Harbeck (2019), ICESat-2 surface height and sea ice freeboard assessed with ATM lidar acquisitions from Operation IceBridge, *Geophysical Research Letters*, *46*, 11,228–11,236, doi:10.1029/2019GL084976.

Kwok, R., S. Kacimi, M. A. Webster, N. T. Kurtz, and A. A. Petty (2020), Arctic snow depth and sea ice thickness from ICESat-2 and CryoSat-2 freeboards: A first examination, *Journal of Geophysical Research: Oceans*, doi:10.1029/2019JC016008.

Lachlan-Cope, T. (2010), Antarctic clouds, *Polar Research*, *29*, 150–158, doi:10.3402/polar.v29i2.6065.

Leeson, A. A., A. Shepherd, K. Briggs, I. Howat, X. Fettweis, M. Morlighem, and E. Rignot (2015), Supraglacial lakes on the Greenland ice sheet advance inland under warming climate, *Nature Climate Change*, *5*, 51–55, doi:10.1038/nclimate2463.

Li, W. (2007), Bidirectional reflectance distribution function of snow: corrections for the Lambertian assumption in remote sensing applications, *Optical Engineering*, doi:10.1117/1.2746334.

Liang, S. (2000), Narrowband to broadband conversions of land surface albedo I: Algorithms, *Remote Sensing of Environment*, *76*, 213–238, doi: https://doi.org/10.1016/S0034-4257(00)00205-4.

Liang, S. (2018), *Comprehensive Remote Sensing*, Elsevier.

Liang, Y.-L., W. Colgan, Q. Lv, K. Steffen, W. Abdalati, J. Stroeve, D. Gallaher, and N. Bayou (2012), A decadal investigation of supraglacial lakes in West Greenland using a fully automatic detection and tracking algorithm, *Remote Sensing of Environment*, *123*, 127–138, doi:10.1016/j.rse.2012.03.020.

Libois, Q., G. Picard, J. L. France, L. Arnaud, M. Dumont, C. M. Carmagnola, and M. D. King (2013), Influence of grain shape on light penetration in snow, *Cryosphere*, doi:10.5194/tc-7-1803-2013.

Liou, K. N. (2002), *An Introduction to Atmospheric Radiation*, International Geophysics Series, Academic Press.

Liu, Z., M. Vaughan, D. Winker, A. Hostetler, L. R. Poole, L. Hlavka, D., W. D. Hart, and M. J. McGill (2004), Use of probability distribution functions for discriminating between cloud and aerosol in lidar backscatter data, *Journal of Geophysical Research*, *109*, doi:https://doi.org/10.1029/2004JD004732.

Lüthje, M., L. T. Pedersen, N. Reeh, and W. Greuell (2006), Modelling the evolution of supraglacial lakes on the West Greenland ice-sheet margin, *Journal of Glaciology*, *52*, 608–618, doi:10.3189/172756506781828386.

Ma, Y., N. Xu, J. Sun, X. H. Wang, F. Yang, and S. Li (2019), Estimating water levels and volumes of lakes dated back to the 1980s using Landsat imagery and photon-counting lidar datasets, *Remote Sensing of Environment*, *232*, 111,287, doi: 10.1016/j.rse.2019.111287.

Magruder, M., et al. (2019), New Earth orbiter provides a sharper look at a changing planet, *Eos*, *100*, doi:10.1029/2019EO133233.

Manizade, S. (2020), personal communication.

Markus, T., et al. (2017), The Ice, Cloud, and land Elevation Satellite-2 (ICESat-2): Science requirements, concept, and implementation, *Remote Sensing of Environment*, *190*, 260–273, doi:10.1016/j.rse.2016.12.029.

Martin, C. F., W. B. Krabill, S. S. Manizade, R. L. Russel, J. G. Sonntag, R. N. Swift, and J. K. Yungel (2012), Airborne Topographic Mapper calibration procedures and accuracy assessment, *Tech. Rep. 215891*, NASA Goddard Space Flight Center.

McMillan, M., P. Nienow, A. Shepherd, T. Benham, and A. Sole (2007), Seasonal evolution of supra-glacial lakes on the Greenland Ice Sheet, *Earth and Planetary Science Letters*, *262*, 484–492, doi:10.1016/j.epsl.2007.08.002.

Mellor, M., and G. McKinnon (1960), The Amery Ice Shelf and its hinterland, *Polar Record*, *10*, 30–34, doi:10.1017/S0032247400050579.

Morassutti, M. P., and E. F. Ledrew (1996), Albedo and depth of melt ponds on sea-ice, *International Journal of Climatology*, *16*, 817–838, doi: http://doi.wiley.com/10.1002/(SICI)1097-0088(199607).

Morlighem, M., et al. (2017), BedMachine v3: Complete bed topography and ocean bathymetry mapping of Greenland from multibeam echo sounding combined with mass conservation, *Geophysical Research Letters*, *44*, doi:10.1002/2017GL074954.

Mouginot, J., E. Rignot, A. A. Bjørk, M. van den Broeke, R. Millan, M. Morlighem, B. Noël, B. Scheuchl, and M. Wood (2019), Forty-six years of Greenland Ice Sheet mass balance from 1972 to 2018, *Proceedings of the National Academy of Sciences*, *116*, 9239–9244, doi:https://doi.org/10.1073/pnas.1904242116.

Moussavi, M., A. Pope, A. R. W. Halberstadt, T. L. D., L. Cioffi, and W. Abdalati (2020), Antarctic supraglacial lake detection using Landsat 8 and Sentinel-2 imagery: Towards continental generation of lake volumes, *Remote Sensing*, *12*, doi:2072-4292/12/1/134.

Moussavi, M. S., W. Abdalati, A. Pope, T. Scambos, M. Tedesco, M. MacFerrin, and S. Grigsby (2016), Derivation and validation of supraglacial lake volumes on the Greenland Ice Sheet from high-resolution satellite imagery, *Remote Sensing of Environment*, *183*, 294–303, doi:10.1016/j.rse.2016.05.024.

National Academies of Sciences, Engineering, and Medicine (2018), *Thriving on Our Changing Planet: A Decadal Strategy for Earth Observation from Space*, chap. 6, The National Academies Press, doi:https://doi.org/10.17226/24938.

Neshyba, S. P., T. C. Grenfell, and S. G. Warren (2003), Representation of a nonspherical ice particle by a collection of independent spheres for scattering and absorption of radiation: 2. Hexagonal columns and plates, *Journal of Geophysical Research: Atmospheres*, doi:10.1029/2002jd003302.

Neuenschwander, A., and K. Pitts (2019), The ATL08 land and vegetation product for the ICESat-2 mission, *Remote Sensing of Environment*, *221*, 247–259, doi: 10.1016/j.rse.2018.11.005.

Neuenschwander, A. L., L. A. Magruder, and M. Tyler (2009), Landcover classification of small-footprint, full-waveform lidar data, *Journal of Applied Remote Sensing*, *3*, doi:https://doi.org/10.1117/1.3229944.

Neumann, T., et al. (2020), Ice, Clouds, and Land Elevation Satellite-2 (ICESat-2): Algorithm Theoretical Basis Document (ATBD) for Geolocated Photons, *Tech. rep.*, NASA Goddard Space Flight Center.

Neumann, T. A., et al. (2019a), ATLAS/ICESat-2 L2A Global Geolocated Photon Data, Version 2, https://doi.org/10.5067/ATLAS/ATL03.001.

Neumann, T. A., et al. (2019b), The Ice, Clouds and Land Elevation Satellite-2 mission: A global geolocated photon product derived from the Advanced Topographic Laser Altimeter System, *Remote Sensing of Environment*, *233*, doi: doi.org/10.1016/j.rse.2019.111325.

Nicodemus, F., J. Richmond, I. W. Hsia, J. Ginsberg, and T. Limperis (1977), Geometrical considerations and nomenclature for reflectance, *National Bureau of Standards*.

Nolin, A. W., and J. Dozier (1993), Estimating snow grain size using AVIRIS data, *Remote Sensing of Environment*, doi:10.1016/0034-4257(93)90018-S.

Nolin, A. W., and J. Dozier (2000), A hyperspectral method for remotely sensing the grain size of snow, *Remote Sensing of Environment*, doi:10.1016/S0034-4257(00)00111-5.

Painter, T. H., N. P. Molotch, M. Cassidy, M. Flanner, and K. Steffen (2007), Instruments and methods: Contact spectroscopy for determination of stratigraphy of snow optical grain size, *Journal of Glaciology*, doi:10.3189/172756507781833947.

Painter, T. H., F. C. Seidel, A. C. Bryant, S. McKenzie Skiles, and K. Rittger (2013), Imaging spectroscopy of albedo and radiative forcing by light-absorbing impurities in mountain snow, *Journal of Geophysical Research Atmospheres*, doi: 10.1002/jgrd.50520.

Parizek, B. R., and R. B. Alley (2004), Implications of increased Greenland surface melt under global-warming scenarios: ice-sheet simulations, *Quaternary Science Reviews*, *23*, 1013–1027.

Parrish, C. E., L. A. Magruder, A. L. Neuenschwander, N. Forfinski-Sarkozi, M. Alonzo, and M. Jasinki (2019), Validation of ICESat-2 ATLAS bathymetry and analysis of ATLAS's bathymetric mapping performance, *Remote Sensing*, *11*, 1634, doi:10.3390/rs11141634.

Penczykowski, R. M., B. M. Connolly, and B. T. Barton (2017), Winter is changing: Trophic interactions under altered snow regimes, *Food Webs*, *13*, 80–91.

Perovich, D. K. (2007), Light reflection and transmission by a temperate snow cover, *Journal of Glaciology*, doi:10.3189/172756507782202919.

Petty, G. W. (2006), *A First Course in Atmospheric Radiation*, Sundog Publishing.

Phillips, H. A. (1998), Surface meltstreams on the Amery Ice Shelf, East Antarctica, *Annals of Glaciology*, *27*, 177–181.

Philpot, W. D. (1989), Bathymetric mapping with passive multispectral imagery, *Applied Optics*, *28*, 1569–1578, doi:10.1364/AO.28.001569.

Picard, G., F. Domine, G. Krinner, L. Arnaud, and E. Lefebvre (2012), Inhibition of the positive snow-albedo feedback by precipitation in interior Antarctica, *Nature Climate Change*, doi:10.1038/nclimate1590.

Picard, G., M. Dumont, M. Lamare, F. Tuzet, F. Larue, R. Pirazzini, and L. Arnaud (2020), Spectral albedo measurements over snow-covered slopes: Theory and slope effect corrections, *Cryosphere*, doi:10.5194/tc-14-1497-2020.

Polashenski, C. M., J. E. Dibb, M. G. Flanner, J. Y. Chen, Z. R. Courville, A. M. Lai, J. J. Schauer, M. M. Shafer, and M. Bergin (2015), Neither dust nor black carbon causing apparent albedo decline in Greenland's dry snow zone: Implications for MODIS C5 surface reflectance, *Geophysical Research Letters*, doi: 10.1002/2015GL065912.

Pope, A. (2016), Reproducibly estimating and evaluating supraglacial lake depth with Landsat 8 and other multispectral sensors, *Earth and Space Science*, *3*, 176–188, doi:10.1002/2015EA000125.

Pope, A., T. A. Scambos, M. Moussavi, M. Tedesco, M. Willis, D. Shean, and S. Grigsby (2016), Estimating supraglacial lake depth in West Greenland using Landsat 8 and comparison with other multispectral methods, *The Cryosphere*, *10*, 15–27, doi:10.5194/tc-10-15-2016.

Popescu, S. C., T. Zhou, R. Nelson, A. Neuenschwander, R. Sheridan, L. Narine, and K. M. Walsh (2018), Photon counting LiDAR: An adaptive ground and canopy height retrieval algorithm for ICESat-2 data, *Remote Sensing of Environment*, *208*, 154–170, doi:https://doi.org/10.1016/j.rse.2018.02.019.

Pritchard, H. D., and G. D. Vaughan (2007), Widespread acceleration of tidewater glaciers on the Antarctic Peninsula, *Journal of Geophysical Research*, *112*, doi: 10.1029/2006JF000597.

Rignot, E., J. Mouginot, B. Scheuchl, M. van den Broeke, M. J. van Wessem, and M. Morlighem (2019), Four decades of Antarctic Ice Sheet mass balance from 1979–2017, *Proceedings of the National Academy of Sciences*, *116*, 1095–1103, doi: 10.1073/pnas.1812883116.

Rutan, D., F. Rose, M. Roman, N. Manalo-Smith, C. Schaaf, and T. Charlock (2009), Development and assessment of broadband surface albedo from clouds and the earth's radiant energy system clouds and radiation swath data product, *Journal of Geophysical Research*, *114*, doi:https://doi.org/10.1029/2008JD010669.

Schaepman-Strub, G., M. E. Schaepman, T. H. Painter, S. Dangel, and J. V. Martonchik (2006), Reflectance quantities in optical remote sensing — definitions and case studies, *Remote Sensing of Environment*, *103*, 27–42, doi: https://doi.org/10.1016/j.rse.2006.03.002.

Schneider, A., M. Flanner, R. De Roo, and A. Adolph (2019), Monitoring of snow surface near-infrared bidirectional reflectance factors with added light-absorbing particles, *Cryosphere*, doi:10.5194/tc-13-1753-2019.

Seidel, F. C., K. Rittger, S. McKenzie Skiles, N. P. Molotch, and T. H. Painter (2016), Case study of spatial and temporal variability of snow cover, grain size, albedo and radiative forcing in the Sierra Nevada and Rocky Mountain snowpack derived from imaging spectroscopy, *Cryosphere*, doi:10.5194/tc-10-1229-2016.

Selmes, N., T. Murray, and T. D. James (2011), Fast draining lakes on the Greenland Ice Sheet, *Geophysical Research Letters*, *38*, doi:10.1029/2011GL047872.

Shepherd, A., E. Rignot, and Others (2019), Mass balance on the Greenland Ice Sheet from 1992 to 2018, *Nature*, doi:https://doi.org/10.1038/s41586-019-1855-2.

Shuman, C. A., K. Steffen, J. E. Box, and C. R. Stearns (2001), A dozen years of temperature observations at the Summit: Central Greenland automatic weather stations 1987–99, *Journal of Applied Meteorology and Climatology*, *40*, 741–752, doi:https://doi.org/10.1175/1520-0450(2001)040¡0741:ADYOTO¿2.0.CO;2.

Skiles, S. M. K., and T. Painter (2017), Daily evolution in dust and black carbon content, snow grain size, and snow albedo during snowmelt, Rocky Mountains, Colorado, *Journal of Glaciology*, doi:10.1017/jog.2016.125.

Skiles, S. M. K., and T. H. Painter (2019), Toward Understanding Direct Absorption and Grain Size Feedbacks by Dust Radiative Forcing in Snow With Coupled Snow Physical and Radiative Transfer Modeling, *Water Resources Research*, doi:10.1029/2018WR024573.

Skiles, S. M. K., T. Painter, and G. S. Okin (2017), A method to retrieve the spectral complex refractive index and single scattering optical properties of dust deposited in mountain snow, *Journal of Glaciology*, doi:10.1017/jog.2016.126.

Smith, B., et al. (2019), Land ice height-retrieval algorithm for NASA's ICESat-2 photon-counting laser altimeter, *Remote Sensing of Environment*, *233*, doi:10.1016/j.rse.2019.111352.

Smith, B. E., A. Gardner, A. Schneider, and M. Flanner (2018), Modeling biases in laser-altimetry measurements caused by scattering of green light in snow, *Remote Sensing of Environment*, *215*, 398–410, doi:10.1016/j.rse.2018.06.012.

Sneed, W. A., and G. S. Hamilton (2007), Evolution of melt pond volume on the surface of the Greenland Ice Sheet, *Geophysical Research Letters*, *34*, doi:10.1029/2006GL028697.

Spinhirne, J. D. (1993), Micro pulse lidar, *IEEE Transactions on Geoscience and Remote Sensing*, *31*, 48–55, doi:https://doi.org/10.1109/36.210443.

Stamnes, K., S.-C. Tsay, W. Wiscombe, and K. Jayaweera (1988), Numerically stable algorithm for discrete-ordinate-method radiative transfer in multiple scattering and emitting layered media, *Applied Optics*, doi:10.1364/ao.27.002502.

Studinger, M. (2018), IceBridge ATM L1B Elevation and Return Strength, Version 2, https://doi.org/10.5067/19SIM5TXKPGT.

Stull, R. B. (1988), *An Introduction to Boundary Layer Meteorology*, Kluwer Academic Publishers.

Stumpf, R. P., K. Holderied, and M. Sinclair (2003), Determination of water depth with high-resolution satellite imagery over variable bottom types, *Limnology and Oceanography*, *48*, 547–556, doi:10.4319/lo.2003.48.1_part_2.0547.

Sturm, M., and C. S. Benson (1997), Vapor transport, grain growth and depth-hoar development in the subarctic snow, *Journal of Glaciology*, doi:10.3189/s0022143000002793.

Tedesco, M., and N. Steiner (2011), In-situ multispectral and bathymetric measurements over a supraglacial lake in western Greenland using a remotely controlled watercraft, *The Cryosphere*, *5*, 445–452, doi:10.5194/tc-5-445-2011.

The IMBIE Team (2018), Mass balance of the Antarctic Ice Sheet from 1992 to 2017, *Nature*, *558*, 219–222, doi:https://doi.org/10.1038/s41586-018-0179-y.

The IMBIE Team (2020), Mass balance of the Greenland Ice Sheet from 1992 to 2018, *Nature*, *579*, 233–239, doi:https://doi.org/10.1038/s41586-019-1855-2.

Thompson, D. R., L. Guanter, A. Berk, B. Gao, R. Richter, D. Schäpfer, and K. J. Thome (2019), Retrieval of atmospheric parameters and surface reflectance from visible and shortwave infrared imaging spectroscopy data, *Surveys in Geophysics*, *40*, 333–360, doi:https://doi.org/10.1007/s10712-018-9488-9.

Thorpe, A. K., et al. (2016), Mapping methane concentrations from a controlled release experiment using the next generation airborne visible/infrared imaging spectrometer (AVIRIS-NG), *Remote Sensing of Environment*, *179*, 104–115, doi:10.1016/j.rse.2016.03.032.

Toon, O. B., C. P. McKay, T. P. Ackerman, and K. Santhanam (1989), Rapid calculation of radiative heating rates and photodissociation rates in inhomogeneous multiple scattering atmospheres, *Journal of Geophysical Research*, doi:10.1029/jd094id13p16287.

Tuzet, F., et al. (2017), A multilayer physically based snowpack model simulating direct and indirect radiative impacts of light-absorbing impurities in snow, *Cryosphere*, doi:10.5194/tc-11-2633-2017.

Ulaby, F. T., R. K. Moore, and A. K. Fung (1986), *Microwave Remote Sensing: Active and Passive*, vol. 3, Artech House, Inc.

van de Hulst, H. C. (1968), Asymptotic fitting, a method for solving anisotropic transfer problems in thick layers, *Journal of Computational Physics*, doi:10.1016/0021-9991(68)90023-5.

van den Broeke, M. R., E. M. Enderlin, I. M. Howat, P. K. Munneke, B. P. Y. Noel, W. J. van de Berg, E. van Meijguard, and B. Wouters (2016), On the recent contribution of the Greenland Ice Sheet to sea level change, *The Cryosphere*, *10*, 1933–1946, doi:10.5194/tc-10-1933-2016.

Van Tricht, K., S. Lhermitte, J. T. M. Lenaerts, I. V. Gorodetskaya, T. S. L'Ecuyer, B. Noël, M. R. van den Broeke, D. D. Turner, and N. P. M. van Lipzig (2016), Clouds enhance Greenland Ice Sheet meltwater runoff, *Nature Communications*, *7*, doi:10.1038/ncomms10266.

Vaughan, D., et al. (2013), Chapter 4: Observations: Cryosphere, *Tech. rep.*, IPCC AR5 WG1.

Ward, J. L., M. G. Flanner, M. Bergin, J. E. Dibb, C. M. Polashenski, A. J. Soja, and J. L. Thomas (2018), Modeled Response of Greenland Snowmelt to the Presence of Biomass Burning-Based Absorbing Aerosols in the Atmosphere and Snow, *Journal of Geophysical Research: Atmospheres*, doi:10.1029/2017JD027878.

Warren, S. G. (1982), Optical properties of snow, *Review of Geophysics and Space Physics*, *20*, 67–89, doi:https://doi.org/10.1029/RG020i001p00067.

Warren, S. G., and R. E. Brandt (2008), Optical constants of ice from the ultraviolet to the microwave: A revised compilation, *Journal of Geophysical Research Atmospheres*, doi:10.1029/2007JD009744.

Warren, S. G., and W. J. Wiscombe (1980), A model for the spectral albedo of snow. II: snow containing atmospheric aerosols., *Journal of the Atmospheric Sciences*, doi:10.1175/1520-0469(1980)037<2734:AMFTSA>2.0.CO;2.

Wehr, A., and U. Lohr (1999), Airborne laser scanning — an introduction and overview, *ISPRS Journal of Photogrammetry and Remote Sensing*, *54*, 68–82, doi:https://doi.org/10.1016/S0924-2716(99)00011-8.

Williamson, A. G., N. S. Arnold, A. F. Banwell, and I. C. Willis (2017), A Fully Automated Supraglacial lake area and volume Tracking ("FAST") algorithm: Development and application using MODIS imagery of West Greenland, *Remote Sensing of Environment*, *196*, 113–133, doi:10.1016/j.rse.2017.04.032.

Wiscombe, W. J., and S. G. Warren (1980), A model for the spectral albedo of snow. I: pure snow., *Journal of the Atmospheric Sciences*, doi:10.1175/1520-0469(1980)037¡2712:AMFTSA¿2.0.CO;2.

Zhang, T. (2005), Influence of the seasonal snow cover on the ground thermal regime: An overview, *Review of Geophysics*, *43*, RG4002, doi:10.1029/2004RG000157.

Zhou, X., N.-B. Chang, and S. Li (2009), Applications of SAR interferometry in Earth and environmental science research, *Sensors*, *9*, 1876–1912, doi: https://doi.org/10.3390/s90301876.

Zwally, H. J., W. Abdalati, T. Herring, K. Larson, J. Saba, and K. Steffen (2002), Surface melt-induced acceleration of Greenland Ice-Sheet flow, *Science*, *297*, 218–222, doi:10.1126/science.1072708.